2021

# The Role of Compartmentalized Metabolism in Cellular Metal Homeostasis

Ross A. Weber


# THE ROLE OF COMPARTMENTALIZED METABOLISM IN CELLULAR METAL HOMEOSTASIS

A Thesis Presented to the Faculty of
The Rockefeller University
in Partial Fulfillment of the Requirements for
the degree of Doctor of Philosophy

by
Ross A. Weber
June 2021

# THE ROLE OF COMPARTMENTALIZED METABOLISM IN CELLULAR METAL HOMEOSTASIS

Ross A. Weber, Ph.D.
The Rockefeller University 2021

The building blocks of cells are usually thought to be DNA, RNA, and proteins. However, life, as we know it, is not possible without iron. While the list of iron's vital cellular functions is extensive, iron is also quite cytotoxic. Thus, great pains have been taken, at the gene regulation level, to assure that a cell has sufficient iron to copy its genome and power its mitochondria but not too much to damage its membranes with lipid peroxides. Cellular organelles, which accompanied the rise of atmospheric oxygen and an increased need for iron, also play a key role in iron homeostasis. Mitochondria are the sites of iron assimilation whereas lysosomes, with their v-ATPase-generated acidic lumens, are responsible for iron uptake and rely.

In the first part of this work, I focused on lysosomes. Unbiased genetic screens performed on cells grown at sub-lethal levels of lysosomal pH inhibition identified several important metabolic pathways in this context. These included central carbon metabolism, cholesterol synthesis and iron homeostasis. While, cells starve for cholesterol and iron, only iron supplementation was necessary and sufficient to restore cell proliferation upon genetic or pharmacologic v-ATPase inhibition. Interestingly, iron supplementation rescued cell viability independent of lysosomal associated functions including signaling and endocytosis. It did, however, reverse changes resulting from low cellular iron including destabilized iron sulfur cluster proteins, induced hypoxia signaling, and impaired respiration. Finally, due to compromised aconitase activity, I identified an increased dependence on pyruvate-derived citrated as a metabolic ramification of lysosomal dysfunction. Taken together, this strongly argued that providing cellular iron is the essential function of lysosomal acidity for cell proliferation

In the second part of this work, I explored other organelles in the setting of altered cellular iron. Using unbiased genetic screens, I found that iron chelation necessitates a fully intact mitochondrial iron import system. In this context, Golgi manganese uptake and storage were also essential. Because chemical or genetic induced manganese overload phenocopied iron starvation, cells were more sensitives to iron starvation and resistant to iron overload and ferroptosis. As mitochondria are the main sites of iron assimilation, I also characterized mitochondrial proteomic changes upon altered cellular iron. Here, I identified a mitochondrial solute transporter, SLC25A39, whose protein stability was proportional to cellular iron levels. Further investigation found a key role for this protein in maintaining mitochondrial GSH levels. Finally, I found that damaged or liberated iron sulfur clusters, rather than free iron, determine SLC25A39 stability. This finding may also represent an organelle-autonomous regulatory loop in which mitochondria coordinate GSH and iron homeostasis.

*To Grandma Hilda.*
*My first scientific mentor and a model of interpersonal generosity and intellectual rigor.*

## ACKNOWLEDGMENTS

First and foremost, I need to thank my mentor Kivanç Birsoy. As I found myself at a crossroads, after my first mentor left New York, you took a chance and invited me to your lab. Even though I spilled a large cup of coffee all over your new office in one of our first meetings, you stilled allowed me to join. I am truly grateful for the all the opportunities you have given to me, our stimulating (and sometimes freewheeling!) scientific discussions, and your sage advice about life outside the lab. You knew when to push me and when to give me breathing space. Like the human metabolome, I hope our paths continue to cross far into the future.

Of course, this would not be possible without the rest of the Birsoy lab. Lou Baudrier and Eiko Nishiuchi manage an extremely organized and well-run lab that could not be a more conducive place for free scientific inquiry. Frederick Yen, who first worked with me as a SURF undergraduate, joined the lab as an undergraduate researcher, and continued on as a research assistant. This work could not have been completed without your help. You are one of the most technically talented and cerebral scientists I have even encountered and your generosity and kindness are inspiring. I have certainly learned more from you than I could ever convey back. You have a bright future ahead for yourself as a fellow MD-PhD trainee!

Rebecca Timson, who began as a rotation student with me, assisted me with difficult imaging experiments and taught me a lot about cellular signaling. Konnor La—on a personal level, campus walks and meals shared later into the night have always been a source of great enjoyment and relief during graduate school. On a scientific level, I thank you for all your bioinformatic and computational expertise as well as an open ear and a critical mind on which to try out new and sometimes crazy ideas. I thank Dr. Erol Bayraktar, a post-doctoral fellow in the lab for his assistance and know-how regarding cholesterol metabolism. I thank Dr. Javier Garcia-Bermudez and Mariluz Soula, for our collaboration on the ferroptosis project. I look forward to hearing all about the new antioxidants and cancer metabolites you will find. I thank Dr. Ying Wang, a clinical fellow in the lab with whom much of the work in Chapter 3 was performed in close collaboration. I look forward to our continued collaboration.

Of course, everyone else in the lab has been generous with their time and patience. Thank you to Dr. Clifton Fulmer, Dr. Tim Kenny, Dr. Maria Liberti, Dr. Max Stahl, Dr. Gokhan Unlu, Xiphias Ge Zhu, Rohiverth Goarorecuco, Robert Williams, Ben Prizer, and all the rotation, visiting, summer students and fellows for making the lab the inviting, fun, and productive place that it is. I cannot remember a time when a call for second set of hands or a slack about a reagent went unanswered. Our annual Knicks and Nets games, BBQ afterparties, and holiday dinners and karaoke were highlights of my four years in lab.

Much of this work involved the Herculean efforts of the proteomics core with whom we managed to get a metabolomics service up and running. I thank Henrik Molina, director of the core, for his scientific guidance and especially, for his patience during the growing pains of the first year of this effort. The rest of the staff: Justine Fidelin, Sahil Sharma, Hanan Alwaseem, Bety Rostandy, and Soeren Heissel have

been extraordinarily dedicated and helpful with metabolomics and proteomics experiments. I also acknowledge the high throughput screening and FACS core facilities for their help as well.

I thank our other collaborators. Dr. Monther Abu-Remaileh for all his technical assistance with lysosomal isolations. I thank Shirony Nicholson, who was a visiting student in our lab, for all her help on the early stages of this project.

I acknowledge and thank the chair of my thesis committee, Dr. Sohail Tavazoie, whose guidance has been invaluable and has made this process as smooth as possible. I wish to thank my other committee members, Dr. John Blenis and Dr. Michael Rout, who have consistently provided thoughtful advice and interesting experimental ideas during our committee meetings and informal discussions. I also thank my external examiner, Dr. Ralph Deberardinis, Children's Medical Research Institute, UT Southwestern Medical Center, for participating in my thesis defense. Unfortunately, current times dictate a virtual defense but I look forward to meeting in person at a conference or seminar in the near future.

Finally, I thank the administration and staff of the David Rockefeller Graduate Program and the Tri-Institutional MD-PhD program for accommodating my needs, providing strong support and making my experience here one that I will cherish.

On a personal level, I thank all my teachers, friends, colleagues and everyone in between. I am fortunate that they are numerous to name here. Nonetheless, there are a few people whom I am obliged to mention. First and foremost, I thank my parents. What is mine is certainly theirs. Their unconditional love and patience and their encouragement to pursue a life of questioning and contemplation over career has brought me to this point. I also thank my siblings, Garret and Mia, for all their support and care during these years. Weekends with away from the city with both of you provided much needed respite from the lab. Last and certainly not least I thank Rachel. I am so lucky to have you and your love in my life during these heady times. You were understanding when experiments went unexpectedly late and an unwavering source of support throughout.

Finally, this thesis is dedicated to my late Grandma Hilda, of blessed memory. As a professor of physics, she was certainly ahead of her time. Our Thursday night sessions of physics and pizza, throughout high school exposed me to the scientific method. She encouraged me to look for meaning rather than math and ideas over numbers. She was a model of how to move between worlds, embracing the complexity of life rather than settling for contradictions.

## Table of Contents

## List of Figures

## CHAPTER 1: Introduction

### Iron is essential for life

Life cannot subsist solely on carbon, hydrogen, oxygen, and nitrogen. Transition metals including Fe, Mn, Co, Cu, Zn, and Mo support protein structural integrity, facilitate specific substrate binding, catalyze enzymatic reactions, and serve as electron transfer relays to sustain energy homeostasis. This biochemical utility emerges from incompletely filled d-orbitals that enable multiple stable oxidation states and flexible complex coordination. In other words, transition metals can both give or take electrons, stabilize a transition state, and effect catalysis.

Iron, the most common element on earth (Figure 1.1A)(McDonough, 2001), fittingly, is also the most biologically abundant and important transition metal (Figure 1.1B)(Zoroddu et al., 2019). Essential to almost all known living species (Posey and Gherardini, 2000), it has even been postulated that the abundance of ferrous (II) iron on early earth gave rise to rudimentary metabolic cycles and contributed to the development of cellular life (Wachtershauser, 1990). Moving further in time, iron, at the root of photosynthesis, fashioned the contemporary oxygen rich world. In such an environment, iron also permitted cells to use oxygen to increase metabolic efficiency and helped give rise to complex eukaryotic life (Sheftel et al., 2012) (Figure 1.1C).

In all three domains of life, iron functions as a protein cofactor in three forms: iron-sulfur clusters (ISC), heme, and or directly bound iron. Within the annotated human iron proteome, 17% of proteins bind Fe-S clusters, whereas 48% bind heme and 35% bind iron metal (Andreini et al., 2018). Although the proportion of free iron binding

proteins stayed roughly constant across evolution, iron cofactor use shifted dramatically from ISCs toward heme. ISC proteins represent 68 ±12%, 47 ±12%, and 21 ±12% of the iron proteome in archea, bacteria, and eukarya, respectively. On the other hand, in these same superkingdoms, heme proteins are 13 ±14%, 22 ±12%, 47 ±19% of iron binding proteins (Andreini et al., 2007; Dupont et al., 2006). The lack of ISC gene expansion may relate to the use of other metals. Eukaryotes indeed do have far more zinc and copper binding proteins than prokaryotes (Andreini et al., 2006; Andreini et al., 2009) (Figure 1.1D). Because oxygen readily destabilizes ISCs whereas heme binds oxygen, this shift also reflects a changing environment. Accordingly, compared to aerobic bacteria, anaerobes have a higher ratio of Fe-S to heme-bound proteins. Nonetheless, despite their fragility in oxygen rich environments, ISC proteins still continue to support a variety of essential cellular processes in higher eukaryotes.

Among the most ancient of all cofactors, ISCs are complexes of iron bridged to sulfide ligands, most commonly in the form [4Fe-4S], [3Fe-4S], or [2Fe-2S]. Such an arrangement delocalizes the electron density across the entire cluster, lowers the reorganization energy of oxidation state interconversion, and increase the rate of electron transfer (Beinert, 2000; Sharma et al., 2014). As a result of these unique properties, ISCs are critical for oxidative phosphorylation and photosynthesis. In fact, human complex I contains 8 ISCs. Due to its special magnetochemistry, in which electrons can readily shift, ISCs also catalyze a variety of reactions. Nitrogen fixation and central carbon metabolism; DNA repair, replication, and nucleotide synthesis; protein translation and ribosomal biogenesis; and synthesis of cofactors molybopterin,

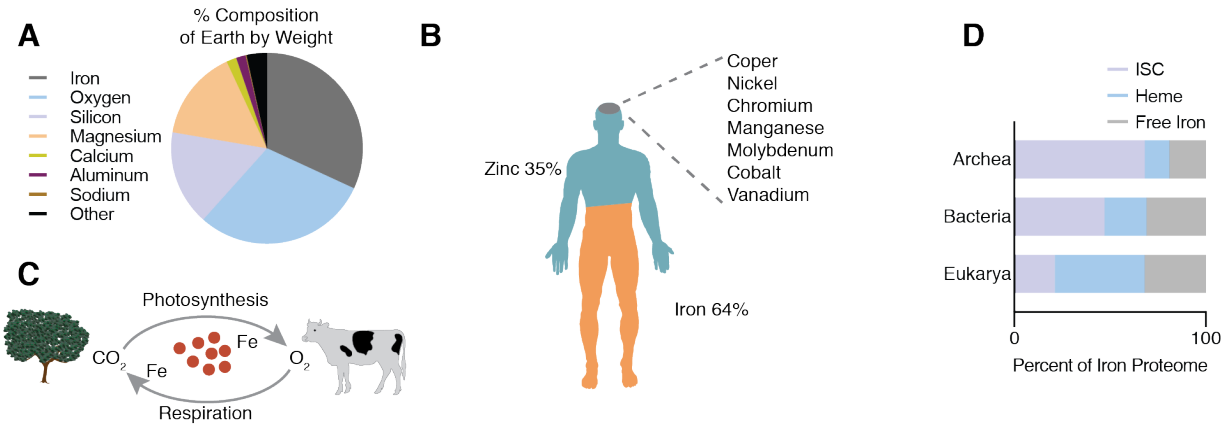


**Figure 1.1: Iron is essential for life**

**(A)** Elemental composition of earth. As shown here, iron is the most common element on earth. Adapted from McDonough, 2001

**(B)** Iron is also the most common metal in the human body. Adapted from (Zoroddu et al., 2019)

**(C)** Iron powers both photosynthesis and oxidative phosphorylation. Thus, iron is in part responsible for shaping the environment and taking advantage of it.

**(D)** Iron cofactor shift across evolution. From archea to bacteria to eukarya, cofactor use shifted from iron sulfur clusters to heme. Adapted from Andreini et al., 2007.

lipoate, and biotin all require ISCs. Although there are only ~70 known human ISC proteins, there are likely more to be discovered. While most ISCs are coordinated by cysteinyl sulfur, and to a lesser extent, histidine, arginine, and glutamine, there is no apparent sequence motif from which to computationally infer binding (Meyer, 2008). To date, there are also no high throughput experimental methods to determine ISC proteins (Maio and Rouault, 2016). The gold standard to establish ISC binding remains electron paramagnetic resonance or Mössbauer spectroscopy on purified proteins. These methods are not only labor intensive and technically challenging but quite problematic for weakly bound or labile ISCs.

The other major iron cofactor, heme, is iron encased in a tetrapyrrole porphyrin ring that has a unique capacity to bind and activate dioxygen as well as transport electrons. Through multiple degenerate spin crossover states, the porphyrin ring lowers the activation energy of iron to bind oxygen from approximately 75 KJ/mol to 15 KJ/mol

(Jensen and Ryde, 2004). Most prominently, heme binds and delivers oxygen as part of hemoglobin in erythrocytes and as part of myoglobin in musculoskeletal tissues. Catalytically, its ability to bind oxygen, activates cytochrome P450 enzymes which oxidize xenobiotics and play a role in steroidogenesis and lipid metabolism. This binding is also essential for the activity of catalases and peroxidases, which converts hydrogen peroxide to water. Within Soluble guanylyl cyclase (sGC), Heme also binds another biologically important gas through a similar mechanism, nitric oxide (NO), and effects a downstream cascade leading to vasodilation. Like ISCs, heme proteins Cytochrome bc1 also participate in electron transport as part of complex III. Heme is also the functional moiety of Cytochrome c which delivers electrons from complex III to complex IV.

In addition to complexed iron, enzymes, can use free ferrous iron to activate molecular oxygen and catalyze a wide range of reactions. In these proteins, iron is typically in octahedral symmetry in hexadentate coordination by the protein's histidine's imidazole side chain in a heme-like pattern. Of note, are the mononuclear iron dioxygenases, whose unique functions include aromatic ring cleavage, thiol oxygenation, and prolyl and lysyl hydroxylation.

Underscoring its essentiality and ubiquity but limited availability, iron sequestration often motivates biological competition. Because insoluble iron hydroxides readily form at atmospheric oxygen and neutral pH, microbes have devised different means of isolating scarce usable iron. One way, prevalent among bacteria and fungi, is

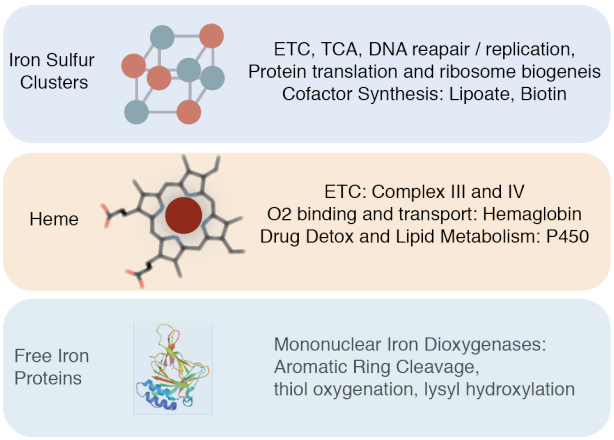


**Figure 1.2: Iron exists in three forms inside cells.**
PDB Structure of rat cysteine dioxygenase from https://www.rcsb.org/

to secrete low-molecular weight, high-affinity iron-trapping compounds known as siderophores. Iron-bound, self-secreted, siderophores can then be taken back-up through stereospecific transporters. This effectively steals iron away from competing organisms or hosts and confers a growth advantage. *Pseudomonas* typically out-competes *Burkholderia* because its siderophore, pyoverdine, binds iron at a higher affinity. Moreover, competition itself regulates siderophore production. The presence of S. *aureus* in a co-culture with P. *aeruginosa* causes P. *aeruginosa* to increase siderophore biosynthesis (Kramer et al., 2020). Competing organisms and pathogen hosts, however, have responded in kind. Some evolved receptors for xenosiderophore uptake. The gut bacteria B. *thetaiotaomicron* pilfers iron from Salmonella without the energic cost of producing a siderophore (Zhu et al., 2020). As iron is so precious, siderophores are often a key virulence factor to which hosts have also countered. The human protein LCN2 disables the E. *coli* siderophore, enterobactin, to prevent bacterial colonization. Iron can also be a limiting nutrient that determines the growth outcomes of

cancer cells versus healthy tissue. For instance, leptomeningeal metastases outcompete healthy tissue for the limited iron in the CSF by expressing LCN2 as well as its receptor SLC22A17 (Chi et al., 2020). Finally, medicine has repurposed siderophores as iron chelators. Deferoxamine, an FDA approved treatment for iron overdose, is a siderophore isolated from Streptomyces *pilosus* (Telfer et al., 2019). Taken together, the evolutionary arms race for iron strongly argues for its importance for growth across life.

Limited iron is not only detrimental for the single cell microbe but has devastating clinical consequences at the systemic level as well. Because of efficient recycling, human adults only require 1-2 mg of iron intake per day. Nonetheless iron depletion, caused by inadequate diet, excessive blood loss, diminished absorption, or increased demand, affects over two billion people and is the leading nutritional deficiency world-wide. Of these, nearly fifty percent have iron-deficiency anemia, which, often runs a chronic and under-diagnosed course. Due to reduced heme synthesis, this anemia is characterized by microcytic, hypochromic erythrocytes. Accompanying these hematological findings, iron deficiency anemia causes a constellation of vague symptoms. Symptoms including weakness and fatigue, as well as compromised immunity, increased risk for heart disease and impaired neurologic development in children suggest that iron is crucial for all tissues and not just erythrocytes. Iron deficiency is especially devastating during pregnancy, when iron is needed most. It impedes fetal development and increases the rate of fetal and maternal mortality (Camaschella, 2015).

**Excess iron is cytotoxic**

While insufficient levels hinder essential cellular functions, excess iron is cytotoxic. Because transition metals can toggle between stable oxidation states, free ferrous (II) iron, as well as other bivalent transition metals, can easily donate single electrons. Through the Fenton reaction, these electrons react with Hydrogen peroxide to produce hydroxyl and superoxide radicals, reactive oxygen species (ROS) that damage cellular lipids, DNA, and proteins. Subsequent accumulation of lipid peroxides triggers a specific type of programed cell death aptly termed ferroptosis (Dixon et al., 2012). Clinically, leveraging ferroptosis is an appealing cancer therapeutic strategy especially in “iron addicted” tumors. For example, chromophobe renal cell carcinomas, whose pathological hallmark is intense cytoplasmic iron staining, are particularly sensitive to lipid peroxidation (Yang and Stockwell, 2016).

In addition to a gain of function toxicity, altered relative concentrations of metals causes mis-metalation and a loss of function of metalloenzymes. Buildup of mitochondrial iron displaces manganese from Superoxide Dismutase 2 (SOD2) and causes mitochondrial dysfunction (Ganini et al., 2018). Similarly, accumulation of cytosolic iron, in a mouse model of hemochromatosis due to defective iron export, leads to a decrease of mitochondrial uptake of Cu, Zn, and Mn (Jouihan et al., 2008). Conversely, excess manganese dislocates iron from iron-binding enzymes and mimics iron starvation (Venkataramani et al., 2018). The neurotoxicity of chronic manganese exposure may, in fact, be a relative iron deficiency (Bjorklund et al., 2020). Given comparable chemical properties and similar in vitro protein affinities for iron,

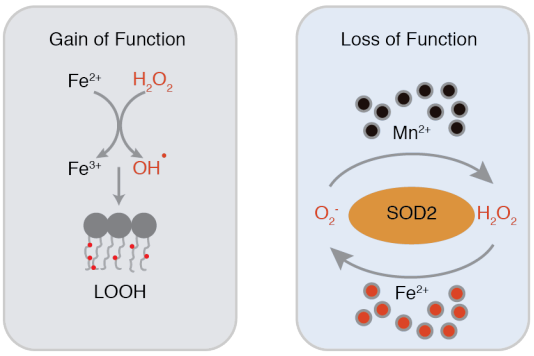


**Figure 1.3: Two models of iron toxicity.**

manganese, and other transition metals, the mechanism assuring proper enzyme metalation remains to be determined (Figure 1.3). This topic will be further explored in chapter 3.

To limit labile metal exposure, specialized proteins mediate transport, uptake and storage. In the blood, non-reactive ferric iron is bound to its carrier protein, Transferrin (TF), and is taken up through endocytosis of the Transferrin-Transferrin Receptor complex (Dautry-Varsat et al., 1983). In other secretory fluids, such as milk and saliva, Lactoferrin, binds iron (Hurlimann and Zuber, 1968). Excess intracellular ferrous iron is reduced by and stored inside ferritin, a multi-subunit globular protein complex, as an unreactive complex with phosphate and hydroxide inside ferritin (de Silva et al., 1993). In addition, poly(C) binding protein (PCBP1/2), a dual function RNA binding protein and iron chaperone (Shi et al., 2008), binds free iron in the cytosol and delivers it to iron binding proteins such as prolyl-hydroxylases (PHDs) (Nandal et al., 2011). Other metals such as zinc or copper can be safely stored in cysteine rich metallothioneins.

Small metabolites can also shield transition metals. Adequate phosphate levels are required for iron storage in ferritin (de Silva et al., 1993). Citrate, produced in the

TCA cycle, forms complexes with non-transferrin bound ferrous iron in the blood (Bakkeren et al., 1985). It is uncertain whether it plays a similar intracellular role. Gentisic acid (2,5-dihydroxybenzoic acid), tempers cytosolic iron levels and affects mitochondrial iron uptake or maintenance (Devireddy et al., 2010). While gentisic acid was initially thought to be the long sought-after mammalian iron siderophore, its actual iron binding affinity and true impact on iron homeostasis remain controversial (Correnti et al., 2012). Thiol containing compounds cysteine and glutathione, either free or attached to proteins, readily bind iron in vitro. It has even been hypothesized that this is one way to discriminate between the chemically similar iron and manganese. Iron binds to GSH at higher affinity than manganese (Hider and Kong, 2011). Nonetheless the cellular relevance and the degree of accessibility of specific metal-metabolite complexes requires future study. Work in chapters 2 and 3 will implicate a role for glutathione in tempering available intracellular iron levels.

Although a cell can safeguard against toxicity to a certain degree, excess iron has serious consequences on the tissue and organismal level. Iron overload due to unregulated absorption or storage, like iron deficiency, presents in patients with vague symptoms that may include fatigue and osteoporosis. The inability to assimilate iron into ISCs or heme leads to sideroblastic anemias, Friedrich's ataxia, and other syndromes whose pathological hallmark is mitochondrial iron accumulation. Largely managed with phlebotomy or chelation, unmitigated iron excess causes cirrhosis to liver, the storage site for iron. Overload also damages renal, cardiac and neurological tissues, tissues that are densely packed with mitochondria (Fleming and Ponka, 2012).

**Iron regulation is a delicate balance**

To balance of iron's indispensability and toxicity, cells coordinate sophisticated gene regulatory schemes. Iron is sensed and adjusted through the iron regulatory protein (IRP) system. IRP1, under iron replete conditions, binds an iron-sulfur cluster and functions as a cytosolic aconitase. When iron is limited, IRP1 loses its iron sulfur cluster, thereby, losing its aconitase activity and gaining RNA binding activity (Toth and Bridges, 1995). In contrast, IRP2 binds FXBL5 an F-box containing protein which contains a hemerythrin-like domain that directly binds iron and an 2Fe-2S cluster. Iron binding stabilizes FBXL5, which, in turn, promotes the ubiquitination and degradation of IRP2. Insufficient iron destabilizes FBLX5 and causes subsequent IRP2 accumulation (Wang et al., 2020).

Downstream of iron sensing, IRP1 and IRP2 bind mRNAs encoding proteins relevant for iron homeostasis that contain iron response elements (IRE), stem loop structures in their 5' or 3' UTRs. When iron levels are low, IRPs bind IREs in the 5' UTR and repress translation of mRNAs encoding proteins that lower functional iron levels such as components of the ferritin storage complex. Conversely, mRNAs encoding proteins that increase cellular iron, such as the transferrin receptor, contain IREs in the 3' UTR that destabilize and rapidly turn over the transcripts. When iron is limiting, however, IRPs bind to the 3' UTR to protect the transcript and promote translation (Anderson et al., 2012). For other metals, such as copper or zinc, cellular levels are sensed by the conserved Metal-regulatory transcription factor 1 (MTF1), which are activated by high metal concentrations levels. MTFs bind to specific DNA motifs to

increase transcription of mRNA encoding relevant proteins such as Metallothioneins (Ziller and Fraissinet-Tachet, 2018).

On a systemic level, four tissues coordinate an analogous feedback system. Duodenal enterocytes uptake iron and release it into the hepatic portal circulation through Ferroprotin-1 (FPN1/SLC40A1), an iron exporter on the basolateral membrane. As the first tissue to encounter ingested iron, the liver serves as a major storage site for iron in polymeric ferritin. Iron then enters the general circulation to be taken up by different tissues. The largest consumers of iron are erythroid precursor cells which assimilate iron into heme and incorporated heme into hemoglobin. In fact, iron availability is a major determinant of erythropoiesis. Senescent red cells are phagocytosed by reticulo-endothelial macrophages and iron released from heme is returned to the circulation through FPN1. Interestingly, the reticulo-endothelial macrophage iron pool is the most dynamic one as it recycles nearly 25mg of iron per day. Overseeing the systemic regulation is the liver, which, releases the hormone hepcidin when hepatic iron stores are high. Hepcidin binds to and inactivates ferroportin which prevents iron release from enterocytes and macrophages and tempers circulating iron levels (Muckenthaler et al., 2017; Nemeth et al., 2004).

In addition to its own regulation, iron availability interfaces with other cellular signaling pathways. Underscoring its importance in oxidative metabolism, low cellular iron activates hypoxia induced factor (HIF) signaling to increase transcription of glycolytic genes. Specifically, the prolyl hydroxylase requires ferrous iron to destabilize HIF1/2a under normoxic conditions. Thus, to a cell, low iron mimics low oxygen. Along

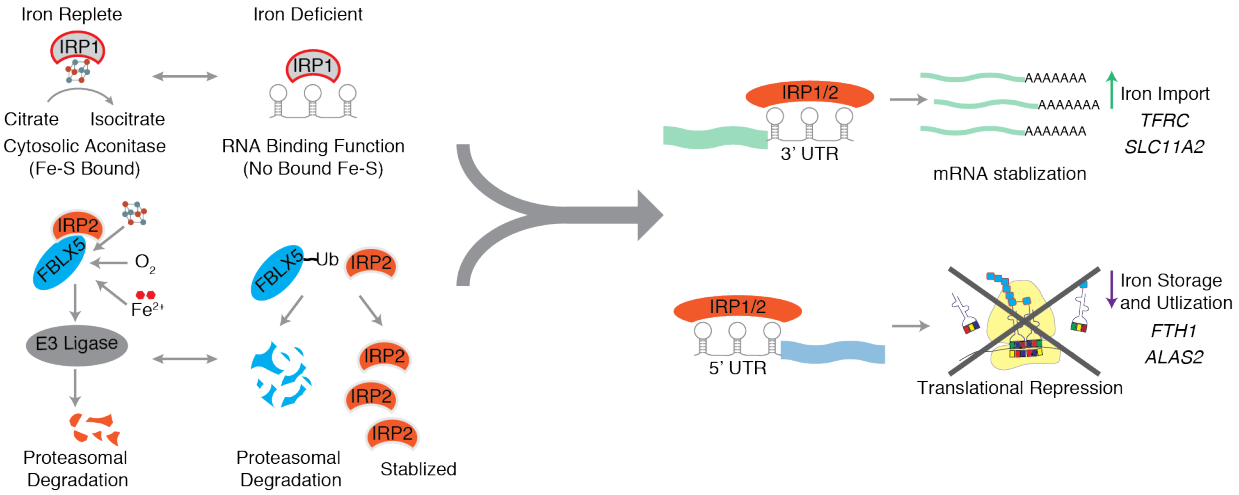


**Figure 1.4: IRP is the central iron regulation pathway**

these lines, oxidative stress signaling pathways similarly regulate and are regulated by iron. BACH1 forms a heterodimer with MAF proteins and is a transcriptional repressor of oxidative stress response genes. These include those encoding proteins involved in cysteine import and glutathione synthesis. Heme, however, binds to the C-terminal Cysteine-Proline domain, inactivates BACH1 and promotes its nuclear export. Without binding competition from BACH1, transcription factors such as NRF2 can promote expression of these same targets and increase cellular antioxidant defenses. Because, BACH1 also inhibits the transcription of Heme-Oxygenase 1 (HO-1), required for heme breakdown into bilirubin. Thus, heme-regulated BACH1 not only affects oxidative stress signaling but also adjusts heme levels.

Iron depletion also activates general stress and nutrient signaling pathways. Iron chelation leads to JNK and p38/MAPK signaling in an ERK independent manner (Yu and Richardson, 2011). The transferrin receptor (TfR1) is an mTOR target, linking the overall nutrient state of a cell with iron (Bayeva et al., 2012). In a similar vein, the protein Heme Regulated Inhibitor (HRI), activated by low cellular heme, phosphorylates

EIF2a to inhibit global translation and activate ATF4 and the integrated stress response (ISR) pathway. In other words, low heme indicates that the cellular metabolic deprivation and ATF4 responds by increasing transcription of genes related to nutrient uptake and synthesis (Zhang et al., 2019a).

**Lysosomes are hubs for iron storage and transport**

Another way to ensure proper metal detoxification and utilization is organellar compartmentation. Isolating metals from the larger cellular milieu prevents damage to cell membranes and the genome. Because many metalloproteins have similar affinities for different transition metals, maintaining distinct local metal concentrations also safeguards against mismetallation (Blaby-Haas and Merchant, 2014). Most importantly, compartmentation leverages the unique properties of each microenvironment. For iron, the routing and storage point is the lysosome, the organelle with the lowest pH, whereas assimilation occurs in, mitochondria, the most alkaline of all organelles.

Although mammals do have the ability to directly uptake free ferrous iron, most cellular iron is endocytosed as redox-inactive diferric-Transferrin attached to the transferrin receptor. The acidic environment of the endo-lysosomal lumen changes the conformation of Transferrin which releases $Fe^{3+}$ and the apo-Transferrin/Transferrin Receptor complex is recycled back to the cell surface (Lee and Goodfellow, 1998). The lysosomal NADPH-dependent STEAP family of metalloreductases then reduces ferric (III) to ferrous (II) iron. As expected, these enzymes have maximal activity at acidic pHs (Gauss et al., 2013). Finally, the Divalent Metal Transporter 2 (DMT2/SLC11A2) exports

$Fe^{2+}$ out of the lysosome coupled to proton symport. In addition to uptake, utilization of ferritin-stored ferric iron also requires functional lysosomes. In an NCOA4-dependent autophagic process known as ferritinophagy, lysosomal acid hydrolases digest ferritin and release its iron (Mancias et al., 2014). Taken together, iron release, reduction, and transport all rely on the vATPase-mediated acidic lysosomal pH.

Intriguingly, fungi and plants also store most of their iron in their lysosomal-like organelle, the vacuole. The fact that many of these organisms directly uptake free iron and do not require an acidic environment to remove iron from its carrier proteins points to another reason for lysosomal / vacuolar iron storage. Feasibly, the common denominator between animals, plants, and fungi is the low vacuolar pH. Such an environment solubilizes the more oxidatively inert ferric ($Fe^{3+}$) iron, normally insoluble at the near-neutral pH of the cytosol. In addition, at pH<5.5, iron is predominantly in its free form, un-complexed to cellular metabolites. The relationship between pH and ferric iron solubility plays further back in evolutionary time. Among the most acidophilic organisms, *Ferroplasma acidiphilum*, can grow at a pH of 1 and maintain an intracellular pH of 4.5-5. Like the vacuole or lysosome, *F. acidiphilum*, is characterized by the presence of oxidized ferric iron. In fact, its DNA ligase uses $Fe^{3+}$ instead of magnesium as co-factor (Ferrer et al., 2008).

Systemic iron regulation similarly takes advantage of pH. In mammals, most nutrient absorption occurs in the jejunum, whereas iron absorption takes place in the duodenum, the first and most acidic segment of the small intestine. Again, as most non-heme iron in stomach-digested food is $Fe^{3+}$, the acidic environment guarantees that the

ferric iron is soluble. Immediately before it is taken up, it is reduced on the surface of brush border cells so that the iron will be soluble inside the neutral cytosol. Once exported from the enterocyte, the ferrous iron is oxidized and then incorporated into transferrin where the protected iron is shuttled through the circulation. Indeed, patients, whose duodenal pH is increased such as in the setting of gastric bypass or H. pylori infection are at a higher risk for iron deficiency anemia.

Beyond its acidity, there are additional benefits of lysosome-controlled iron uptake and storage. Iron reduction and efflux from the lysosome or the vacuole allows a cell to quickly respond to iron replete or depleted conditions. As the hub for mTOR signaling, lysosomes or vacuoles can coordinate metal availability with the overall nutrient state of a cell (Zoncu et al., 2011). Finally, strict lysosomal storage of iron isolates it from the chemically similar, albeit more oxidatively inert, Manganese ($Mn^{2+}$), which is largely deposited in the Golgi apparatus in both fungi and animals (Das et al., 2019).

Even the earliest studies on lysosomes considered its importance in iron homeostasis. De Duve and colleagues noticed considerable iron enrichment in the “L-fractions” or lysosomal fractions in the original differential centrifugation experiments. In their initial electron micrographs, they noticed electron dense bodies in lysosomes and hypothesized that these were “ferritin-iron micelles” (Appelmans et al., 1955; Novikoff et al., 1956). Indeed, work ever since has pointed to an important role in iron homeostasis.

It is intriguing, however, to push this reasoning even further and speculate whether this is the key role of lysosomes. Interestingly, iron supplementation impairs

nuclear translocation of TFEB, the master transcriptional regulation of lysosomal biogenesis (Settembre et al., 2011; Xiao et al., 2018). This phenomenon might suggest when more free iron available there is less of a need for the organelle all together. This may even suggest that providing cellular iron is the essential function of lysosomal acidity. Chapter 2 will provide support for this hypothesis.

**Cellular iron trafficking and the labile iron pool**

Once released from the lysosome, labile iron, mostly $Fe^{2+}$, must be incorporated into non-heme iron binding proteins and safely and effectively transported into mitochondria for assimilation. Ferrous iron can diffuse through the cytosol to mitochondria either free or bound to chaperone proteins or metabolites. As mentioned above, these molecules may include, citrate, cysteine, or GSH. Alternatively, transient mitochondrial-lysosomal contacts, through a “kiss and run” mechanism, can directly deposit iron in the mitochondrial intermembrane space (Sheftel et al., 2007). It remains to be determined how the labile iron pool is sensed and whether this differs in cells with higher iron demands (tumors, erythrocyte precursors, etc.).

In either case, once inside the intermembrane space, Mitoferrin-1 (MFRN1/SLC25A37) or Mitoferrin-2 (MFRN2/SLC25A28) mediate ferrous iron transport into the matrix for assimilation (Shaw et al., 2006). It remains unresolved whether mitoferrin imports free, chaperoned, or complexed iron (Rouault, 2016).
Because the inner mitochondrial membrane is highly selective and does not allow for the free diffusion of polar molecules, mitoferrins represent a key regulatory breakpoint

for iron assimilation. For instance, during differentiation, erythroid cells regulate the half-life of MFRN1 to transiently increase hemoglobin production (Paradkar et al., 2009). In addition, Mitoferrin-1 Can form a complex with Ferrochelatase (FECH), a heme synthesis protein. This points to a coregulation of iron and assimilation (Chen et al., 2010).

**The mitochondrion is the site of iron assimilation**

*A priori*, the unique properties of the mitochondrion including its high pH, antioxidant pathways, and metabolic functions makes it an appealing site for iron assimilation into ISCs and heme. In contrast to lysosomes, its alkaline pH and negative inner membrane potential ensures that iron is more likely to remain soluble in its active ferrous (II) oxidation state, required for ISC biosynthesis, heme production and oxygen binding. Consequently, loss of mitochondrial membrane potential impairs Fe-S biosynthesis (Kispal et al., 1999; Veatch et al., 2009). Furthermore, at this higher pH, ferrous iron is most likely complexed with GSH over its other candidate metabolite ligands (Hider and Kong, 2011). Not only does this property maintain iron in its reduced oxidation state, but GSH-complexed iron may actually be necessary for ISC synthesis through glutaredoxin binding (Ouyang et al., 2018).

Second, although they produce a significant share of cellular ROS as electrons leak from the respiratory chain, mitochondria have countered with dedicated antioxidant pathways. The thioredoxin, superoxide dismutase, catalase and glutathione peroxidase pathways effectively buffer ROS toxicity from the iron-mediated Fenton reactions. The

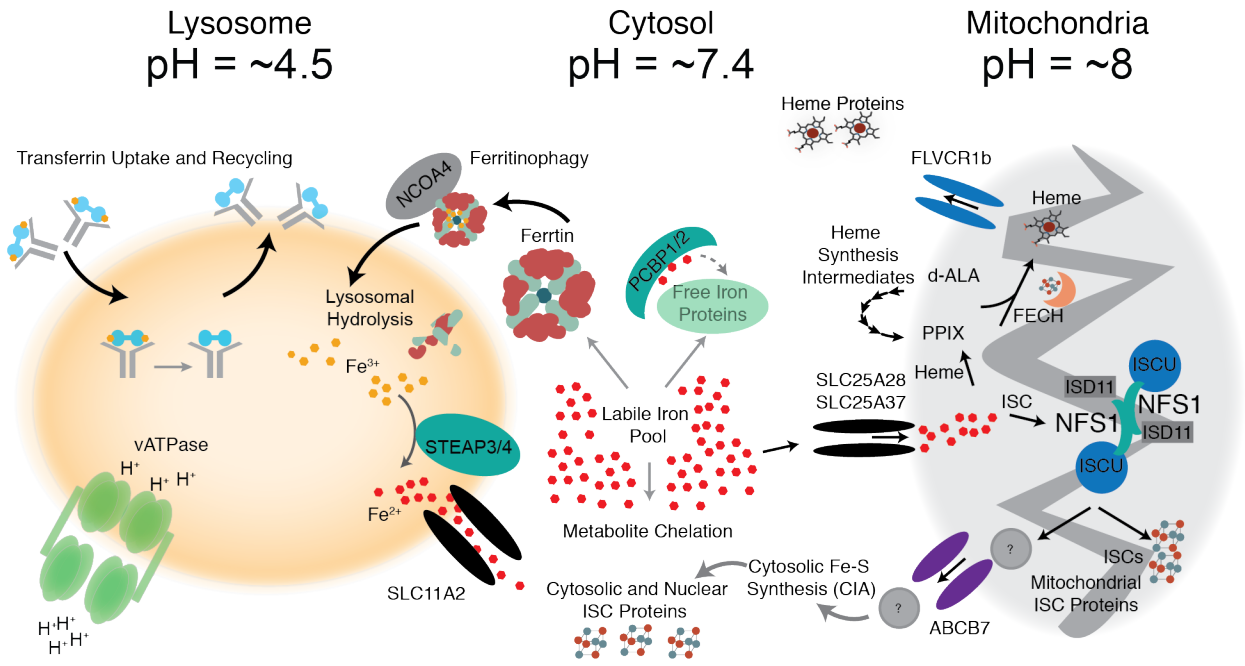


**Figure 1.5: From lysosomes to mitochondria, iron transport and assimilation.**

importance of maintaining these pathways in mitochondria is indicated by the relatively higher NADPH/NADP$^+$ ratio in mitochondria versus the cytosol (Sallin et al., 2018). Interestingly, uncoupled from its antioxidant role, inadequate NADPH levels impair ISC-cluster synthesis (Pain et al., 2010). Moreover, the generated ROS appears to be less mutagenic and leading to fewer base substitutions in mitochondrial DNA than to nuclear genome (Shokolenko et al., 2009).

Finally, as the centers of electron transport and oxidative metabolism, whose components require Fe-S clusters and heme, it is energetically most favorable to synthesize these cofactors where they are most needed. Along these lines, FECH, which converts protophyrin IX (PPIX) to heme, requires ISCs, for which mitochondria are a rich reservoir. Fittingly 7% of the mitochondrial proteome binds iron (Andreini et al., 2018).

Heme synthesis, in which the first and last two steps occur inside mitochondria, further capitalize on other non-intrinsic properties of this organelle. In the first reaction, ALAS1/2 catalyzes the condensation of glycine and succinyl coA to delta-aminoleveulinic acid (d-ALA) (Ponka et al., 2017). Because mitochondria are hubs for one carbon metabolism and TCA cycle, which produce glycine and succinyl coA, respectively, these precursors are readily available. Compartmentalized heme synthesis also provides a mechanism for efficient regulation as the first and last two steps occur in mitochondria while the intermediate steps occur in the cytosol. Indeed, in non-erythropoietic cells, high levels of mitochondrial heme inhibit ALAS1 activity.

The theme of iron assimilation is especially evident in the context of ISC synthesis. In mammals, the mitochondrially localized cysteine desulfurase, NFS1, as part of a larger complex with ISCU and ISD11, along with the activity of FXN, combines cysteine-derived sulfide with iron to generate a 2Fe-2S cluster. These ISCs are further matured into 4Fe-4S clusters and delivered to target proteins. The mitochondrial ISC synthesis pathway is also required for cytosolic ISCs even though mitochondria do not export intact clusters. Rather, ABCB7, exports an unknown ISC derivative which is subsequently converted into ISCs by the cytosolic iron sulfur cluster assembly (CIA) machinery (Kispal et al., 1999; Lill and Freibert, 2020). Nonetheless, mitochondria play at least some role in the formation of iron-sulfur clusters for all cellular proteins. Several evolutionary anomalies point to an even tighter relationship. Fascinatingly, *Monocercomonoidesis* is the only eukaryotic species without any mitochondrial remnants. It adopted a bacterial sulfur mobilization system (SUF), through a lateral

gene transfer event, to replace its lost mitochondrial ISC synthesis machinery (Karnkowska et al., 2016). In a similar vein, the intestinal parasite, Giardia *intestinalis*, does not have functional respiring mitochondria. Instead it has a rudimentary mitosome, a primitive organelle that has no functional pathways other than ISC synthesis (Pyrih et al., 2016). These examples instance strongly argues that ISC synthesis is one of the most important functions of mitochondria. Appropriately, without ISCs there are also no mitochondria. Not only does loss of ISC synthesis impair mitochondrial function and electron transport but it ablates the mitochondrial genome (Wilson and Roof, 1997) due to damage from accumulated unincorporated iron (Foury and Roganti, 2002).

Given the importance of mitochondrial iron, it is tantalizing to speculate that there may be, in addition to the IRP pathway, other organellar specific means of sensing iron and transducing that signal. Work in chapter 3 will attempt to identify mitochondrially localized protein switches that respond to alterations in cellular iron levels. It remains a fascinating possibility that mitochondria can autonomously respond to altered levels of iron to alter their metabolism.

Portions of Chapter 2 and 5 have been published as:

Weber, R.A., Yen, F.S., Nicholson, S.P.V., Alwaseem, H., Bayraktar, E.C., Alam, M., Timson, R.C., La, K., Abu-Remaileh, M., Molina, H., et al. (2020). Maintaining Iron Homeostasis Is the Key Role of Lysosomal Acidity for Cell Proliferation. Mol Cell 77, 645-655 e647

## CHAPTER 2: Maintaining iron homeostasis is the key role of lysosomal acidity for cell proliferation

### INTRODUCTION

Lysosomes are acidic membrane-bound organelles that play key roles in nutrient signaling, uptake and digestion of macromolecules, autophagy and recycling of intracellular components (Appelmans et al., 1955; Bainton, 1981; De Duve and Wattiaux, 1966; Lawrence and Zoncu, 2019). For activation and maximal enzyme activity, these catabolic reactions require the protected acidic environment of the lysosome, achieved through the proton-pumping action of the vacuolar-type ATPase (v-ATPase) (Mindell, 2012). Consistent with a critical role in maintaining cellular homeostasis, lysosomal pH dysfunction is associated with neurodegenerative diseases, aging, lysosomal storage disorders and compromised immunity (Bergmann et al., 2004; Klempner and Styrt, 1983; Koh et al., 2019; Platt et al., 2018).

A major ramification of inhibiting lysosomal acidification is impaired cell proliferation (Figure 2.1A; Figure 2.1B) (Manabe et al., 1993; Nishihara et al., 1995; Tsherniak et al., 2017). Accordingly, lysosome function is essential for the growth and progression of diverse human cancer types (Graham et al., 2014; Kinoshita et al., 1996; Ohta et al., 1998; Yan et al., 2016) and pH-disrupting lysosomotropic agents such as hydroxychloroquine are effective anti-cancer agents *in vitro* and *in vivo* (Yang et al., 2011). However, precisely why cells require acidic lysosomes to proliferate is not well-defined (Figure 2.1A). *A priori*, several explanations may underlie this phenomenon including compromised lysosomal membrane integrity and release of cytotoxic contents

(Boya and Kroemer, 2008), broad impairment of lysosomal functions such as autophagy and endocytosis, or depletion of critical nutrients upon disruption of lysosomal catabolism. Although the first two scenarios render cell proliferation in the absence of functional lysosomes infeasible, the third scenario would allow bypassing the necessity of lysosomal acidity upon supplementation of these limiting nutrients.

Here, using unbiased genetic screens, we identified metabolic processes that are required for cell proliferation under lysosomal pH inhibition. In particular, cholesterol synthesis, iron trafficking, and central carbon metabolism are essential when lysosomal pH is disrupted. Interestingly, we circumvented the requirement for functional lysosomes by simply providing cells with free iron, making iron, but not others, the limiting small molecule. Finally, because of iron depletion, lysosomal pH inhibition leads to mitochondrial dysfunction and a reliance on pyruvate dehydrogenase activity. Together, our results identify iron homeostasis as the key function of lysosomal acidity for cell proliferation.

## RESULTS

### A metabolism-focused CRISPR-Cas9 genetic screen identifies genes whose loss sensitizes cells to lysosomal pH inhibitors

To understand the impact of lysosomal acidity on cell metabolism, we first characterized the effects of two small molecules that raise lysosomal pH through different mechanisms. Ammonia, an endogenous toxic metabolite, disrupts lysosomal acidity by acting as a lysosomotropic weak base (Klempner and Styrt, 1983). Bafilomycin A1 (BafA1), a macrolide, potently inhibits the v-ATPase pump and prevents

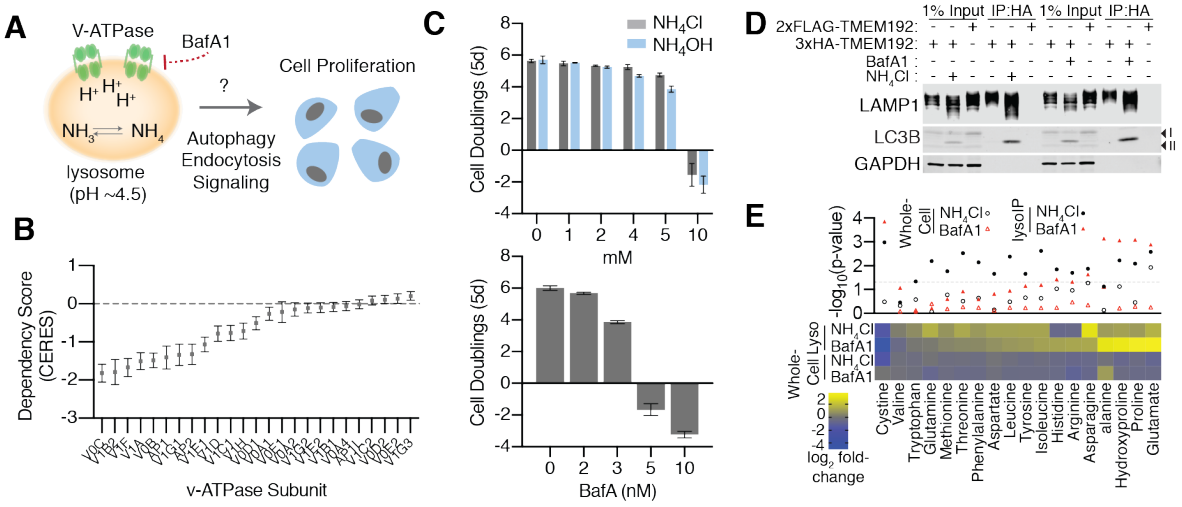


**Figure 2.1: Bafilomycin and ammonia increase lysosomal pH and inhibit cell proliferation**

(A) Lysosomal pH is essential for cells to proliferate. Ammonia and BafA1 disrupt lysosomal pH through different mechanisms.

(B) Plot of gene essentiality scores (DepMAP) of v-ATPase subunits.

(C) Dose-dependent effects of ammonia (top) and BafA1(bottom) on Jurkat cell proliferation (mean ± SD, n=3).

(D) Immunoblotting for lysosomal markers in input, purified lysosomes, or control immunoprecipitates in the presence or absence of BafA1 (10nm) or $NH_4Cl$ (10mM). Lysates were prepared from cells expressing 3xHA-tagged TMEM192 (HA-Lyso cells) or 2xFLAG-tagged TMEM192 (FLAG control cells).

(E) Metabolite abundance in cells or lysosomes upon treatment with BafA1 (10nm) or $NH_4Cl$ (10mM). *P*-values are for comparisons between metabolite concentrations in whole-cell or lysosome samples (upper panel) ($n = 3$ for each treatment; dotted line represents $P = 0.05$). Heat map of fold changes ($log_2$) in metabolite concentrations of treatment relative to control (lower panel).

acidification of lysosomes (Figure 2.1A) (Bowman et al., 1988). Both compounds cause cell death at high concentrations and only mildly inhibit cell proliferation at lower concentrations (Figure 2.1C). To determine whether these orthogonal means of increasing lysosomal pH affect metabolism in similar ways, we profiled polar metabolites in cell extracts and purified lysosomes (Figure 2.1D). Consistent with previous reports (Abu-Remaileh et al., 2017), disruption of lysosomal pH caused profound metabolic changes in the lysosomes, including increases in the levels of amino acids such as proline and asparagine and a profound decrease in lysosomal cystine (Figure 2.1E). While BafA1 led to more dramatic changes in lysosomal metabolites than ammonia, both caused changes in a wide variety of metabolites that generally trended in the same direction (Figure 2.1E). This suggested that the metabolic alterations, following these treatments, both inside lysosomes and larger cellular milieu, were generally similar.

Next, to systematically characterize the metabolic processes required for cell viability and proliferation under lysosomal dysfunction and to identify potentially limiting metabolites, we performed CRISPR/Cas9 genetic screens for metabolic genes whose loss potentiates the anti-proliferative effects of mild lysosomal pH disruption (Figure 2.2A). For these screens, we used a focused library targeting ~3,000 metabolism-related genes and measured the abundances of sgRNAs in the control, BafA1, or ammonia-treated Jurkat cells at the beginning and at the end of the 14-day culture period. For each gene, we calculated its score as the median $\log_2$ fold change in the

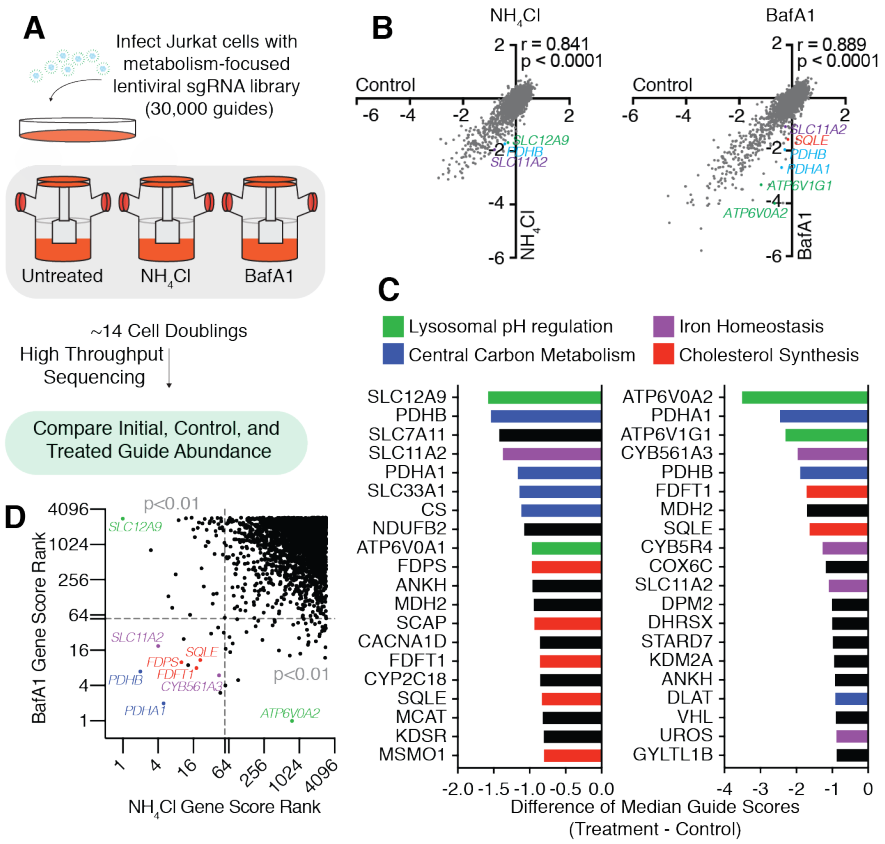


**Figure 2.2: A metabolism-focused CRISPR-Cas9 genetic screen identifies genes whose loss sensitizes cells to lysosomal pH inhibitors**

(A) Scheme describing the pooled CRISPR-based screen.

(B) Gene scores in untreated versus ammonia-treated (3mM) Jurkat cells (left). Gene scores in untreated versus BafA1-treated (3nM) Jurkat cells (right). The gene score is the median log2 fold change in the abundance of all sgRNAs targeting that gene during the culture period. Most genes, as well as non-targeting control sgRNAs, have similar scores in the presence or absence of the treatments.

(C) Top 20 genes scoring as differentially required upon ammonia (left) or BafA1 (right) treatment. Genes associated with lysosomal pH regulation are indicated in green, iron homeostasis in purple, central carbon metabolism in blue and cholesterol synthesis in red.

(D) Plot of gene score ranks from ammonia and BafA1 screens. Significant (P<0.01) unique hits in the BafA1 are in the lower right quartile, significant unique hits in the ammonia screen are in the upper left quartile, and significant hits shared in both screens are in the lower left quartile.

(E) Gene scores in untreated versus $NH_4Cl$-treated (3mM) KMS26 cells (top). The gene score is the median log2 fold change in the abundance of all sgRNAs targeting that gene during the culture period. Most genes, as well as non-targeting control sgRNAs, have similar scores in the presence or absence of the treatments. Top 20 genes scoring as differentially required upon ammonium chloride treatment (bottom). Genes associated with iron homeostasis are in purple, central carbon metabolism in blue, and cholesterol synthesis in red.

abundance of the 8-10 sgRNAs targeting the gene. Most genes and control sgRNAs scored similarly in the presence or absence of $NH_4Cl$ and Bafilomycin A1, confirming the robustness of the genetic screens (Figure 2.2B). Among the top-represented pathways shared between these screens were iron homeostasis, cholesterol biosynthesis and central carbon metabolism (Figure 2.2C).

In addition to these common pathways and consistent with the different modes of action for each molecule, our screens identified differentially essential genes under ammonia or BafA1 treatments (Figure 2.2D). The top-scoring gene unique to ammonia treatment was the cation transporter *SLC12A9* (Figure 2.2D and Figure 2.3A. Interestingly, the yeast ortholog of *SLC12A9* is localized to vacuoles and regulates vacuolar osmoregulation (Chapel et al., 2013; Petrezselyova et al., 2013), raising the possibility that *SLC12A9* may counteract the anti-proliferative effects of ammonia. Indeed, expression of sgRNAs targeting *SLC12A9* sensitized Jurkat cells to ammonia treatment (Figure 2.3B). Conversely, the top-scoring gene under BafA1 treatment was *ATP6V0A2*, a gene not essential upon ammonia treatment (Figure 2.2D; Figure 2.3 A,C). Similarly, expression of sgRNAs targeting *ATP6V0A2* sensitized Jurkat cells to BafA1 treatment (Figure 2.3D). As a non-essential component of the lysosomal v-

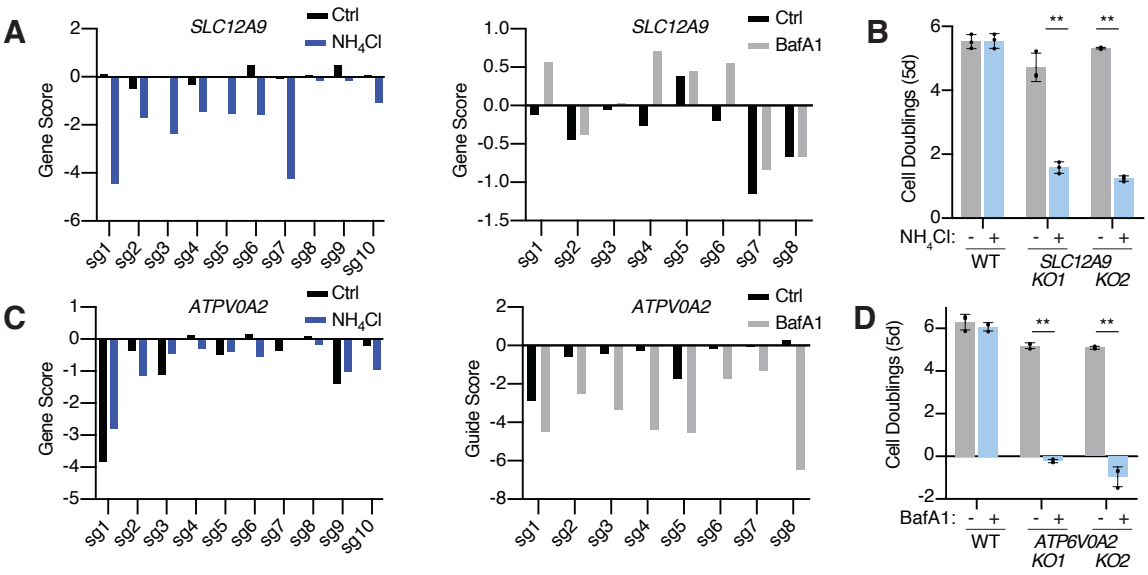


**Figure 2.3: Differentially essential genes under ammonia or BafA1 treatments**

(A) Guide score plots for guides targeting *SLC12A9* in $NH_4Cl$ (left) and BafA1 (right) negative genetic screens.

(B) Fold change in cell number (log2) of untreated (gray) or $NH_4Cl$ (4mM) treated (blue) parental or cells expressing two different guides targeting *SLC12A9* under treatment for 5 days (mean ± SD, n=3).

(C) Guide score plots for guides targeting *ATP6V0A2* in $NH_4Cl$ (left) and BafA1 (right) negative genetic screens.

(D) Fold change in cell number (log2) of untreated (gray) or BafA1 (3nM) treated (blue) parental or cells expressing two different guides targeting *ATP6V0A2* under treatment for 5 days (mean ± SD, n=3).

ATPase complex and adjacent to the BafA1 binding site, loss of *ATP6V0A2* may impact v-ATPase activity itself or the action of BafA1 on the complex. These experiments suggest that cancer cells rely on distinct metabolic pathways to survive under different modes of lysosomal pH inhibition.

**Upon lysosomal pH perturbation, cells are starved for cholesterol and iron**

Given their high scores in both genetic screens, we turned our focus to cholesterol synthesis and iron homeostasis. To study these pathways, in this context, we generated clonal knockout Jurkat cell lines for *SQLE* and *SLC11A2*, two scoring genes of cholesterol and iron metabolism, respectively. SQLE, a rate limiting enzyme of cholesterol synthesis, catalyzes the conversion of squalene to (S)-2,3-epoxysqualene (Garcia-Bermudez et al., 2019). On the other hand, SLC11A2 is a transmembrane glycoprotein involved in ferrous iron import across the plasma membrane as well as endosomal transport out of lysosomes (Hubert and Hentze, 2002). While both knockout cells, are viable and proliferate at similar rates to parental counterparts, non-lethal doses of ammonia and BafA1 profoundly affect cell viability and proliferation of the knockout cells (Figure 2.4A and 2.4C). In line with these observations, pharmacologic inhibition of SQLE by a small molecule inhibitor, NB-598, or iron chelation by deferoxamine (DFO) also sensitized Jurkat and several other cell lines to inhibition of lysosomal acidity with BafA1 as well as chloroquine, a lysosomotropic agent with anti-cancer properties (Figure 2.4B, D-H). These data validate the CRISPR screening

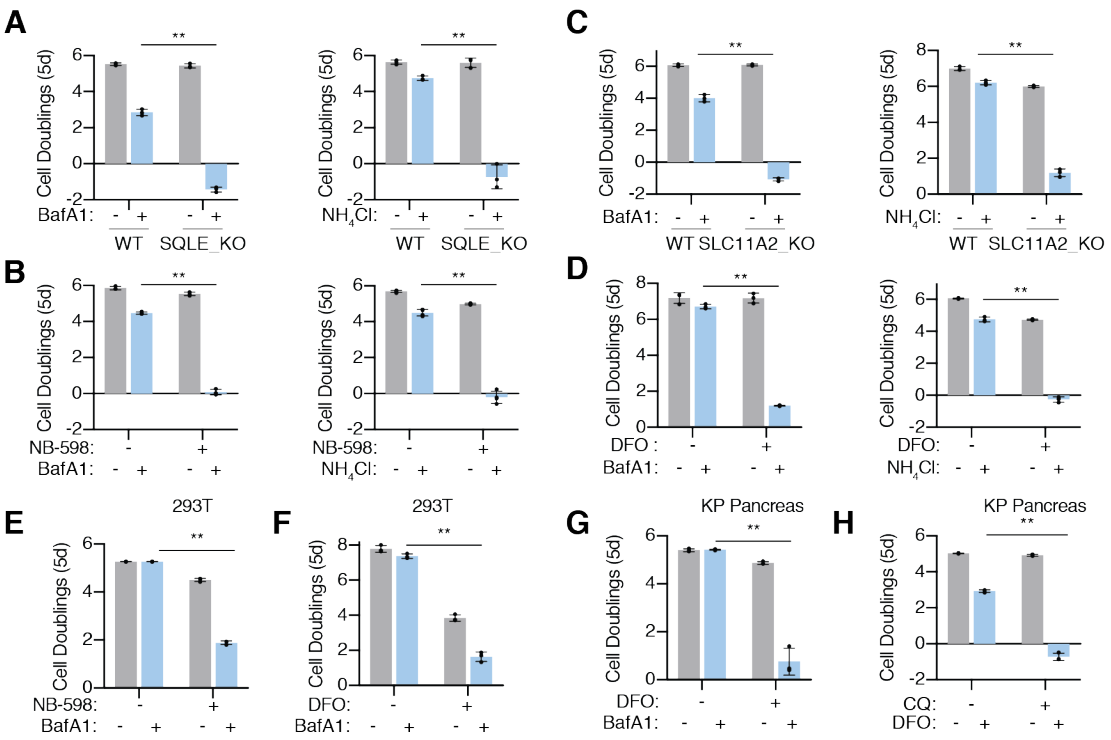


**Figure 2.4: Cholesterol synthesis and iron homeostasis are essential upon lysosomal dysfunction.**

(A) *SQLE* knockout cells die upon BafA1(2nm) (left) or ammonia (5mM) (right) treatment. Fold change in cell number (log2) of wild type and *SQLE* knockout Jurkat cells after treatment with indicated molecules for 5 days (mean ± SD, n=3, **p<0.05).

(B) Inhibition of SQLE using a small molecule inhibitor (NB-598; 10 $\mu$M) is synthetic lethal with lysosomal pH disruption. Fold change in cell number (log2) of untreated or NB-598 (10$\mu$M) treated Jurkat cells under BafA1(3nM) (left) or ammonia (5mM) (right) for 5 days (mean ± SD, n=3, **p<0.05).

(C) SLC11A2 knockout cells die upon BafA1(3nM) (left) or ammonia (4mM) treatment (right). Fold change in cell number (log2) of wild type and SLC11A2 knockout Jurkat cells after treatment with indicated molecules for 5 days (mean ± SD, n=3, **p<0.05).

(D) Iron chelation using deferoxamine (DFO) is synthetic lethal with lysosomal pH inhibition. Fold change in cell number (log2) of untreated or DFO (3$\mu$M) treated Jurkat cells under BafA1(3nM) (left) or ammonia (4mM) (right) for 5 days (mean ± SD, n=3, **p<0.05).

(E) NB-598-mediated inhibition of SQLE using a small molecule inhibitor (NB-598) is synthetic lethal with lysosomal pH disruption in 293T cells. Fold change in cell number (log2) of untreated or NB-598 (10$\mu$M) treated cells under BafA1(3nM) for 5 days (mean ± SD, n=3, **p<0.05).

(F) DFO-mediated iron chelation is synthetic lethal with lysosomal pH disruption in 293T cells. Fold change in cell number over 5 days (log2) of untreated or DFO (5$\mu$M) treated cells under BafA1(3nM). (mean ± SD, n=3, **p<0.05).

(G) DFO-mediated iron chelation is synthetic lethal with lysosomal pH disruption in mouse KP pancreas. Fold change in cell number over 5 days (log2) of untreated or DFO (5$\mu$M) treated cells under BafA1(3nM). (mean ± SD, n=3, **p<0.05).

(H) DFO-mediated iron chelation is synthetic lethal with the lysosomotropic drug, Chloroquine. Fold change in cell number over 5 days (log2) of untreated or DFO (10$\mu$M) treated cells under CQ (20$\mu$M) (mean ± SD, n=3, **p<0.05).

results and reveal that cells depend on de novo cholesterol synthesis and iron import to proliferate under lysosomal dysfunction.

As both iron and cholesterol are essential for cell proliferation, we next explored whether cells starve for them under lysosomal dysfunction. Mammalian cells control their cholesterol levels through a feedback regulatory system that senses intracellular cholesterol and activates membrane-bound sterol regulatory element binding proteins (SREBPs) (Mullen et al., 2016). Under cholesterol deprivation, SREBPs are cleaved from membranes, allowing them to translocate to the nucleus and activate transcription of its target genes. Interestingly, $NH_4Cl$ and BafA1 activate SREBP cleavage in Jurkat cells and upregulate expression of SREBP targets involved in de novo cholesterol synthesis, including *HMGCS1, HMGCR and SQLE* (Figure 2.5A and 2.5B). Furthermore, lanosterol, a surrogate for de novo cholesterol synthesis increases, suggesting that SREBP-mediated cholesterol synthesis is induced upon altering lysosomal pH (Figure 2.5C).

Cells treated with either BafA1 or iron chelator DFO were profoundly depleted of intracellular iron, as read out by a fluorescent iron probe (Figure 2.5D). Consequently, as is similarly observed under direct iron chelation (Vashisht et al., 2009), BafA1 activated the iron starvation cascade that prevents proteasomal degradation of Iron-Regulatory Protein 2 (IRP2), which, in turn, stabilizes mRNA of several iron-related genes, including *TFRC*, the cell surface transferrin receptor (Figure 2.5E). Because iron availability is also a major determinant for the synthesis of Fe-S clusters, a cofactor

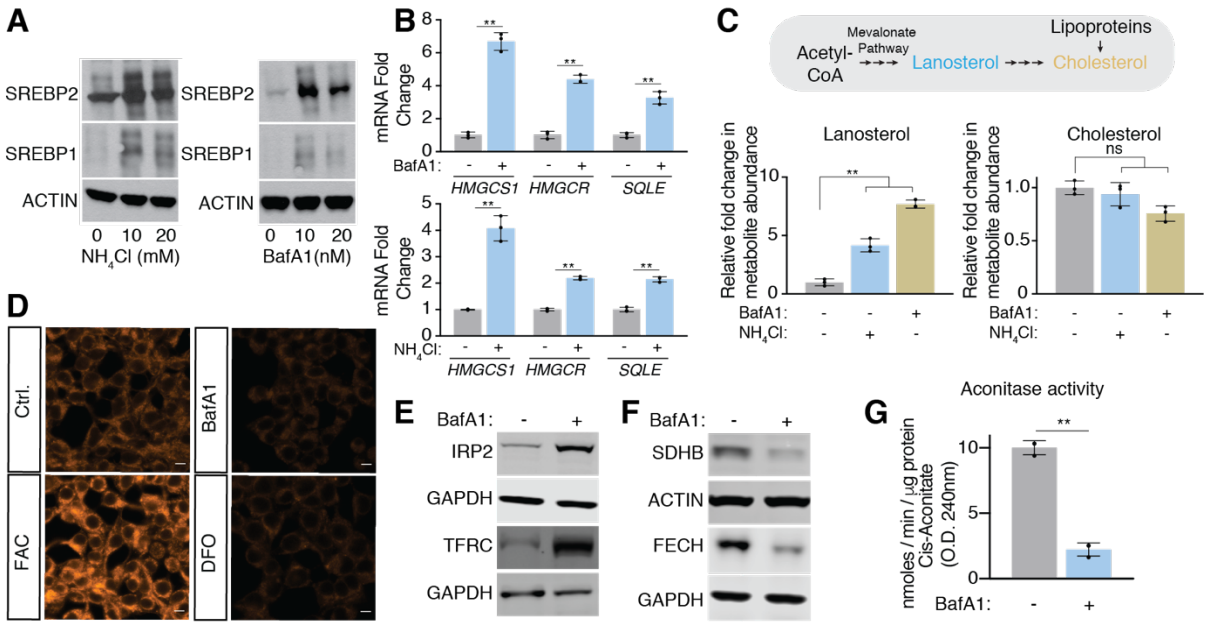


**Figure 2.5: Upon lysosomal pH dysfunction, cells activate iron and cholesterol starvation response pathways**

(A) Immunoblotting for SREBP-1 and -2 cleavage in Jurkat cells in the presence or absence of BafA1 (right) or ammonia (left).

(B) qRT-PCR analysis for the indicated mRNAs in the presence or absence of BafA1 (10nM) (top) or ammonia (10mM) (bottom) (mean ± SD, n=3, **p<0.05).

(C) Mevalonate pathway in human cells (top). Relative lanosterol or cholesterol levels in Jurkat cells treated with BafA1 (10nM) or ammonia (10mM) after a 24-hour treatment using LC-MS/MS (mean ± SD, for n=3, **p<0.05). All measurements are relative to untreated wild type Jurkat cells.

(D) Ferro-orange staining for intracellular $Fe^{2+}$ in 293T cells treated for 24h in the presence or absence of BafA1 (10nM) or DFO (100$\mu$M). Shown is one of five representative fields illustrating fluorescence intensity taken at identical exposures for each condition. Scale bar, 10 $\mu$m.

(E) Immunoblotting for the iron response pathway proteins (IRP2 and TFRC) in 293T cells in the presence or absence of BafA1 (10nM).

(F) Immunoblotting for iron sulfur cluster containing proteins SDHB and FECH in 293T cells in the presence or absence of BafA1 (10nM).

(G) Relative aconitase activity in 293T cells grown 24h in the presence or absence of BafA1 (10nM). (mean ± SD, for n=3, **p<0.05).

required for the stability and activity of several enzymes, we next sought to test whether lysosomal dysfunction affects iron sulfur cluster proteins, as well. Iron-sulfur clusters stabilize complex II of the electron transport chain and FECH, the final enzyme of the heme biosynthesis pathway. Additionally, this cofactor is required for the catalytic activity of aconitase. By all these measures, BafA1 treatments strongly decreases the stability or catalytic activity of these proteins (Figure 2.5F and 2.5G). Altogether our data indicate that human cells activate cholesterol synthesis and iron uptake to compensate for their decreased levels under inhibition of lysosomal acidification.

**Supplementation of iron, but not cholesterol, is sufficient to enable human cells to proliferate upon pharmacological and genetic disruption of lysosomal acidity**

The fact that lysosomal dysfunction induces iron and cholesterol starvation responses, we next asked whether one of these is a limiting metabolite and if we can restore cell proliferation by directly adding the deficient metabolite. To test this possibility, we supplemented Jurkat cell lines with varying levels of iron and cholesterol. While cholesterol addition completely rescued proliferation of *SQLE* knockout cells under cholesterol depletion, it did not enable cell proliferation when lysosomal pH is disrupted, suggesting that cholesterol is not a metabolic limitation (Figure 2.6A). In contrast, supplementation of media with iron in the form of ferric (III) ammonium citrate (FAC) or ferrous (II) ammonium sulfate (FAS) remarkably reversed the anti-proliferative effects of both ammonia and BafA1 on Jurkat cells (Figure 2.6B and 2.6C). Iron supplementation also protected other mouse and human cell types from lysosomal pH

inhibition, indicating a generalizable role for iron as a limiting metal for cell proliferation (Figure 2.6D). It should be noted that we supplemented the antioxidant, Ferrostatin-1, to cells grown in the presence of free iron to prevent any ROS-induced cytotoxicity. However, supplementation of Ferrostatin-1 alone without iron had no effect on BafA1 toxicity (Figure 2.6E).

The iron rescue experiments required iron concentrations that are higher than those found in standard media or human serum. This suggests that free iron uptake is not universally efficient among different cell types. To test this possibility, we overexpressed different isoforms of an iron transporter, SLC11A2 in Jurkat and Kras/p53 mouse cancer cell lines. SLC11A2.2 is more enriched on the plasma membrane and mediates absorption of non-transferrin bound iron while SLC11A2.1 is more enriched on endosomal/lysosomal membranes and mediates absorption of transferrin bound iron (Hubert and Hentze, 2002) (Figure 2.6G). Remarkably, only expression of the plasma membrane SLC11A2 isoform rescued cell viability of these cell lines, even in the absence of additional iron supplementation (Figure 2.6F-I). These experiments indicate that iron becomes limiting for cellular viability and proliferation under lysosomal pH dysfunction.

To expand upon our work with pharmacological inhibition of the v-ATPase to increase lysosomal pH, we next asked if iron supplementation rescues the proliferation of cells with genetic v-ATPase defects. Components of the lysosomal v-ATPases are among the most essential genes for proliferation in all cell lines (Figure 2.1B). However, why v-ATPases are required for proliferation is not completely clear. To explore this

question, we chose a highly essential v-ATPase component, *ATP6V0C* and generated conditionally v-ATPase deficient HEK293T cell lines using a CRISPR-Cas9 system based on Cas9 containing a destabilization domain (dd-Cas9) which is stablized by an FKBP12 synthetic ligand (Shield-1) (Senturk et al., 2017). Upon *ATP60VC* loss, HEK293T cells stop proliferating and can only be rescued upon addition of iron (Figure 2.6J). Interestingly, at the time of collection, we found that after Shield-1 addition, remaining 293T cells treated with iron had much lower amounts of ATP6V0C than those untreated counterparts, which is consistent with a selection against v-ATPase loss in cells in the absence of iron (Figure 2.6J). Collectively, these data demonstrate that iron is essential for the optimal survival and proliferation of cells lacking v-ATPase activity.

Finally, to explore the limiting role of iron further, we determined biologically relevant gene associations with v-ATPases using a publicly available RNAi genetic screening data of 712 cell lines (Figure 2.6K). As genes in the same functional pathways show parallel patterns of essentiality, variations in gene essentiality provides an efficient means for discovering genes with similar biological roles. Remarkably, correlation of essentiality gene scores revealed that the essentiality of *ATP6V0C* correlated highly significantly with that of other v-ATPase subunits as well as *TFRC*, but not with cholesterol uptake or cholesterol biosynthesis or other metabolic genes (Figure 2.6K). Of note, we could not use CRISPR based screens due to the essential role of v-ATPases upon complete loss in this system (Figure 2.1B). This further supports the limiting role of iron for cell proliferation under lysosomal dysfunction.

**Figure 2.6: Iron supplementation is sufficient to enable human cell proliferation upon pharmacological and genetic disruption of lysosomal pH**

(A) Cholesterol supplementation does not rescue anti-proliferative effects of Bafilomycin A1. Fold change in cell number (log2) of Jurkat cells in the absence and presence of free cholesterol (5$\mu$g/ml) after treatment with lipoprotein depleted serum (left) or full serum (right) for 5 days (mean ± SD, n=3, **p<0.05). In the full serum condition, cells were treated with or without BafA1(5nM) for the 5 days.

(B) Iron (Ferric (III) Ammonium Citrate (FAC)) rescues the proliferation of Jurkat cells under lysosomal dysfunction. Fold change in cell number (log2) in the presence or absence of $NH_4Cl$ (10mM) (left) or BafA1(5nM) (right) and/or FAC (0.1mg/ml) (blue) for 5 days (mean ± SD, n=3, **p<0.05).

(C) Ferrous (II) Ammonium Sulfate (FAS) also rescues proliferation of Jurkat cells under lysosomal pH inhibition. Fold change in cell number (log2) in the presence or absence of or BafA1(5nM) and/or FAS (0.1mg/ml) (blue) for 5 days (mean ± SD, n=3, **p<0.05).

(D) Iron supplementation at indicated concentrations rescues cell proliferation in HEK293T and HT cells under BafilomycinA1 concentrations up to 2$\mu$M. Fold change in cell number (log2) in the presence or absence of BafA1 and/or FAC (mean ± SD, n=3, **p<0.05).

(E) Ferrostatin-1 supplementation alone does not rescue anti-proliferative effects of Bafilomycin A1. Fold change in cell number (log2) of 293T and mouse pancreas cancer cells cultured in the absence and presence of ferrostatin (1$\mu$M) for 5 days.

(F) Expression of SLC11A2 isoform 2 is sufficient to enable proliferation of cells upon lysosomal pH inhibition. Expression of SLC11A2.2 rescues BafA1 sensitivity of the Kras/p53 mouse cancer cell lines. Immunoblot analysis of wild type and SLC11A2 expressing Kras p53 cell line (top). GAPDH was used as a loading control. Fold change in cell number (log2) of empty vector (EV) (gray) and SLC11A2 cDNA (blue) expressing cells after a 5-day treatment with BafA1(10nM) (blue) (mean ± SD, for n=3, **p<0.05) (bottom).

(G) Illustration of relative enrichment of SLC11A2 isoforms 1 or 2 for lysosomal or plasma membranes, respectively.

(H) In KP pancreas mouse cells, expression of SLC11A2.2 but not SLC11A2.1 is sufficient to rescue high dose BafA1 toxicity corresponding to Figure 3D. Fold change in cell number (log2) of untreated or BafA1 treated cells expressing, empty vector or SLC11A2 isoform 1 or isoform 2 (mean ± SD, n=3, **p<0.05).

(I) In Jurkat cells, expression of SLC11A2 potentiates iron rescue (0.1mg/ml) of BafA1 toxicity (mean ± SD, n=3, **p<0.05).

(J) Iron supplementation enables v-ATPase deficient cells to survive and proliferate. Immunoblots for *ATP6V0C* in HEK293T cell line infected with sg*ATP6V0C* virus in the presence or absence of Shield-1 (500 nM; top). Relative fold change in cell viability of indicated cancer cell lines grown in the absence and presence of Shield-1 and iron (FAC 0.1mg/ml) for 5 days (bottom) (mean ± SD, for n=3, **p<0.05). Representative bright-field micrographs of indicated cells after a 5-day BafA1 treatment in the absence or presence of iron (right).

(K) Schematic depicting co-essentiality analysis from RNAi screens using DepMAP data (top). Correlations of gene essentialities of *ATP6V0C* with other genes were calculated and ranked (bottom). TFRC is indicated in red and other VATPase subunits in green.

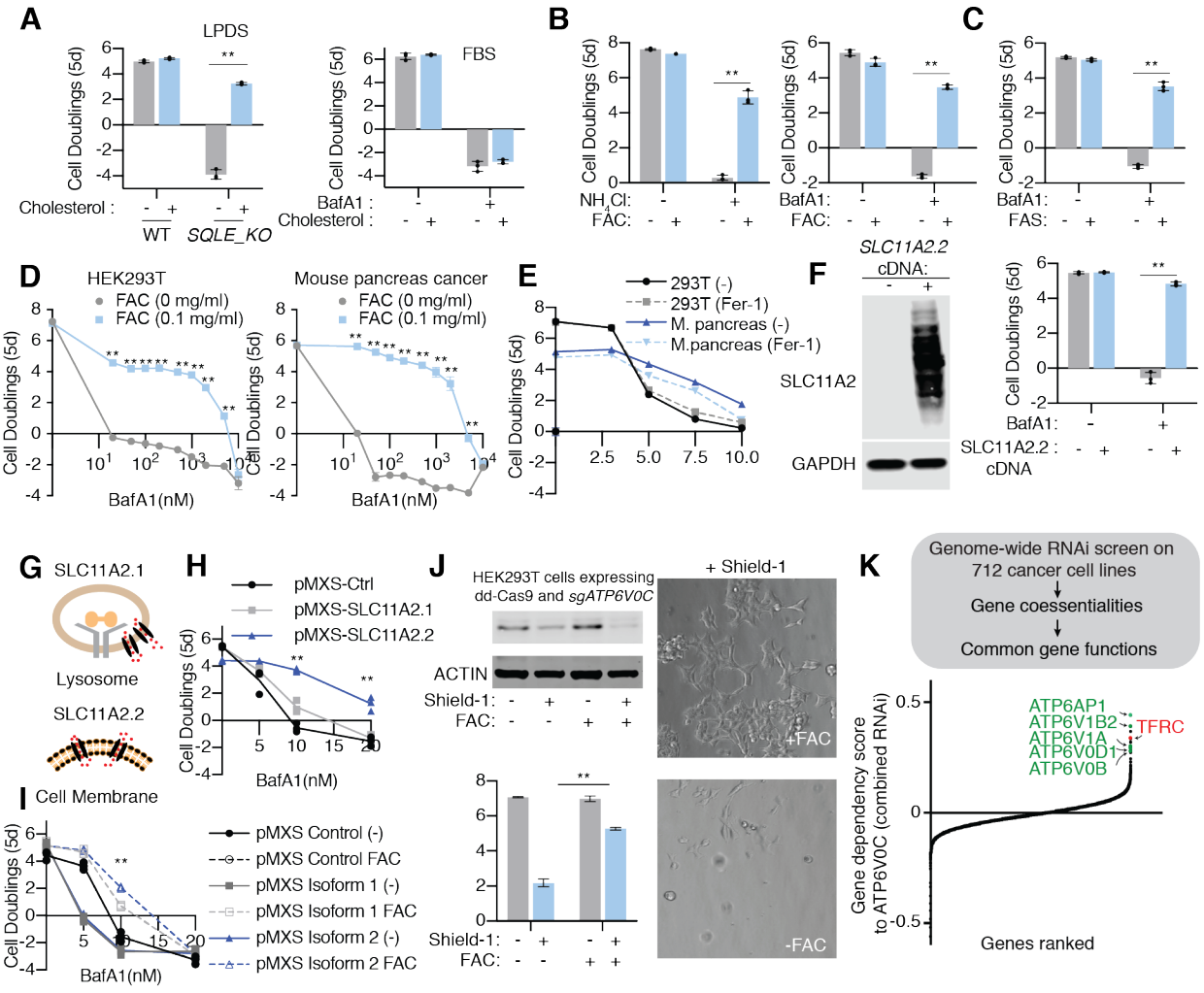
A
LPDS
FBS
Cell Doublings (5d)
Cholesterol :
WT
SQLE_KO
BafA1 :
B
NH4Cl:
FAC:
BafA1:
C
FAS:
D
HEK293T
Mouse pancreas cancer
FAC (0 mg/ml)
FAC (0.1 mg/ml)
BafA1(nM)
E
293T (-)
293T (Fer-1)
M. pancreas (-)
M.pancreas (Fer-1)
F
SLC11A2.2
cDNA:
SLC11A2
GAPDH
SLC11A2.2 :
cDNA
G
SLC11A2.1
Lysosome
SLC11A2.2
H
pMXS-Ctrl
pMXS-SLC11A2.1
pMXS-SLC11A2.2
I
Cell Membrane
pMXS Control (-)
pMXS Control FAC
pMXS Isoform 1 (-)
pMXS Isoform 1 FAC
pMXS Isoform 2 (-)
pMXS Isoform 2 FAC
J
HEK293T cells expressing
dd-Cas9 and sgATP6V0C
+ Shield-1
ACTIN
Shield-1:
FAC:
+FAC
-FAC
K
Genome-wide RNAi screen on
712 cancer cell lines
Gene coessentialities
Common gene functions
Gene dependency score
to ATP6V0C (combined RNAi)
Genes ranked
ATP6AP1
ATP6V1B2
ATP6V1A
ATP6V0D1
ATP6V0B
TFRC

**Iron-mediated rescue of cell proliferation is independent of signaling and metabolite changes associated with lysosomal acidity**

We next asked how iron rescues cell proliferation under inhibition of lysosomal acidification. Increasing cellular iron levels may restore v-ATPase associated functions or bypass entirely the need for a functional v-ATPase. Iron addition did not affect the broad metabolite changes previously observed under BafA1 treatment (Figure 2.1D; Figure 2.7A). In fact, the metabolite changes relative to untreated controls of BafA1 alone and BafA1 supplemented with iron are highly correlated (whole cell r=0.775, lysosome r = 0.996, $p<0.001$) (Figure 2.7A). Similarly, iron supplementation did not prevent inhibition of mTOR activity (Zoncu et al., 2011) (Figure 2.7B) or aggregation of LC3B-II, a surrogate for autophagy inhibition, following BafA1 treatment (Figure 2.7C).

Another function of lysosomal acidity is to enable the release of cargo following receptor-mediated endocytosis(Maxfield, 2014). One such process involves the uptake of transferrin-bound iron through the transferrin receptor. To test whether iron addition impacts the release of transferrin bound iron, we cultured cells in the presence of biotinylated holo-transferrin and measured levels of holo (unreleased iron) or apo (released iron) forms under lysosomal pH inhibition. These experiments showed an accumulation of holo-transferrin as indicated by a phoretic shift in the transferrin band, regardless of the iron supplementation and an increase in the ratio of holo- to apo-transferrin (Figure 2.7D). Notably, both the apo- and holo-transferrin levels decrease upon iron addition likely due to the downregulation of the transferrin receptor (TFRC) levels as part of the iron response pathway (Figure 2.7E)

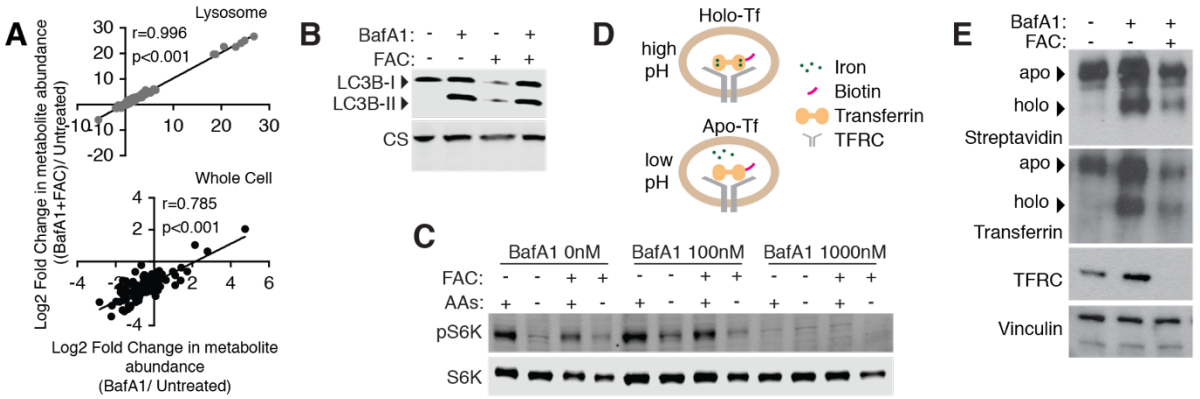


**Figure 2.7: Iron-mediated rescue of cell proliferation is independent of signaling and metabolite changes associated with lysosomal acidity**

(A) Comparison of metabolite abundance in 293T whole cells or purified lysosomes upon treatment with BafA1 (10nM) in the presence or absence of iron supplementation (FAC 0.4 mg/ml). (Lysosomes r= 0.996, p<0.001; Whole cell r=0.785, *P*<0.001)

(B) Immunoblotting for LC3B-II accumulation as an indicator of inhibition of autophagy completion in cells grown under BafA1 (10nM) or FAC (0.4mg/ml) for 24 hours.

(C) Immunoblots of pS6K and S6K as a readout of mTOR reactivation following amino acid starvation and feeding under indicated BafA1 concentrations in cells preincubated for 24 hours in the presence or absence of FAC (0.4mg/ml).

(D) Iron release from transferrin depends on lysosomal acidity. 293T lysates following uptake of biotinylated-holotransferrin, after 24-hour control, BafA1(10nM), or BafA1 and FAC (0.1mg/ml) treatments were immobilized on PDVF membranes. Immunoblotting for TF, TFRC, and vinculin loading controls or incubation of membrane with HRP-streptavidin

(Scheiber-Mojdehkar et al., 2004). Taken together, these data suggest that iron supplementation rescues cell proliferation independent of v-ATPase associated processes.

**Cellular processes restored by iron supplementation under lysosomal dysfunction**

We next sought to determine cellular processes restored by iron supplementation when lysosomal pH is disrupted. Iron supplementation increases intracellular iron levels, tempers the iron starvation response (Figure 2.8A,C) and reverses the destabilization of iron sulfur cluster (ISC)-containing proteins (Figure 2.8B). Consistent with the protective effect of low oxygen on iron-sulfur clusters (Alvarez et al., 2017; Ast et al., 2019), hypoxia also potentiated iron-mediated rescue under lysosomal pH inhibition (Figure 2.8C). Notably, BafA1 destabilizes many but not all iron sulfur cluster containing proteins likely due to variable affinities of proteins to ISCs or their differential stability upon loss of the ISC.

On a broader metabolic level, BafA1 treatment impairs baseline and maximal respiration, which was rescued by iron supplementation (Figure 2.8D). This phenotype is congruent with a destabilization of iron-sulfur cluster containing components of electron transport chain complexes I and II (Figure 2.8B). Nonetheless pyruvate supplementation, which normally rescues cytotoxicity and cell proliferation upon electron transport chain inhibition, does not restore cell viability upon lysosomal dysfunction (Figure 2.8F). This indicates that defects in the electron transport chain are

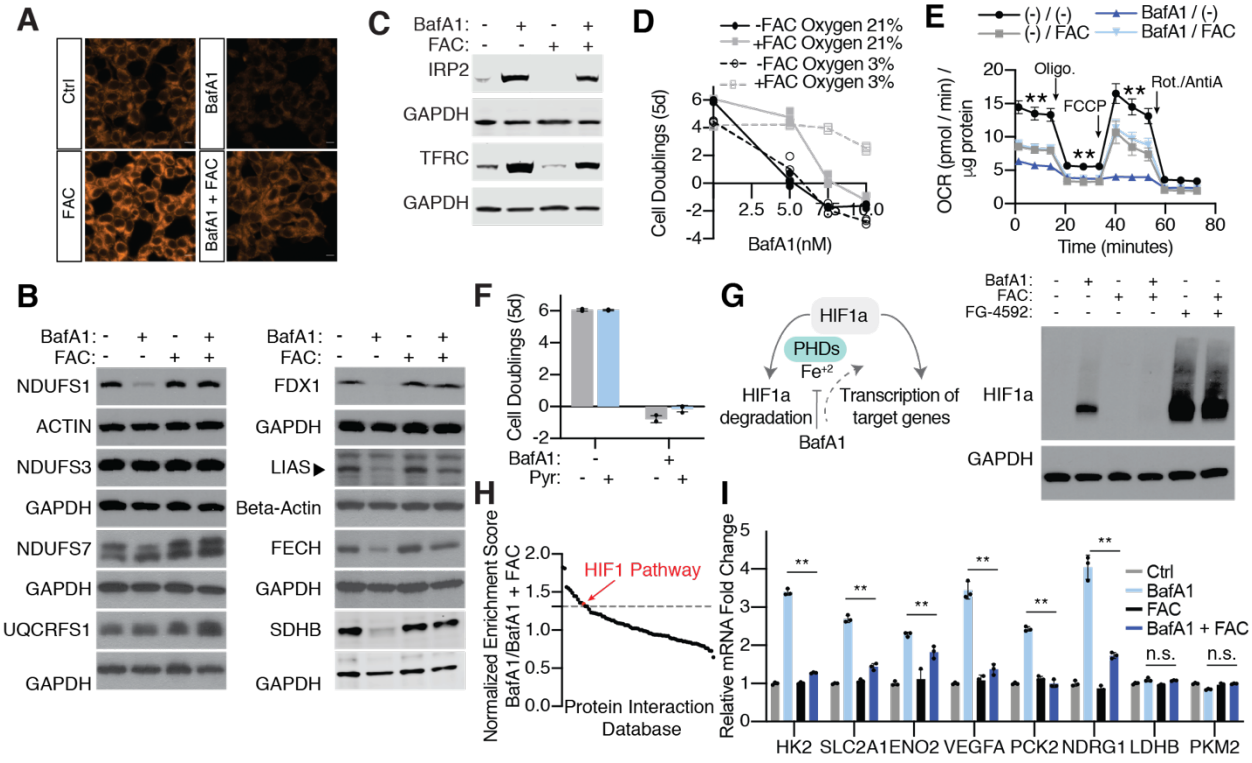


**Figure 2.8: Cellular processes restored by iron supplementation under lysosomal dysfunction**

(A) Ferro-orange staining for intracellular $Fe^{2+}$ in 293T cells cultured in the presence or absence of BafA1 (10nM) and/or FAC (0.1mg/ml). Shown is one of five representative fields illustrating fluorescence intensity taken at identical exposures for each condition. Scale bar, 10 $\mu$m.

(B) Immunoblotting for the indicated iron sulfur cluster containing proteins. GAPDH and Beta-actin are used as loading controls.

(C) Immunoblotting for the indicated iron response pathway proteins. GAPDH is used as a loading control.

(D) High oxygen levels disrupt iron sulfur clusters. Fold change in cell number (log2) of Jurkat cells in the absence and presence of FAC (0.1mg/mL) and hypoxia after treatment with indicated concentrations of BafA1 for 5 days (mean ± SD, n=3, **p<0.05).

(E) Oxygen consumption rate in 293T cells in the presence and absence of BafA1 (10nM) with and without iron supplementation (FAC 0.1mg/ml) (mean ± SD, n=9, **p<0.05).

(F) Pyruvate does not rescue anti-proliferative effects of Bafilomycin A1. Fold change in cell number (log2) of Jurkat cells grown in the absence or presence of BafA1 (5nM) and/or pyruvate (2mM) for 5 days (mean ± SD, n=3).

(G) Illustration of HIF1a stabilization by BafA1-mediated iron depletion (left). Immunoblotting for HIF1a in 293T cells grown in the presence or absence of BafA1 (10nM) and/or FAC (0.1mg/ml) (right).

(H) Gene set enrichment analysis (GSEA) on FPKM values from RNA-seq performed on 293T cells grown in the presence or absence of BafA1 (10nM) and/or FAC (0.1mg/ml). Graphed are normalized enrichment scores from 86 enriched pathways using the protein interaction database as the gene set. Values above the gray dotted line are pathways enriched with a nominal p-value <0.05. Highlighted in red is the HIF1a pathway.

(I) Relative expression of canonical HIF1a transcription targets (FPKM normalized to Control) from above RNA-seq experiment (mean ± SD, n=3, **p<0.05).

one of many metabolic changes due to iron depletion but not the sole cause of cytotoxicity.

Iron availability also controls the stability of hypoxia inducible factors (HIFs) through inhibition of the activity of Fe(II) dependent prolyl hydroxylases (PHDs) (Figure 2.6G) (Siegert et al., 2015). Consistent with previous observations (Miles et al., 2017), BafA1 treatment increases HIF1a protein levels (Figure 2.8G) and the expression of the canonical HIF1a target genes (Figure 2.8H,I), a phenotype largely reverted by iron supplementation. Altogether, these experiments suggest that iron supplementation restores mitochondrial function and HIF activation status under lysosomal pH disruption.

**Lysosomal acidity couples iron homeostasis to mitochondrial citrate synthesis**

As cells starve for iron and depend on it to proliferate under inhibition of lysosomal acidification, we next sought to determine the genes or processes required for cell proliferation specifically due to iron starvation. To study this in an unbiased manner, we performed a complementary CRISPR/Cas9 metabolism screen under direct iron chelation and identified genes that are essential under both lysosomal dysfunction and deferoxamine (DFO)-mediated iron depletion (Figure 2.9A-D). While sgRNAs targeting genes encoding enzymes and transporters related to iron metabolism, including *SLC11A2*, *CYB561A3* and the mitochondrial iron carriers *SLC25A28* and *SLC25A37*, were significantly depleted, none of the cholesterol synthesis-related genes or non-essential v-ATPase components scored upon DFO treatment (Figure 2.9C). Conversely, several genes encoding Krebs cycle enzymes including citrate synthase

(*CS*) and pyruvate dehydrogenase (*PDHA1*, *PDHB*) scored in both BafA1 and DFO screens (Figure 2.9C).

To study the essential role of pyruvate dehydrogenase under iron depletion further, we generated clonal Jurkat knockout cells of *PDHA1* and *PDHB*, components of the pyruvate dehydrogenase complex. Confirming the screen results, loss of *PDHB* or *PDHA1* sensitized cells to the treatment of ammonia, BafA1 as well as DFO (Figure 2.9 E-G). PDH-mediated acetyl-coA production may feed into cholesterol synthesis, de novo lipid synthesis or antioxidant capacity (Pietrocola et al., 2015), but none of these processes scored in the DFO screen (Figure 2.9B). Furthermore, *PDHB* null cells proliferate normally in lipoprotein depleted serum (LPDS) and antioxidant addition does not rescue their sensitivity to lysosomal dysfunction, ruling out the possibility that sensitivity of *PDHB* null cells is due to deficits in cholesterol synthesis or antioxidant capacity (Figure 2.9H,I). These data suggest that limiting iron is the basis of PDHB knockout sensitivity to lysosomal pH inhibition.

We next asked why cells depend on PDH activity to proliferate under lysosomal pH dysfunction and iron depletion. As PDH catalyzes the conversion of glucose-derived pyruvate to acetyl-coA, one possibility is that PDH may be necessary to contribute carbon units for the TCA cycle upon lysosomal dysfunction. Glucose tracing experiments showed a significant decrease in downstream TCA cycle intermediates (m+2) from isotopically labeled glucose, raising the possibility that cells do not require PDH activity to fill in their TCA cycle. Despite this decrease, glucose-labeled citrate levels were not affected by lysosomal pH inhibition, suggesting a block in aconitase

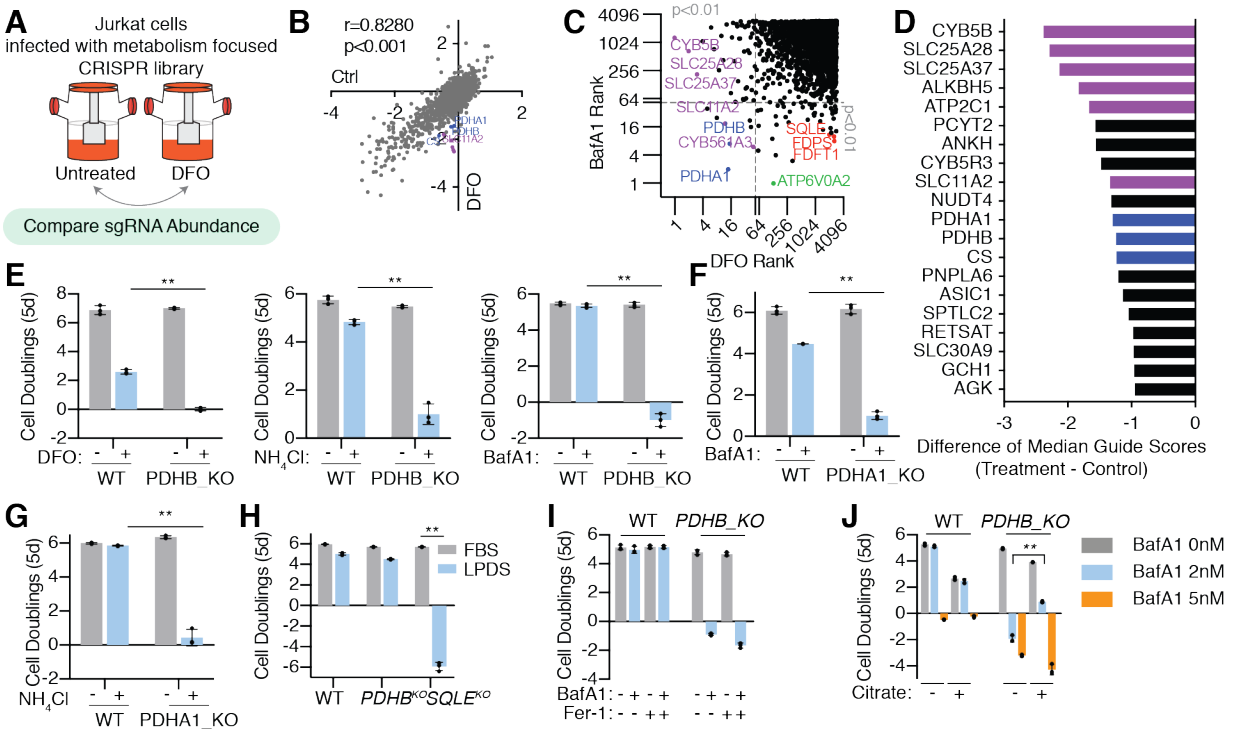


**Figure 2.9: Lysosomal pH couples iron homeostasis to mitochondrial citrate synthesis**

(A) Scheme of CRISPR/Cas9 screen of deferoxamine-mediated iron chelation (left).

(B) Gene scores in untreated versus DFO-treated (2$\mu$M) Jurkat cells. The gene score is the median log2 fold change in the abundance of all sgRNAs targeting that gene during the culture period. Most genes, as well as non-targeting control sgRNAs, have similar scores in the presence or absence of the treatments.

(C) Plot of gene score ranks from DFO and BafA1 screens (right). Significant (P<0.01) unique hits in the BafA1 are in the lower right quartile, significant unique hits in the DFO screen are in the upper left quartile, and significant hits shared in both screens are in the lower left quartile.

(D) Top 20 genes scoring as differentially required upon DFO treatment. Genes associated with iron homeostasis are in purple and central carbon metabolism in blue.

(E) Fold change in cell number (log2) of parental and PDHB null Jurkat cells in the absence or presence of DFO (3$\mu$M), BafA1 (3nM) and ammonia (4mM) for 5 days (mean ± SD, n=3, **p<0.05).

(F) Fold change in cell number (log2) of parental and PDHA1 null Jurkat cells in the absence and presence of BafA1 (3nM) (top) and ammonia (5mM) (bottom) for 5 days (mean ± SD, n=3, **p<0.05).

(G) Fold change in cell number (log2) of parental and PDHA1 null Jurkat cells in the absence and presence of ammonia (5mM) (bottom) for 5 days (mean ± SD, n=3, **p<0.05).

(H) Fold change in cell number (log2) of parental, PDHB null and SQLE null Jurkat cells grown for 5 days in media containing 10% FBS or 10% lipoprotein depleted serum. (mean ± SD, n=3, **p<0.05).

(I) Fold change in cell number (log2) of Jurkat cells grown in the absence or presence of antioxidant Ferrostastin-1 (Fer-1) (1$\mu$M) or BafA1 (2nM)

(J) Fold change in cell number (log2) of parental and PDHB null cells cultured in the absence or presence of Sodium Citrate (10mM) and indicated concentrations of BafA1 grown for 5 days (mean ± SD, n=3, **p<0.05).

activity (Figure 2.10A). Notably, we could partially rescue sensitivity of PDHB null cells with citrate supplementation (Figure 2.9J). Taken together, these data indicate that lysosomal acidity is required for PDH-independent citrate synthesis.

One way to obtain citrate, independent of pyruvate, is from glutamine through reductive carboxylation (Rajagopalan et al., 2015). In reductive carboxylation, citrate is synthesized from glutamine through the reversal of isocitrate dehydrogenase and aconitase. Indeed, we observe a significant enrichment of fractional citrate labeling (m+5) from glutamine in *PDHB* null cells compared to parental controls. Similar to our glucose tracing results, BafA1 treatment decreases total and m+5 labeled citrate levels in *PDHB* null cells. Consistent with the block in reductive carboxylation in WT cells, BafA1 leads to a decrease in m+5 labeled citrate, but not other isotopically labeled intermediates (Figure 2.10 B). As reductive carboxylation depends on mitochondrial aconitase (ACO2), an iron sulfur containing protein, we hypothesized that lysosomal pH dysfunction depletes cellular iron, which, in turn, may inhibit aconitase activity and indirectly decrease citrate availability in *PDHB* null cells. In line with this possibility, BafA1 significantly decreases aconitase activity, which is restored by iron supplementation (Figure 2.10C). Furthermore, iron supplementation rescues the sensitivity of *PDHB* knockout Jurkat cells to BafA1 (Figure 2.10D). These results couple lysosomal acidity to mitochondrial citrate synthesis and indicate the functional requirement for lysosomes in central carbon metabolism through iron homeostasis.

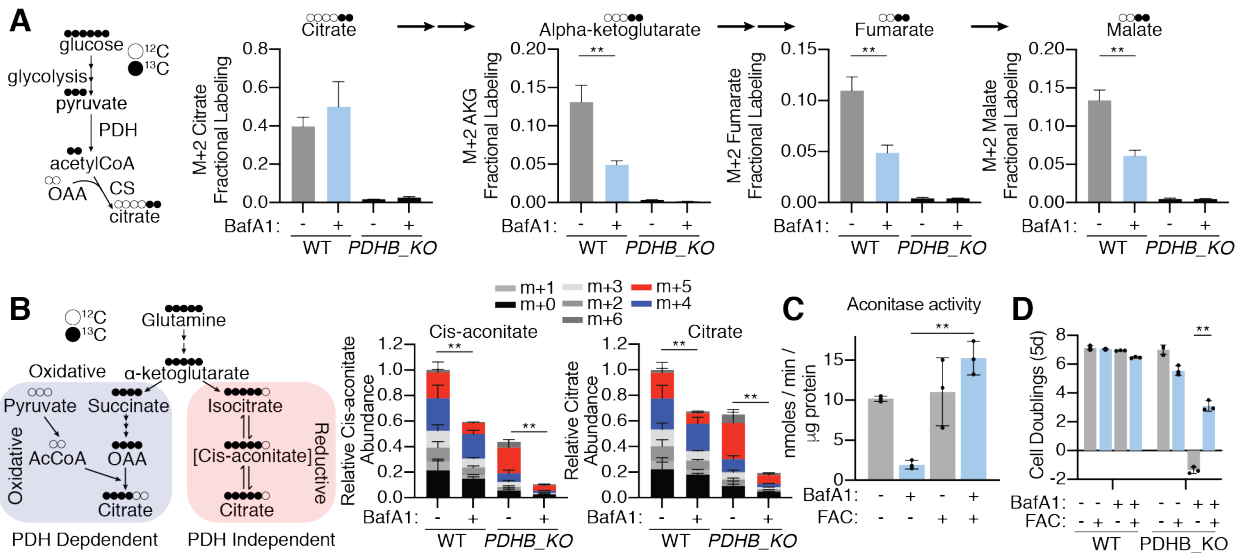


**Figure 2.10: Pyruvate dehydrogenase activity becomes essential under lysosomal dysfunction**

(A) Illustration of isotopic labeling of citrate and downstream TCA cycle intermediates from U$^{13}$C-glucose (left). m+2 fraction labeled metabolites represent the pyruvate dehydrogenase-dependent labeling. Citrate and downstream TCA cycle intermediates m+2 fraction labeling in WT and PDHB-null Jurkat cells in the absence and presence of BafA1 (10nM) (right) (mean ± SD, n=3, **p<0.05).

(B) Illustration of isotopic labeling of citrate and cis-aconitate from U$^{13}$C-glutamine (left). m+4 labeled citrate and cis-aconitate represents the oxidative, pyruvate dehydrogenase dependent and aconitase independent labeling. m+5 labeled citrate represents the oxidative, pyruvate dehydrogenase independent and aconitase dependent labeling. Relative citrate and cis-aconitate abundance in WT and PDHB-null Jurkat cells in the absence and presence of BafA1 (10nM) (right) (mean ± SD, n=3, **p<0.05). Statistical analysis was performed on the m+5 fraction.

(C) Aconitase activity in 293T cells in the presence and absence of BafA1 (10nM) with and without iron supplementation (FAC 0.1mg/ml) (mean ± SD, n=3, **p<0.05).

(D) Fold change in cell number (log2) of parental and PDHB null Jurkat cells in the absence and presence of Ferric ammonium citrate (0.1mg/ml) and BafA1 (3nM) (mean ± SD, n=3, **p<0.05).

## DISCUSSION

Cancer cells rely on functional acidic lysosomes to proliferate. While lysosomes are important for many anabolic and catabolic functions, our data indicates maintenance of cellular iron levels as the key function of lysosomes in cancer cell proliferation (Figure 2.11). As iron supplementation bypasses the need for functional and acidic lysosomes, our data strongly argues against a cytotoxic death upon release of degradative enzymes or heavy metals. Indeed, iron supplementation does not restore canonical lysosomal functions such as nutrient signaling and autophagy, but rather rescues defects associated with iron depletion. Lysosomal dysfunction, through iron depletion, leads to profound alterations in metabolism including electron transport chain impairment, induction of hypoxia-like signaling, and changes in central carbon metabolism. These results link lysosomal function to mitochondrial metabolism and, in part, explain the mitochondrial defects seen in mammalian cells under lysosomal dysfunction.

While many of the same signaling pathways and metabolic changes were elicited, the differences between iron depletion due to inhibition of lysosomal pH versus direct iron chelation warrant further consideration. A potential difference may be the type of cell death caused by lysosomal dysfunction versus iron chelation. The cell death mechanism of iron chelation is not well understood. It may be related to autophagy, paradoxical ferroptosis, necrosis, or apoptosis (Greene et al., 2002; Rainey et al., 2019). Similarly, conflicting reports have characterized Bafilomycin mediated cell death as caspase-dependent apoptosis (Greene et al., 2002; Nakashima et al., 2003),

caspase-independent apoptosis (Yuan et al., 2015), or necrosis (Yambire et al., 2019). Careful follow-up experiments using apoptosis or necrosis inhibitors and precise measurements of cell death markers will determine which, if any, of the above cell death pathways is triggered and whether it varies according to cell type and treatment conditions.

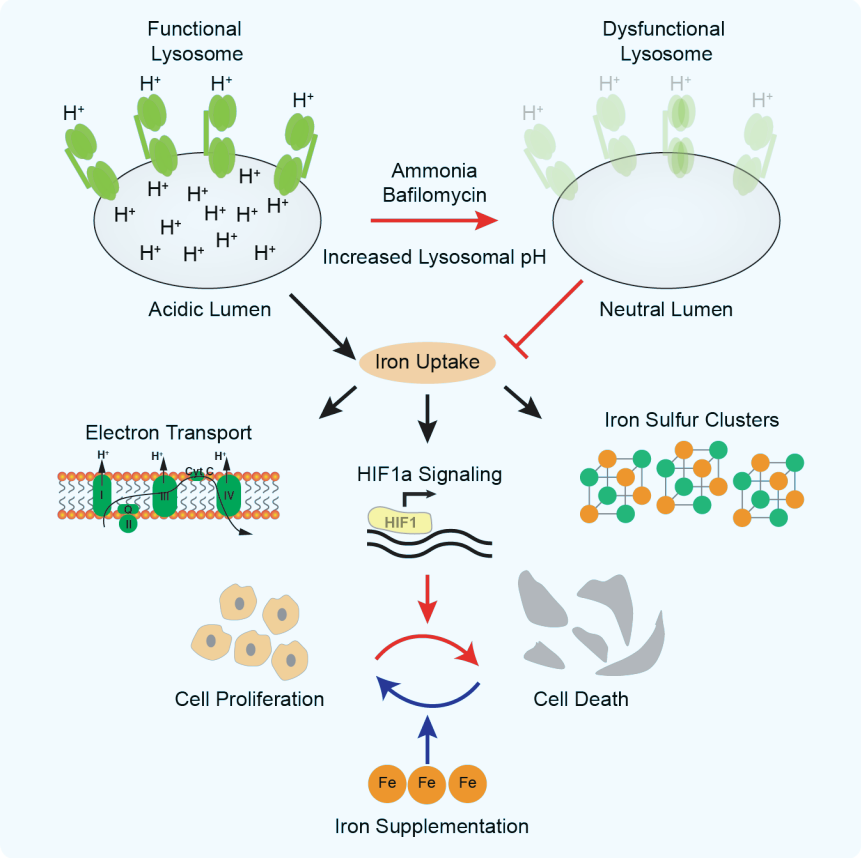


**Figure 2.11: Maintaining iron homeostasis is the key role of lysosomal acidity for mitochondrial function and cell proliferation**
Schematic illustrating that although lysosomes participate in many key cellular functions including cholesterol uptake, signaling, and autophagy, iron is the essential function of lysosomes for cell proliferation under inhibition of lysosomal acidification. In this context, iron supplementation restores loss of iron sulfur clusters and is sufficient to rescue cell viability and proliferation.

Although iron rescues cell death and enables proliferation in a culture system, on an organismal-developmental level, vATPase activity and lysosomal acidity is likely required for embryonic progression and differentiation. In fact, in a pilot experiment, iron supplementation did not rescue a developmental blockade in worms expressing an RNAi targeting several vATPase components (data not shown). In mice, ATP6V0C knockouts are early embryonically lethal and survive to either the pre-implantation stage (E2.5-3.5) (Inoue et al., 1999) or immediate post-implantation stage (E4.5) (Sun-Wada et al., 2000). This is likely made possible by the presence of maternal mRNA or slow protein turnover. Similarly, 1-cell mouse embryos treated with Bafilomycin can advance no further than the 4-cell stage (Tsukamoto et al., 2013). If iron supplementation extends the survival and development of *ATP6V0C*$^{-/-}$ or Bafilomycin-treated cultured embryos, one could pinpoint at what stage is lysosomal acidity needed for iron homeostasis and at what stage is it needed for other purposes.

Nonetheless the lysosomal-iron axis is likely to be physiologically relevant in other contexts. A striking example is how asymmetric lysosomal division determines hematopoietic stem cell differentiation. Remarkably daughter cells that contained fewer lysosomes had vastly increased transferrin receptor protein levels, indicating an iron starvation response (Loeffler et al., 2019). Consistent with a strong effect of direct iron chelation on hematopoiesis and differentiation (Kao et al., 2018), lysosomal depletion is an efficient way to quickly modulate intracellular iron signaling and drive differentiation.

Our findings may also have useful therapeutic implications in the setting of lysosomal dysfunction across a variety of clinical contexts. Lysosomal pH disrupting

drugs such as hydroxychloroquine show efficacy in clinical trials for several cancer types. While some of the efficacy was attributed to the reliance of some tumors on catabolic pathways such as macropinocytosis and autophagy, our data raise the possibility that iron may be a limiting metal for cancer cells when treated with these inhibitors. Indeed, iron chelation and chloroquine were synthetically lethal in a mouse pancreatic cancer model (Figure 2.3H). Similarly, toxic ammonia may build up at concentrations in the tumor microenvironment that may disrupt lysosomal acidity (Spinelli et al., 2017) and can also be exploited by targeting iron homeostasis in these tumors. Building upon these, it should be determined whether iron deficient diets, mitochondrial citrate synthesis inhibition, or iron chelation can be target these tumors, especially in combination with lysosomal pH inhibitors.

Iron dysregulation may also play an important role in the pathology of lysosomal storage diseases (LSDs). These diseases are often caused by recessive loss of function mutations in genes encoding lysosomal catabolic enzymes leading to consequent toxic accumulation of cellular metabolites (Platt et al., 2018). For instance, mutations in acid alpha-glucosidase (GAA) cause Pompe disease, a typical LSD characterized by lysosomal accumulation of glycogen with patients clinically presenting with cardiomegaly, hypotonia, and myopathy. Interestingly, in addition to these clinical symptoms, iron depletion and loss of mitochondrial activity were also present in a mouse model of Pompe's disease. Moreover, these phenotypes were partially rescued when mice were fed an iron rich chow (Yambire et al., 2019). Further studies using

animal and cellular models of LSDs will determine to what extent a particular lysosomal insult affects iron metabolism.

## CHAPTER 3: The roles of Golgi and mitochondria in iron homeostasis

### INTRODUCTION

While chapter 2 underscored the significance of functional lysosomes, several indications point to the importance of other organelles in iron homeostasis. As noted earlier, mitochondria assimilate iron into ISCs and heme, which, respectively affect IRP and BACH1 gene regulation. They can also store iron in mitochondrial ferritin, a brain and testes specific protein (Gao and Chang, 2014). In addition to mitochondria, Golgi play a role in IRP protein (Patton et al., 2005) and ferritinophagy machinery docking (Goodwin et al., 2017). Furthermore, ZIP13, whose stability is post-translationally regulated by iron (Xu et al., 2019), stores excess iron inside the endoplasmic reticulum (ER) for eventual secretion (Xiao et al., 2014). More generally, these organelles also play a role in detoxification and storage of other transition metals (Gudekar et al., 2020). Precisely how other organelles contribute to iron homeostasis has not yet been fully explored.

Iron is also crucial for organellar function. Within each compartment, there are iron binding proteins. However, the type of bound iron is unevenly distributed. The ER iron proteome, of which cytochrome P450 proteins comprise a significant portion, mostly binds heme. In contrast, most iron binding proteins in mitochondria, the site of the electron transport chain and the TCA cycle, are ISC proteins (Andreini et al., 2018). Moreover, the ER and mitochondrial iron proteomes (7%) are also significantly enriched for iron binding compared to the total proteome (2%). Given the ubiquity of organellar iron binding proteins but specificity of type, we would expect altered cellular iron to

affect organellar proteomes in unique ways. These changes, however, have not been examined at fine organellar resolution.

Here, we utilized a two-pronged approach to characterize the role of organelles in the setting of altered iron. First, using CRISPR/Cas9 based genetic screens, we identified manganese import as the essential function of Golgi in the context of iron chelation. Second, leveraging unbiased proteomics on purified mitochondria, we found a metabolite transport protein, regulated by iron, whose loss of function profoundly decreased mitochondrial glutathione.

## RESULTS

### CRISPR/Cas9 genetic screens identify organellar metal transport as essential under limited iron

To systematically characterize iron overload, using the aforementioned sgRNA library targeting ~3000 metabolism-related genes, we performed a CRISPR/Cas9 genetic screen on Jurkat cells grown in the presence of Ferric Ammonium Citrate (FAC) and the antioxidant Ferrostain (Fer-1). We reasoned that co-treatment with an anti-oxidant would mitigate iron mediated ferroptosis and allow the screen to focus narrowly on iron metabolism. After ~14 doublings, we compared the iron treated versus control gene scores, defined as the median normalized $\log_2$ fold change of 8-10 guides compared to the initial. The most positive hit, a gene essential under control conditions but not under supplemented iron, was *TFRC*, the transferrin receptor. This argues that in the presence of excess iron, cells may bypass the transferrin uptake system and use

the divalent metal (DMT), zinc transporter (ZIP), or another alternative system. Conversely, the gene normally dispensable but now essential was Ferritin Heavy Chain 1(FTH1), a major storage site for cellular iron (Figure 3.1A). The presence of these genes, in addition to good correlation scores indicated that the screen was technically well-executed. Disappointingly, little additional biological novelty emerged from this screen.

Instead, we refocused on iron chelation. We reconsidered our previously performed negative DFO screens (Figure 2.7B; Figure 3.1B). Here cells were grown under sublethal doses of this iron chelator. We also performed a positive or “drop-out” DFO screen in which cells were grown under lethal doses of DFO to find genes whose loss of function enabled cells to grow under minimal iron (Figure 3.1C). The gene whose guides were most enriched in the positive screen and at the positive end of the negative screen, was *MRP1/ABCC1*. ABCC1 is a plasma membrane efflux pump, responsible for exporting a variety of substrates including chemotherapeutic drugs. As such, it is a major determinant of drug resistance in cancer. Another top hit was *GCLM*, a component of the glutathione synthesis complex. These two genes are likely functionally related as ABCC1 exports glutathionylated xenobiotics and heavy metals substrates as well as glutathione itself (Cao et al., 2019; Johnson and Chen, 2017). We speculate that cellular glutathione levels may affect usable iron in the cell and that glutathionylated iron can be exported by ABCC1. Another possibility is drug specific. The activity of this efflux pump and/or glutathione may be required for DFO specific chelation.

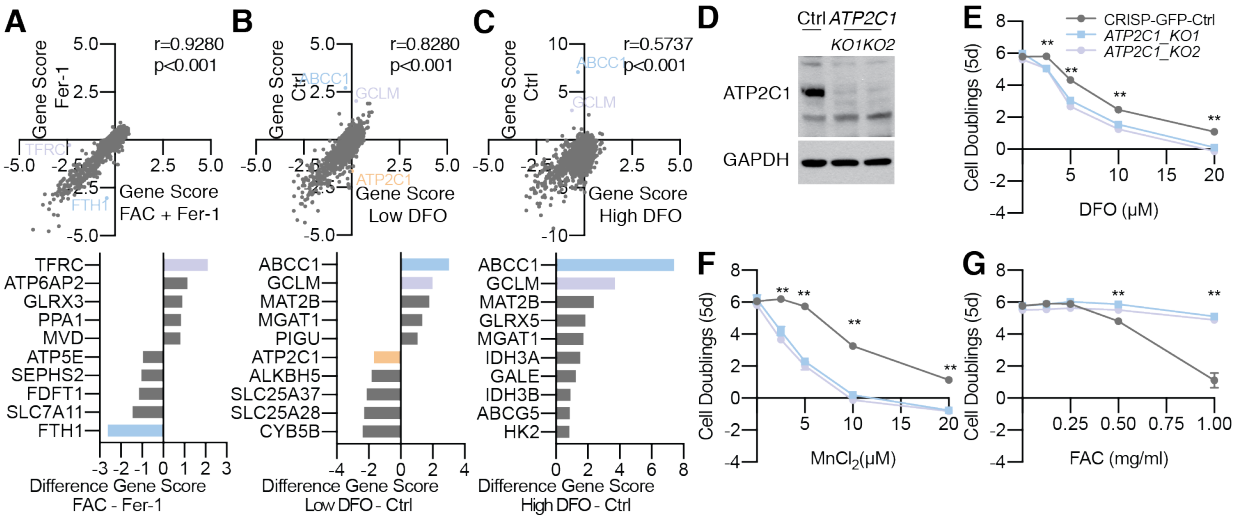


**Figure 3.1: CRISPR/Cas9 genetic screens identify organellar metal transport as essential under limited iron**

(A) Gene scores in Fer-1 (1$\mu$M) versus FAC (0.1mg/ml) + Fer-1 treated Jurkat cells. The gene score is the median log2 fold change in the abundance of all sgRNAs targeting that gene during the culture period. Most genes, as well as non-targeting control sgRNAs, have similar scores in the presence or absence of the treatments.

(B) Gene scores in untreated versus DFO-treated (2$\mu$M) Jurkat cells, modified from Figure 2.9B. The gene score is the median log2 fold change in the abundance of all sgRNAs targeting that gene during the culture period. Most genes, as well as non-targeting control sgRNAs, have similar scores in the presence or absence of the treatments.

(C) Gene scores in untreated versus high DFO-treated (5$\mu$M) Jurkat cells. The gene score is the median log2 fold change in the abundance of all sgRNAs targeting that gene during the culture period. Most genes, as well as non-targeting control sgRNAs, have similar scores in the presence or absence of the treatments.

(D) Immunoblotting for ATP2C1 to confirm *ATP2C1* 293T knockout cells. GAPDH is used as a loading control.

(E) Fold change in cell number (log2) of parental and ATP2C1 null 293T cells in the absence or presence of indicated concentrations of DFO for 5 days (mean ± SD, n=3, **p<0.05).

(F) Fold change in cell number (log2) of parental and ATP2C1 null 293T cells in the absence or presence of indicated concentrations of $MnCl_2$ for 5 days (mean ± SD, n=3, **p<0.05).

(G) Fold change in cell number (log2) of parental and ATP2C1 null 293T cells in the absence or presence of indicated concentrations of FAC for 5 days (mean ± SD, n=3, **p<0.05).

Because we were most interested in organellar functions, we looked back at our negative DFO screens for organellar candidates. Among the top five sensitizers to DFO were mitochondrial iron importers (Shaw et al., 2006), SLC25A37/Mitoferrin-1 and SLC25A28/Mitoferrin-2. Due to redundancy, each of these genes is not essential when iron is sufficient. We reasoned, however, that when iron is limiting the transport efficiency of iron into mitochondria becomes vital. Thus, both paralogs are required.

In addition to these mitochondrial transporters, *ATP2C1,* the golgi manganese/calcium importer also scored. Confirming the screen results, loss of *ATP2C1*, sensitized cells to iron chelation (Figure 3.1D,F). Despite occupying only ~5% of total cell volume, 60% of cellular manganese localizes to Golgi, making this organelle the major storage site for $Mn^{2+}$ (Carmona et al., 2010; Das et al., 2019). Thus, consistent with previous reports (Xia et al., 2017), *ATP2C1*$^{-/-}$ cells were sensitive to manganese ($Mn^{2+}$) supplementation due to cellular $Mn^{2+}$ overload (Figure 3.1F). As manganese and iron are chemically similar and compete for enzymes and transporters, we wondered whether ATP2C1 affects iron cytotoxicity. Remarkably, loss of *ATP2C1* fully rescued iron toxicity (Figure 3.1G). Taken together, these results indicate that the essential function of Golgi during iron chelation is to buffer cellular manganese. This function also contributes to iron's cytotoxicity.

**Manganese overload partly phenocopies iron chelation**

To validate our *ATP2C1* findings, and rule out generalized Golgi stress, we next explored the effects of iron chelation, iron overload, and manganese supplementation.

**Figure 3.2: Manganese partly phenocopies iron chelation**

(A) Fold change in cell number (log2) of 293T cells grown in the absence or presence of indicated concentrations of $MnCl_2$ and in the presence or absence of DFO (2.5$\mu$M) for 5 days (mean ± SD, n=3, **p<0.05).

(B) Fold change in cell number (log2) of 293T cells grown in the absence or presence of indicated concentrations of $MnCl_2$ and in the presence or absence of a lethal dose ofFAC (1mg/ml) for 5 days (mean ± SD, n=3, **p<0.05).

(C) Fold change in cell number (log2) of 293T cells grown in the absence or presence of indicated concentrations of $ZnCl_2$ and in the presence or absence of FAC (0.125mg/ml) for 5 days (mean ± SD, n=3, **p<0.05).

(D) Fold change in cell number (log2) of 293T cells grown in the absence or presence of indicated concentrations of $CuCl_2$ and in the presence or absence of FAC (0.125mg/ml) for 5 days (mean ± SD, n=3, **p<0.05).

(E) Immunoblotting for TFRC and FDX1in 293T cells grown for 24 hours in the absence or presence of $MnCl_2$ (20$\mu$M), DFO (100$\mu$M), FAC (0.1mg/ml). GAPDH is used as a loading control

(F) Immunoblotting for HIF1A and HMOX1 in 293T cells grown for 24 hours in the absence or presence of $MnCl_2$ (20$\mu$M), DFO (100$\mu$M), FAC (0.1mg/ml). GAPDH is used as a loading control

(G) Fold change in cell number (log2) 293T cells grown at 0.5% or 21% $O_2$ with 5 increasing concentrations of DFO (0, 10, 20, 50, 100 $\mu$M), FAC (0, 0.125, 0.25, 0.5, and 1mg/ml), and $MnCl_2$ (0, 5, 10, 20, 50) the absence or presence of indicated concentrations of $MnCl_2$ for 5 days (mean ± SD, n=3, **p<0.05).

(H) Fold change in cell number (log2) 293T cells grown at with 5 increasing concentrations of FAC (0, 0.125, 0.25, 0.5, and 1mg/ml), and $MnCl_2$ (0, 5, 10, 15, 20 $\mu$M) in the absence or presence of the antioxidant Ferrostatin-1 (2 $\mu$M) (mean ± SD, n=3, **p<0.05).

(I) Schematic to describe the mode of action of RSL3 and erastin.

(J) Fold change in cell number (log2) 293T cells grown in the presence or absence of a lethal dose of RSL3 (0.8 $\mu$M) 5 increasing concentrations of $MnCl_2$ for 5 days (mean ± SD, n=3, **p<0.05).

(K) Fold change in cell number (log2) 293T cells grown in the presence or absence of a sub-lethal dose of erastin (0.5 $\mu$M) with 5 increasing concentrations of $MnCl_2$ for 5 days (mean ± SD, n=3, **p<0.05).

(L) Fold change in cell number (log2) 293T cells grown in the presence or absence of a lethal dose of erastin (3 $\mu$M) and indicated sub-lethal concentrations of $MnCl_2$ for 5 days (mean ± SD, n=3, **p<0.05).

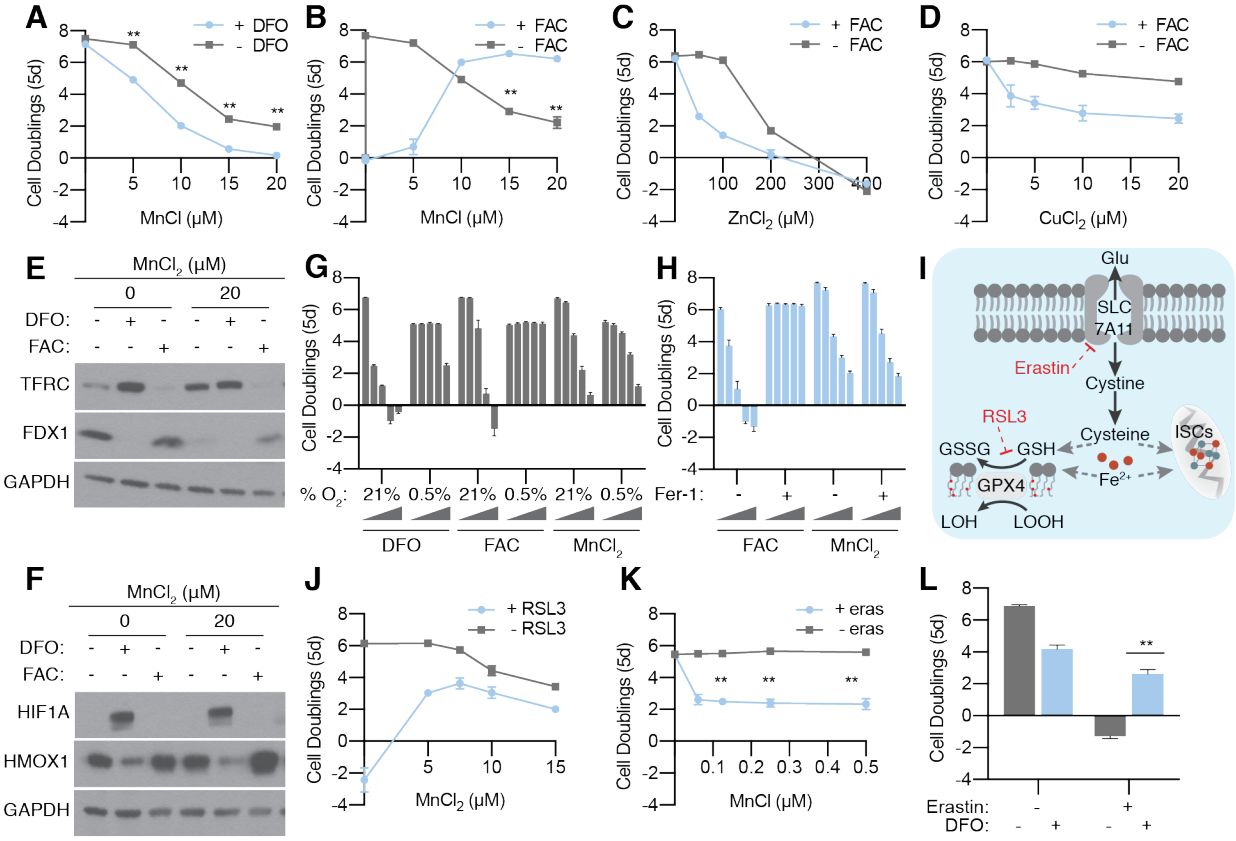
A
+ DFO
- DFO
Cell Doublings (5d)
MnCl (μM)
B
+ FAC
- FAC
Cell Doublings (5d)
MnCl (μM)
C
+ FAC
- FAC
Cell Doublings (5d)
ZnCl2 (μM)
D
+ FAC
- FAC
Cell Doublings (5d)
CuCl2 (μM)
E
MnCl2 (μM)
0
20
DFO:
FAC:
TFRC
FDX1
GAPDH
G
Cell Doublings (5d)
% O2:
21% 0.5% 21% 0.5% 21% 0.5%
DFO
FAC
MnCl2
H
Cell Doublings (5d)
Fer-1:
FAC
MnCl2
I
Glu
SLC 7A11
Erastin
Cystine
RSL3
Cysteine
ISCs
GSSG
GSH
GPX4
Fe2+
LOH
LOOH
F
MnCl2 (μM)
0
20
DFO:
FAC:
HIF1A
HMOX1
GAPDH
J
+ RSL3
- RSL3
Cell Doublings (5d)
MnCl2 (μM)
K
+ eras
- eras
Cell Doublings (5d)
MnCl (μM)
L
Cell Doublings (5d)
Erastin:
DFO:

Consistent with impaired manganese storage potentiating iron chelation toxicity, DFO and $Mn^{2+}$ treatments were synthetically lethal (Figure 3.2A). Just as *ATP2C1* loss provided iron resistance, manganese and iron were reciprocally toxic. Supplementation of one metal reversed the cytotoxicity of the other (Figure 3.2B). To confirm that this phenomenon was specific to manganese, we also checked the effect on iron toxicity of zinc and copper, two other important intracellular transition metals. In contrast to manganese, these metals had a synergistically toxic effect with iron (Figure 3.2C,D). Copper, which is redox active and can catalyze a Fenton-like reaction (Lee et al., 2016), likely increased ROS production and potentiated iron-mediated ferroptosis. Zinc, which is not known to be redox active, however can compete with iron for ferritin. This may interfere with iron storage, which is essential under iron overload (Price and Joshi, 1982). Solidifying this proposed mechanism will require further follow up work.

To understand why manganese is toxic, we compared it to iron chelation in several ways. Similar to iron chelation, manganese, activated the IRP pathway as indicated by an increase in TFRC protein levels. Like DFO, manganese also destabilized ISC protein FDX1 (Figure 3.2E). These data implied that $Mn^{2+}$ provoked a state of relative iron starvation. Unlike iron chelation, however, $Mn^{2+}$ had little effect on HMOX1 protein levels and did not observably activate HIF1a (Figure 3.2 F). Furthermore, while hypoxia reversed iron chelation cytoxicity, likely due to ISC buffering, it did not change $MnCl_2$ (Figure 3.2G). Consistent with ineffective hypoxia rescue, antioxidant supplementation had little effect (Figure 3.2H).

Given that Mn phenocopies the protective effect of DFO to counter iron toxicity, we asked whether the same would be true regarding other means of inducing ferroptosis. GPX4 uses GSH to reduce lipid peroxides to lipid alcohols and prevents ferroptosis (Figure 3.2I). As expected, $Mn^{2+}$ reversed direct inhibition of GPX4 (Figure 3.2J). Iron chelation similarly rescued toxicity of erastin, a small molecule inhibitor of cystine uptake, the limiting component of GSH synthesis and the sulfur source for ISC synthesis (Figure 3.2I,L). Manganese supplementation, in contrast, unexpectedly potentiated inhibition of cystine uptake (Figure 3.2K). Taken together, manganese supplementation and iron chelation have similar but not identical effects. Teasing apart these differences will reveal new biology and elucidate the mechanisms of manganese toxicity.

**Mitochondrial proteomics uncovers a post-translationally regulated mitochondrial transporter**

Taking an orthogonal approach to uncover specific organellar adaptations, we performed proteomics on mitochondria isolated from cells grown under control, iron overloaded, or iron starved conditions. Similar to our genetic screens, in all conditions we treated cells with the antioxidant, Fer-1, to uncouple reactive oxygen species (ROS) from iron homeostasis.

Akin to our lysosomal purifications, we took advantage of the mitoIP system (Chen et al., 2016). Here, we lysed cells expressing an HA-epitope tagged Outer Mitochondrial Protein 25 (OMP25) over anti-HA magnetic beds for rapid organellar

purification (Figure 4.3A). Enrichment of Citrate Synthase (CS), a mitochondrial matrix-localized TCA enzyme and depletion of GAPDH, a cytosolic glycolysis enzyme indicated that our preparations were pure. Stabilized IRP2 and destabilized mitochondrial ISC proteins FDX1 and SDHB implied that our treatment conditions were effective (Figure 4.3B).

Applying a Tandem Mass Tag (TMT)-isobaric labeling based mass spectrometry proteomics analysis to our purified mitochondria, we identified peptides mapping to 1765 unique proteins. It was initially concerning that only 524 of these 1765 proteins were found in MitoCarta 2.0 or IMPI, two databases of mitochondrial proteins (Figure 4.3C). Because 77% of the total signal intensity matched these databases, however, suggested proper mitochondrial enrichment (Figure 4.3D). We attributed the other identified proteins to mitochondrial-organellar contacts, novel mitochondrial proteins, non-specific binding to magnetic beads, or cytoplasmic contamination.

After quantifying peptide abundances and setting a threshold of $p<0.01$ and a fold change $> 2$, we observed a few significant changes due to FAC and broader significant changes due to DFO. In response to iron overload, only TFRC decreased. This was consistent with decreased IRP binding to the 3' UTR of *TFRC* resulting in mRNA destabilization (Figure 3.3E). While TFRC is not a typical mitochondrial protein, TFRC binds ferromagnetic iron and thus, may non-specifically bind magnetic beads. Anecdotally, we have observed TFRC binding to anti-HA beads lysed from cells expressing myc-tagged mitochondria. Alternatively, these data may reflect the fact

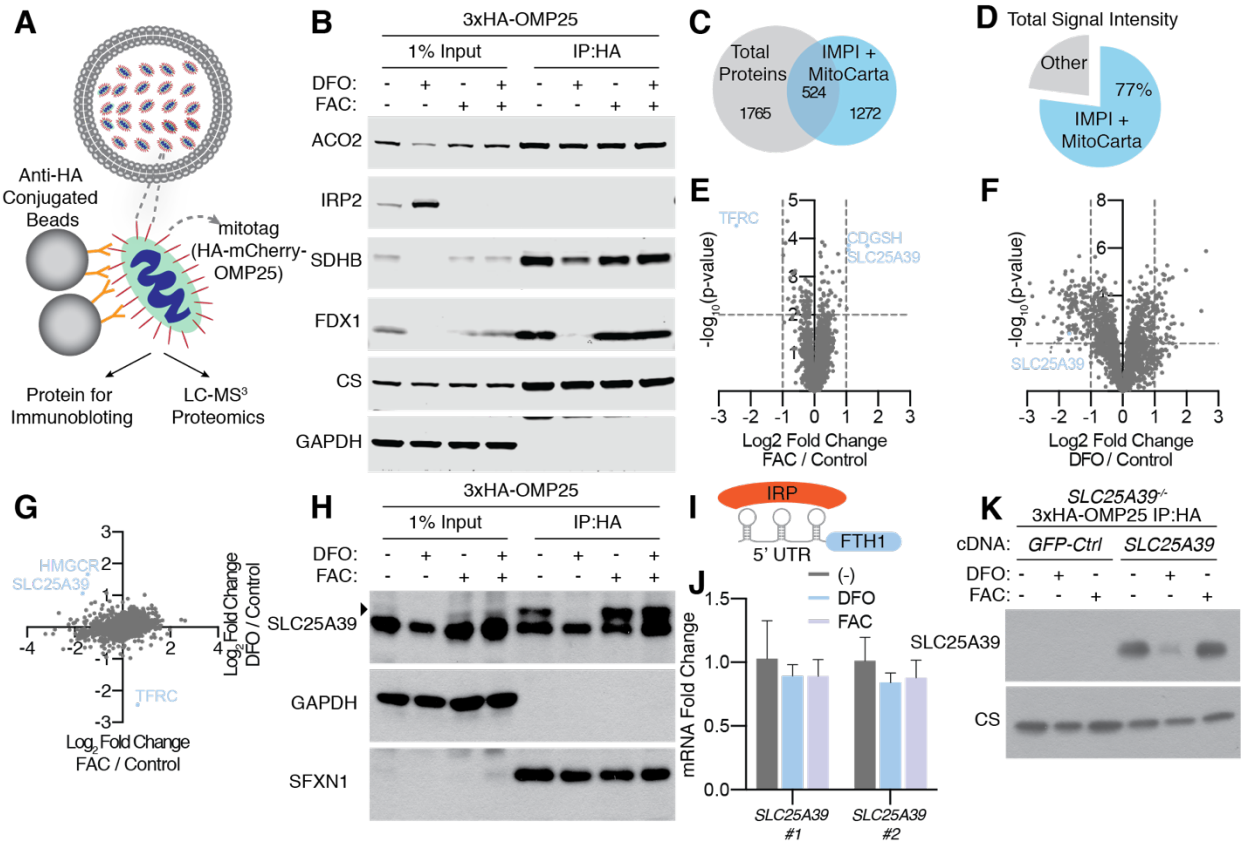


**Figure 3.3: Mitochondrial proteomics uncovers a post-translationally regulated mitochondrial transporter**

(A) Schematic for mitochondria purification protocol.

(B) Immunoblots for ACO2, IRP2, SDHB, FDX1 on input protein lysates and HA-immunoprecipitants purified from 293T cells grown in the presence of Fer-1 (1 $\mu$M) and the presence or absence of DFO (100$\mu$M) and or FAC (0.1mg/ml). CS is used as a mitochondrial loading control. GAPDH is used as a cytosolic loading control.

(C) Schematic representing overlap of identified proteins (1765) with those found in mitochondrial databases IMPI and MitoCarta.

(D) Schematic representing percent of total intensity of peptides matching to proteins found in mitochondrial databases IMPI and MitoCarta

(E) Volcano plot of -log10 pvalue and log2 fold changes in response to FAC compared to control. Cut-off indicated by dotted line at p<0.01 and absolute fold change >2.

(F) Volcano plot of -log10 pvalue and log2 fold changes in response to FAC compared to control. Cut-off indicated by dotted line at p<0.01 and absolute fold change >2/

(G) Scatter plot of normalized log2 fold change of DFO vs. FAC. Noted in light blue are genes that are significantly reciprocally regulated in response to iron.

(H) Immunoblots for SLC25A39 on input protein lysates and HA-immunoprecipitants purified from 293T cells grown in the presence of Fer-1 (1 $\mu$M) and the presence or absence of DFO (100$\mu$M) and or FAC (0.1mg/ml). SFXN1 is used as a mitochondrial loading control. GAPDH is used as a cytosolic loading control.

(I) Illustration of IRP-mediateed regulation of a 5' IRE.

(J) qRT-PCR analysis for SLC25A39 mRNA using two different primer sets. RNA extracted from HeLa cells grown for 24 ±DFO (100 $\mu$M), ±FAC (0.1mg/ml) (mean ± SD, n=3, n.s.).

(K) Immunoblots for SLC25A39 on HA-immunoprecipitants purified from HeLa cells grown in the presence or absence of DFO (100$\mu$M) or FAC (0.1mg/ml). CS is used as a mitochondrial loading control.

TFRC can make contact with mitochondria as an alternative means of iron delivery (Furihata et al., 2018).

Conversely, upon FAC treatment, there were two significantly enriched mitochondrial proteins, CDGSH or mitoNEET and SLC25A39. As a small outer mitochondrial membrane bound protein containing a 2Fe-2S ISC, CDGSH repairs iron sulfur clusters and plays a role in mitochondrial redox homeostasis (Wiley et al., 2007). These experiments recapitulated previous findings that high levels of iron post-translationally stabilized mitoNEET (Kusminski et al., 2012). SLC25A39 is a member of the SLC25A family of inner mitochondrial membrane solute transporters. Because cold exposure induced SLC25A39 expression in brown adipose tissue, SLC25A39 was first posited to be an uncoupling protein (Yu et al., 2001). Later, it was associated with hematopoiesis as loss SLC25A39 impaired heme synthesis in mouse erythrocyte precursor cells and caused anemia in zebrafish (Nilsson et al., 2009). Disruption of its drosophila ortholog caused neurodegeneration, increased ROS, electron dense mitochondria—indicative of free iron accumulation, and accumulation of cytosolic manganese (Slabbaert et al., 2016).

When we examined the proteomic response to iron chelation, there were many changes that fell into a several broad categories (Figure 3.3F). Unexpectedly, we observed a decrease STARD7 and PRELID1, two canonical targets of the mitochondrial inner membrane i-AAA zinc protease, YME1L (MacVicar et al., 2019). This implied that metal imbalance, perhaps the mitochondrial zinc to iron ratio regulates its activity. We saw an expected drop in iron sulfur cluster proteins including FDX1, NDUFS6, LIAS and ETFDH. As previously noted, iron starvation increased hypoxia signaling (Figure 3.2F).

Consequently, canonical HIF1a targets, including PDK1 and HK2 were all upregulated. We also observed BACH1/NRF2 gene regulation, which is responsive to heme levels. As previously observed, iron chelation decreased HMOX1, a BACH1/NRF2 transcriptional target (Figure 3.2F).

To narrow down proteins that respond in a dose dependent manner to iron and meet our exclusion criteria, we plotted DFO vs. FAC enrichment values. These proteins included cholesterol synthesis and SREBP target HMGCR, IRP target TFRC, and SLC25A39 (Figure 4.3G). Among these only SLC25A39 was annotated as mitochondrial. Furthermore, SLC25A39's function and mode of regulation were unknown. These data, in addition to the aforementioned studies, strongly suggested iron-mediated regulation of SLC25A39.

Validating our proteomics findings, we observed a dramatic decrease and a subtler increase in SLC25A39 protein levels upon iron chelation and supplementation, respectively (Figure 3.3H). Next, we asked how iron regulates SLC25A39. One possibility is that the mRNAs encoding SLC25A39 contains a 5' IRE in its UTR, like FTH1 or ALAS2 (Figure 3.3I). This would explain how its protein levels were proportional to cellular iron levels. Another possibility is that it is a transcriptional target of NRF2 or BACH1. These possibilities were unlikely as *SLC25A39* neither contains an apparent IRE in its 5' UTR nor is it a canonical NRF2/BACH1 target. In any case, to rule these out, we measured *SLC25A39* mRNA levels in response to our treatments and observed no significant changes (Figure 3.3J). To further exclude mRNA stability or translational repression, we compared the effects of our treatments in *SLC25A39* clonal knockout cells expressing a guide resistant cDNA without its 5' or 3' UTRs. Arguing

strongly for destabilization at the protein level, DFO treatments similarly destabilized the expressed SLC25A39 cDNA (Figure 3.3K).

**SLC25A39 links mitochondrial GSH and ISCs**

Because SLC25A39 is a member of the mitochondrial solute transporter family, we hypothesized that has a role in mitochondrial metabolome mainteance. To test this, we performed LC-MS based metabolomic profiling on whole cell extracts and purified mitochondria from *SLC25A39*$^{-/-}$ cells expressing a control vector or a guide resistant cDNA. While there were no significant differences in whole cell metabolites, remarkably, there was a nearly eight-fold depletion of reduced (GSH) and oxidized glutathione (GSSG) in *SLC25A39*$^{-/-}$ mitochondria (Figure 3.4A).

It remains to be determined whether SLC25A39 itself directly imports GSH. It is also possible that it enables another GSH transport protein or supports a matrix environment in which GSH is not consumed by heavy metals or other toxins. A GSH transport assay on SLC25A39 proteo-liposomes would confirm mitochondrial GSH uptake sufficiency.

Following up on this result, we tested whether modulation of cellular GSH levels might also affect the stability of SLC25A39. L-Buthionine-sulfoximine (BSO), an inhibitor of GSH synthesis protein, Glutamate-Cysteine Ligase Catalytic Subunit (GCLC) decreased cellular and mitochondrial GSH levels (Figure 3.4B). BSO treatment moderately stabilized SLC25A39 (Figure 3.4C). In an effort to further drop GSH levels, we combined BSO with erastin, an inhibitor of cellular cystine uptake, the limiting amino acid precursor of GSH (Figure 3.2I). Simultaneous inhibition of enzyme and substrate

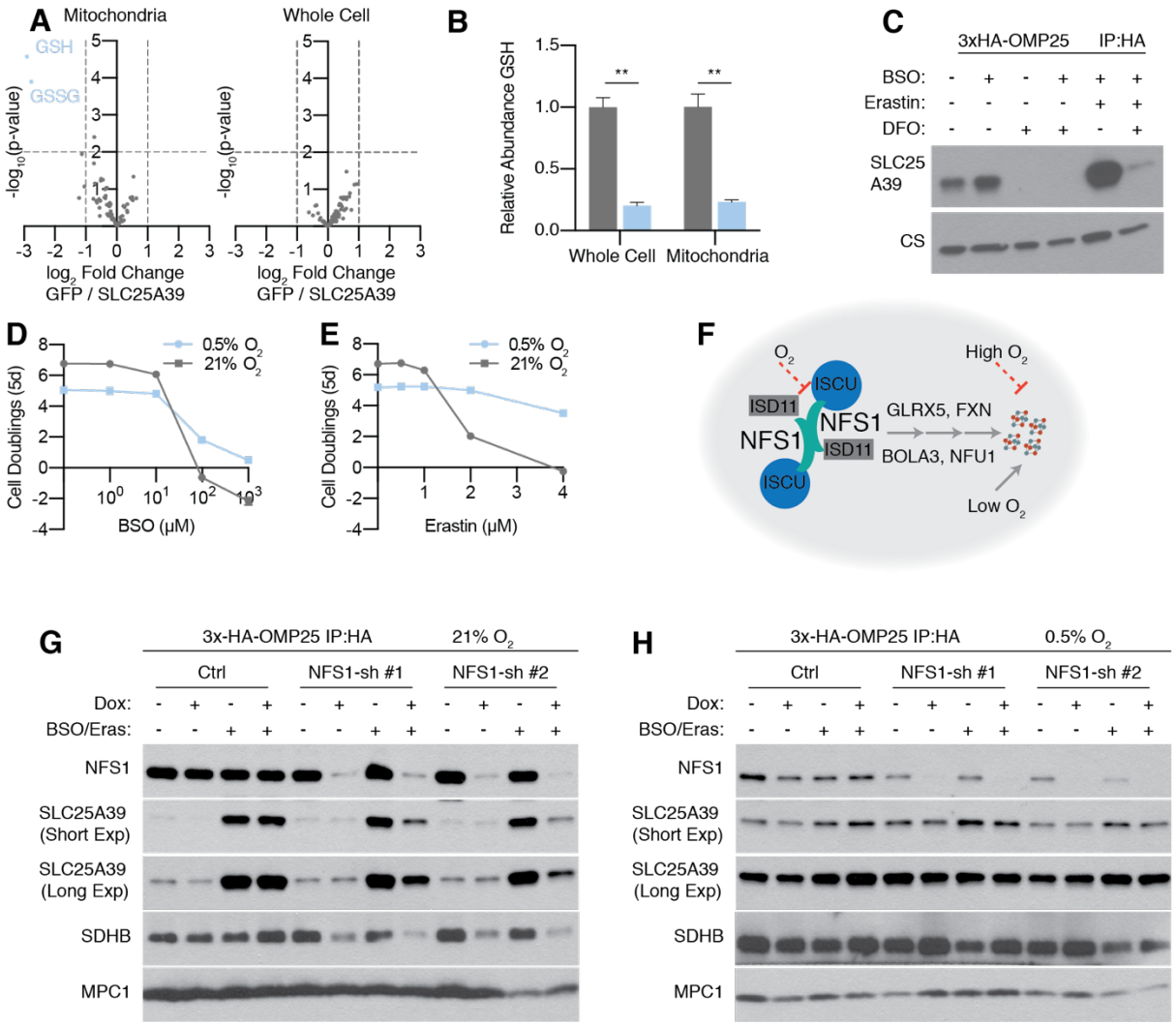


**Figure 3.4 SLC25A39 links mitochondrial GSH and ISCs**

(A) Volcano plots comparing mitoIP-purified mitochondrial and whole cell polar metabolites in SLC25A39$^{-/-}$ HeLa cells expressing a control (GFP) or a sgRNA resistant cDNA (SLC25A39). Cutoffs, indicated by dotted lines, were set to p<0.01 and absolute fold change>2.

(B) Measurement of GSH in mitoIP-purified mitochondria and whole cells following 24h treatment in 1mM BSO. (mean ± SD, n=3, **p<0.05)

(C) Immunoblots of SLC25A39 and CS on mitoIP-purified mitochondrial from HeLa cells grown in the absence or presence of the following treatments: DFO (100 $\mu$M), BSO (1mM), or Erastin (5 $\mu$M)..

(D) Fold change in cell number (log2) 293T cells grown in the presence or absence of indicated doses of BSO at 0.5% $O_2$ and 21% $O_2$ for 5 days (mean ± SD, n=3, **p<0.05).

(E) Fold change in cell number (log2) 293T cells grown in the presence or absence of indicated doses of erastin at 0.5% $O_2$ and 21% $O_2$ for 5 days (mean ± SD, n=3, **p<0.05).

(F) Illustration of the effect of oxygen on ISC synthesis and stability.

(G) Immunoblots of NFS, SLC25A39, and SDHB on purified mitochondrial from HeLa cells expressing a doxycycline inducible shRNA targeting *NFS1*. Cells were grown at 0.5% $O_2$ in the absence or presence of doxycycline (100ng/ml) for 96h. For the last 24h, BSO(1mM) / Erastin (5 $\mu$M) was added. MPC1 is used as a mitochondrial loading control.

(H) Immunoblots of NFS, SLC25A39, and SDHB on purified mitochondrial from HeLa cells expressing a doxycycline inducible shRNA targeting *NFS1*. Cells were grown at 21% $O_2$ in the absence or presence of doxycycline (100ng/ml) for 96h. For the last 24h, BSO (1mM) / Erastin (5 $\mu$M) was added. MPC1 is used as a mitochondrial loading control.

had a robust synergistic effect (Figure 3.4C). Iron chelation, which destabilized SLC25A39 at baseline, similarly, reversed low GSH-mediated stabilization (Figure 3.4C). This suggested that low GSH-mediated stabilization was also dependent on cellular iron levels.

To distinguish whether free iron or assimilated iron determined stabilization, we examined the effect of shRNA knockdown of *NFS1* on SLC25A39 levels. NFS1, the mitochondrial cysteine desulfurase, is the rate limiting enzyme for iron sulfur cluster synthesis (Lill and Freibert, 2020). As such, it is one of the most essential genes in the human genome. In fact, sgRNAs targeting *NFS1* routinely rank among the most depleted in t our genetic screen control conditions (Figure 3.1A,C). Hypoxia rescues the proliferation defects of NFS1 knockdown (*NFS1-KD*) cells because it prevents oxidative damage to iron sulfur clusters (Alvarez et al., 2017) and because it increases ISC synthesis (Ast et al., 2019) (Figure 3.4F). To test whether SLC25A39 stability was dependent on iron sulfur clusters, we generated doxycycline-inducible NFS1 conditional knockdown cells at 21% oxygen ($O_2$) and 0.5% $O_2$ and measured the effect of low GSH on SLC25A39 stability. We reasoned that Loss of ISC synthesis enzymes increases free mitochondrial iron (Chen et al., 2002). Thus, if free iron stabilizes SLC25A39, we would expect an increase in protein levels. On the other hand, if ISCs stabilize SLC25A39, we would expect a decrease.

*NFS1-KD* destabilized the iron sulfur cluster protein, SDHB at 21% but not at 0.5 % $O_2$ (Figure 3.4 G,H). This assured us that *NFS1-KD* had a measurable effect on ISC synthesis, which, as previously reported (Alvarez et al., 2017) was reversed by low oxygen. With regards to SLC25A39, this experiment was informative on several levels.

First, 0.5% $O_2$ blunted stabilization of SLC25A39 due to GSH loss (Figure 3.4G). Whereas hypoxia rescued BSO-mediated ROS generation and its subsequent cytotoxicity (Figure 3.4 D,E), it does not reverse BSO-mediated loss of cellular GSH (Yang et al., 2003). This suggested, that, here too, GSH depletion itself did not directly stabilize SLC25A39 but rather the ensuing oxidative damage did. Second, *NFS1-KD*, dampened low-GSH mediated stabilization at normoxic conditions (Figure 3.4F). This argued that the stabilization resulting from GSH-depletion mediated oxidative damage depended on an ample supply of ISCs. Taken together these data indicated that damaged or liberated ISCs stabilized SLC25A39. Thus, when ISC synthesis is inhibited or oxidative damage is reduced, there are no longer sufficient levels of these ISCs to stabilize SLC25A39. To cement this hypothesis and prove direct ISC binding, Mossbauer spectroscopy on purified SLC25A39 will be required. Finally, because *NFS1-KD* decreased SLC25A39 levels, it also ruled out that free iron stabilized SLC25A39.

Still, if damaged ISCs stabilize SLC25A39, we need to reconcile why *NFS1-KD* did not destabilize SLC25A39 at baseline whereas iron chelation did. While *NFS1-KD* impaired ISC synthesis to some extent, as an shRNA knockdown with some lingering protein present, residual ISC synthesis likely remains. Complete iron chelation, on the other hand, may prevent ISC synthesis to a much greater extent. Another possibility is that free iron or heme levels regulate SLC25A39's baseline stability. It will be difficult to resolve this discrepancy, as NFS1 knockouts, are not viable even at hypoxia. One approach would be combined moderate iron chelation, at a level that does not affect

SLC25A39 stability, with NFS1-KD. This setting might drive ISC levels low enough levels to destabilize SLC25A39.

## DISCUSSION

In the first part of this chapter we sought to catalogue essential organellar specific functions in the context of altered cellular iron. We found that organellar metal transport is a major determinant of cell proliferation under limited iron. For mitochondria, the paralogous iron transporters, Mitoferrin-1 and Mitoferrin-2, can normally substitute for one another. When iron is limiting, however, cells require the activity of both. Unless otherwise challenged, Golgi transition metal storage is expendable in proliferating cells. Under low iron, however, manganese uptake is an essential role for this organelle because manganese overload mimics relative iron depletion.

While the first part of this chapter highlighted the importance of an organellar specific function for the broader cellular milieu, the second part uncovered a potential organellar self-repairing circuit. Certainly, rigorous follow-up work is necessary to establish direct or indirect ISC binding and GSH transport. Still, we propose that SLC25A39 is stabilized by damaged or liberated ISCs and, at the same time, supports mitochondrial GSH import to repair these clusters and prevent further oxidative damage. Given that ISCs are rapidly oxidized but difficult to synthesize and repair, a reflexive post-translational mechanism in this setting makes sense.

Interestingly, this mode of regulation is also similar to other organellar transporters. On lysosomes, SLC38A9 senses lumenal arginine, which enables its efflux activity of the essential amino acid leucine. This, in turn, activates mTOR and cell

growth (Wyant et al., 2017). So too SLC25A39 may sense the oxidative or metal state of mitochondria and react to modulate GSH import. Using one metabolite to tune the levels of another—albeit related—metabolite, may be a more efficient alternative to transcriptional signaling to buffer small organellar changes.

This regulation may also relate to findings in the first half of this chapter. In our iron chelation screen, we found that impairment of GSH synthesis was actually beneficial when iron is very low (Figure 3.2C). One interpretation, as is observed in yeast, is that GSH chelates iron and removes it from the usable pool (Kumar et al., 2011). We speculate, that the absence of damaged or liberated ISCs may also indicate a relative shortage of mitochondrial iron. Backhandedly, mitochondria counter this by decreasing GSH import in an effort to boost free mitochondrial iron.

## Chapter 4: Future Directions and Perspectives

### Non-Transferrin bound iron uptake

In chapter 2, we found that iron supplementation circumvents lysosomal-dependent transferrin iron uptake. Confirming these results, in chapter 3, we established that iron supplementation rendered the transferrin receptor dispensable. Nonetheless several important questions remain with regard to non-transferrin bound iron (NTBI) uptake.

The relevant set of free iron transporters requires identification. Potential candidates located on the plasma membrane with known metal transport activity include DMT1 (SLC11A), ZNT (SLC30A), or ZIP (SLC39A) proteins (Ji and Kosman, 2015). Coupling NTBI obligate systems, such *TFRC* knockout or lysosomal pH inhibited cells, to CRISPR/Cas9 screening strategies would uncover differentially essential genes for their proliferation, among them, the free iron carrier. A major complicating factor, however, is redundancy and cell type specificity. In addition to other solute transporters with purported iron or metal transport function, there are 14 members of the ZIP family with different expression profiles across tissues types (Bafaro et al., 2017).

The ramifications of bypassing this system also warrant further consideration. As our iron screen indicated, the ferritin storage system counters iron overload toxicity (Figure 3.1A). We also found that zinc supplementation potentiated iron cytotoxicity (Figure 3.2C) likely through iron-zinc competition for ferritin sites (Price and Joshi, 1982). It will be informative to test the importance of zinc transport and storage upon iron supplementation. Indeed, if zinc regulation is a key factor, we can also leverage the NTBI system to clarify mechanisms of intracellular zinc homeostasis. Furthermore,

because many free metal transporters, including ZIP and DMT proteins, are quite promiscuous, they can import a variety of divalent substrates including iron, zinc, nickel, cadmium and manganese (Dempski, 2012). If iron predominantly uses this cellular entry pathway it may also affect homeostasis of other metals.

Although iron supplementation rescued loss of ISC proteins, respiration defects and hypoxia signaling, we also need to explore the possibility that transferrin bound iron may be qualitatively different from NTBI. Perhaps in the setting of direct iron uptake cells are now more dependent on intracellular cysteine, glutathione or other metabolite or protein chelators. Consistent with this, SLC7A11, the cellular importer of cystine, the limiting precursor for GSH, was a weak hit in our iron overload screen (Figure 3.1A).

Tackling these questions will be relevant for several clinical contexts. Iron-overload, in the setting of genetic hemochromatosis or beta thalassemia, end stage renal failure, diabetes, or cancer chemotherapy, is associated with NTBI-mediated cardiac and kidney damage (Patel and Ramavataram, 2012). While chelation can prevent some damage, it comes with its own set of drawbacks including side effects, dosing difficulties, and bioavailability (Shah, 2017). Understanding the mechanism and ramifications of NTBI uptake will uncover complementary therapeutic approaches to chelation.

Unlike most tissues, NTBI is an important source of brain iron. NTBI is usually undetectable in serum but readily detectable in cerebral spinal and brain interstitial fluids (Knutson, 2019). Because glial cells express low to undetectable levels of TFRC, NTBI may be especially important for these cells (Codazzi et al., 2015). But exactly why

these cells at least, in part, askew the TFRC system remains unanswered. Reasonable advantages of NTBI might include baseline ROS maintenance, required for synaptic transmission and long-term potentiation, and more efficient iron utilization to meet a neuron's metabolic demands. In any case, a concrete understanding of NTBI will inform glial cell biology and neurodegenerative disease pathogenesis

**Conservation of the lysosome-iron axis and signaling**

In chapter 2, we determined that an essential function of lysosomes is to provide iron. Strikingly, complementary studies on the yeast vacuole, the fungal counterpart to the animal lysosome, suggest that the link between lysosomal acidity and iron homeostasis is conserved across eukaryotic evolution. Genetic or pharmacologic ablation of yeast vacuolar acidification similarly triggered an iron starvation signaling response and destabilized iron sulfur cluster containing proteins. Furthermore, iron supplementation or overexpression of cellular iron importers also rescued yeast cell proliferation in non-fermentable media under vacuolar pH dysfunction (Chen et al., 2020; Davis-Kaplan et al., 2004; Diab and Kane, 2013; Hughes et al., 2020).

Although the link between lysosomal or vacuolar acidity and iron homeostasis is shared, the underlying rational differs. In mammals, increased lysosomal pH impairs the dissociation of ferric iron from the endocytosed transferrin-transferrin receptor complex (Dautry-Varsat et al., 1983). Likewise, the release of ferric iron from ferritin, the endogenous cytosolic iron storage protein complex, requires functional lysosomes to digest ferritin through autophagy (Mancias et al., 2014). Taken together, lysosomal pH

affects iron abundance and downstream iron sulfur cluster synthesis in mammalian cells because the acidic environment is required to free protein-sequestered iron in mammalian cells.

In contrast, in yeast, there is no intuitive explanation for how or why an iron starvation signal is induced under vacuolar pH inhibition. Although the vacuole is the major site of iron storage for fungi and plants (Raguzzi et al., 1988), when its acidity is dissipated, total cellular iron levels do not change (Chen et al., 2020). In fact, acute inhibition of the vATPase elicits an iron starvation response within minutes, likely not reflective of the iron state of a cell (Diab and Kane, 2013). Furthermore, vacuolar uptake of iron requires neither an intact endocytosis pathway (Li et al., 2001) nor vacuolar acidity (Bode et al., 1995). Iron starvation almost appears to be hardwired into vacuolar dysfunction.

Recent work, however, has pointed to amino acid dysregulation leading to excess intracellular cysteine upon vacuolar pH disruption as the effector molecule (Hughes et al., 2020). It remains to be determined exactly how cysteine acts as a signal amplifier for iron starvation. One possibility, previously raised in chapters 1 and 3, is that cysteine and especially its downstream metabolite, GSH, can chelate and form complexes with ferrous iron at neutral physiologic pHs (Hider and Kong, 2011). In fact, overexpression of the yeast GSH importer induces an iron signaling response analogous to chelation (Kumar et al., 2011). Furthermore, as previously noted, (Figure 3.1B,C), loss of glutathione synthesis geene, *GCLM*, conferred a growth advantage under iron chelation. In yeast, vacuolar dysfunction induces a thiol burst which, in turn,

may sequester iron away and elicits a starvation response. Inhibiting GSH synthesis in the context of vATPase inhibition or iron chelation might uncouple whether the root cause is thiol mediated iron sequestration.

Cysteine, however, is likely not relevant to mammalian systems. In fact, our unbiased genetic screens identified extracellular cystine uptake as necessary under ammonia treatments (Figure 2.1G). In the setting of limited iron, adequate cysteine levels are expected to be important to maintain ISC synthesis.

In any case, these yeast data point to a vacuolar dysfunction mediated iron starvation response, independent of cellular iron status. Our data also suggest an organellar autonomous means of turning on iron signaling through increased lysosomal pH. While iron fully reversed Bafilomycin A1-mediated changes in iron sulfur clusters and HIF1a signaling, it only partially reversed IRP2 stabilization. In contrast, iron supplementation completely reversed the DFO activated IRP pathway. This discrepancy hints at the possibility that lysosomal dysfunction may be sufficient to elicit a partial IRP response uncoupled from the overall iron status of the cell. Lysosomal metabolite or signaling changes upon vATPase inhibition may trigger this signal. Alternatively, accumulation of holo-transferrin or holo-ferritin may initiate an IRP signal.

It remains to be determined whether such a pathway exists and how it signals. A FACS-based genetic screening strategy to identify factors which stabilize TFRC and IRP2 in the setting of supplemented iron and lysosomal dysfunction would uncouple lysosomal dysfunction from the IRP response. A different tactic would be to compare the lysosomal proteomes upon BafA1 treatment in the presence or absence of iron.

Common factors that respond to compromised lysosomal pH, uncoupled from cellular iron, would be especially promising.

**New players in iron homeostasis**

Throughout this work, we utilized several paradigms to study iron metabolism. These assumptions, however, warrant a second look. ISCs, themselves, are unstable and prone to oxidation, and are, thus, difficult to measure. Therefore, we used ISC protein stability to approximate ISC abundance. Indeed, low cellular iron and inhibition of ISC synthesis decreased many but not all ISC proteins. Puzzlingly, exactly how this occurs is not well defined. One hypothesis is that the protein becomes inherently unstable resulting in proteolysis. If so, cluster loss should uncover destabilization domains or severely unfold the protein. Comparing the architectures of destabilized ISC proteins with ACO1, a protein that loses its cluster but is not destabilized, may be informative. Alternatively, a chaperone or adapter may sense an apo-ISC binding protein and target it for degradation. There may be different chaperones for different compartments or types of ISC proteins. If the later were true, we can perform another FACS based screen using fluorescent-tagged organellar ISC proteins from different organelles (e.g. FDX1, POLD, etc.), known to be destabilized upon cluster loss. We expect loss of candidate adapter proteins to reverse destabilization under low iron or impaired ISC synthesis.

We also measured IRP2 levels as a readout of intracellular iron levels. Other than FBXL5, which binds oxygen and free iron to regulate IRP2, we did not consider

confounding secondary regulators. Interestingly, one would expect heme synthesis inhibition, which, increases cellular free iron, to decrease IRP2 levels. Paradoxically, inhibition of heme synthesis partially stabilizes IRP2 (Anderson et al., 2012). This suggests that other uncharacterized inputs into this pathway exist. Using the aforementioned IRP2 screening strategy under conditions of limited free iron, heme, or ISCs would uncover cofactor or metabolite specific regulators of IRP2.

Finally, we assumed all iron regulation, whether through IRP1/2, NRF2/BACH1, or otherwise to be at the transcriptional or post-transcriptional level. Our findings in chapter 3 point to a reflexive post-translational mechanism in which mitochondria may autonomously sense and respond to altered cellular iron homeostasis through mitochondrial ISCs and GSH. This hinted at the possibility of other autonomous organellar means of iron regulation. Proteomic analyses on other organelles such as lysosomes and endoplasmic reticulum will potential uncover novel free iron or heme regulated organellular metabolite switches.

**Toward a systematic characterization of heavy metal toxicity**

In our search for essential organellar functions under limited iron, we found that Golgi are vital because of their capacity to store manganese. Manganese overload phenocopied iron chelation—albeit only to a certain extent. Given similar substrate affinities, iron and manganese have reciprocal toxicities. Nonetheless, manganese toxicity and the cellular ramifications thereof are distinct from iron chelation. While several hypotheses including, altered autophagy (Zhang et al., 2019b), ROS production

(Martinez-Finley et al., 2013), calcium signaling (Zhu et al., 2019a), lipid composition (Corsetto et al., 2016), or carbohydrate metabolism (Baly et al., 1984), have been raised, there is no unified theory of manganese toxicity. Furthermore, other than direct $Mn^{2+}$ chelation or iron supplementation there are no effective downstream mitigating factors (e.g. antioxidants, hypoxia, etc.). Consequently, manganese toxicity, especially in the context of industrial inhalation during welding and mining, cause irreversible psychiatric disturbances and irreversible parkinsonism (Harischandra et al., 2019). It is also associated with Alzheimer's disease onset. Taken together, a comprehensive understanding of manganese homeostasis and toxicity would be clinically useful. It might clarify why a subset of neurons are particularly susceptible to its toxicity and how it contributes to the pathogenesis of neurodegenerative diseases.

Our brief characterization of iron's interaction with copper and zinc (Figure 3.4C,D) further emphasized the gaps in our knowledge about other heavy metals. Unbiased genetic screens and other systems approaches will highlight how these and other metals effect cytotoxicity and open up new therapeutic approaches to counter acute or chronic exposures. Given the importance of compartmentalization for iron and manganese homeostasis, these studies will reveal how metals are routed and stored inside the cell and with what other metals, proteins, or metabolites they interact. This work may also uncover novel transition metal signaling. Although the canonical way to sense and detoxify transition metals is through Metal regulatory transcription factor 1 (MTF1) and Metallothionein (MT), respectively, parallel systems or novel inputs into this system may also exist (Ziller and Fraissinet-Tachet, 2018). Finally, because MT

expression is upregulated in several tumor types and is associated with carcinogenesis, this work may clarify the relatively little explored role of heavy metal homeostasis for cancer progression (Si and Lang, 2018).

## Chapter 6: Materials and Methods

### Antibodies and Reagents

The following antibodies were purchased from the following vendors. Proteintech: SLC11A2 (20507-1-AP), PDHB (14744-1-AP), TF (17435-1-AP), FECH (14466-1-AP), LIAS (11577-1-AP), FDX1 (12592-1-AP), NDUFS1 (12444-1-AP), NDUFS3 (15066-1-AP), NDUFS7 (15728-1-AP), SLC25A39(14963-1-AP), SFXN1 (12296-1-AP) ATP2C1(13310-1-AP), HMOX1 (10701-1-AP). Abcam: UQCRFS1 (ab14746), SDHB (ab14714), SREBP-2 (ab30682). Novus Biologicals: ATP6V0C (NBP1-59654). Cell Signaling: CS(14309S), MPC1 (14462S), LAMP1(9091), LC3B (3868), VINCULIN (4650), IRP2 (37135), TFRC (13208), S6K (2708), pS6K (9234), ACO1/IRP1 (20272S), ACO2 (6571S). Genetex: ACTIN (GTX109639), GAPDH (GTX627408). Santa Cruz: NFS1 (sc-365308), SREBP-1 (sc-13551). BD Biosciences: HIF1a (610958). The following secondary antibodies were used: HRP-conjugated horse anti-mouse IgG (Cell Signaling 7076), HRP-conjugated and goat anti-rabbit IgG (Cell Signaling 7074). The following IR-Dye conjugated secondary antibodies were used: IR-Dye680LT-conjugated Donkey anti-mouse IgG (LICOR, 926-68022), IR-Dye800CW-conjugated Donkey anti-rabbit IgG (LICOR, 926-32212)

The following reagents were purchased from the following vendors: Pierce BCA Protein Assay Kit, (Thermo Fisher), Seahorse XF Cell Mito Stress Test Kit (Agilent), Seahorse XF RPMI medium, pH 7.4 (Agilent), D-Glucose (VWR), FBS (Sigma), Dialyzed FBS (GIBCO), Fetal Bovine Lipoprotein Deficient Serum (Kalen Biomedical), Tet Approved FBS (Takara), Bafilomycin A1 (Cayman), NB-598 (Adooq Bioscience), Erastin (Tocris), RSL3 (Selleckchem), L-Buthionine-sulfoximine (Sigma) Ferrostatin-1 (Tocris), Shield-1 (CheminPharma), Doxycycline (Sigma), Sodium Pyruvate (Sigma), Sodium Citrate Tribasic Dihydrate (Sigma), NH4Cl (Sigma), NH4OH (Sigma), Cholesterol (Sigma), Ammonium Iron (III) Citrate (FAC) (Sigma), Ammonium iron(II) sulfate hexahydrate (FAS) (Fisher Scientific), Manganese Chloride (Sigma), Zinc Chloride (Sigma), Copper Chloride (Sigma), Ethanol 100% (Fisher Scientific), Deferoxamine Mesylate(Sigma), DMSO(AlfaAesar), HPLC Grade Water (Fisher Scientific), HPLC Grade Methanol (Fisher Scientific), Pierce Anti-HA Magnetic Beads (ThermoFisher), Biotinylated holo-transferrin (ThermoFisher), Pierce High Sensitivity Streptavidin-HRP (ThermoFisher).

### Cell Lines

The KPC pancreas mouse cell line was kindly provided by Dr. Thales Papagiannakopoulos (New York University School of Medicine). Remaining cell lines (Jurkat, HEK293T, KMS26, and HeLa) were purchased from the ATCC. Cell lines were verified to be free of mycoplasma contamination and the identities of all were authenticated by STR profiling.

### Cell Culture Conditions

Unless otherwise indicated, cells were cultured in RPMI-1640 media (Gibco) containing 2 mM glutamine, 10% fetal bovine serum (Sigma), 1% penicillin and streptomycin (Invitrogen). For iron supplementation rescue experiments, cells were grown in indicated concentrations of ferric ammonium citrate with 1$\mu$M Ferrostatin-1. For lipoprotein depleted media, 10% fetal bovine serum was replaced with 10% lipoprotein depleted serum (Kalen Biomedical). For doxycycline inducible experiments, 10% fetal bovine serum was replaced with 10% Tet approved FBS (Takara) Unless otherwise indicated, all cells were maintained and grown at 37°C, 21% oxygen and 5% $CO_2$. For experiments at 0.5% or 3% oxygen, the hypoxia chamber (INVIVO) was set to 0.5% or 3% oxygen and culture media was preincubated under these conditions for 24 hours.

**Primers**

| Primer Name | Sequence | Purpose |
|---|---|---|
| Human SQLE-F | GATGATGCAGCTATTTTCGAGGC | qPCR |
| Human SQLE-R | CCTGAGCAAGGATATTCACGACA | qPCR |
| Human HMGCR-F | TGATTGACCTTTCCAGAGCAAG | qPCR |
| Human HMGCR-R | CTAAAATTGCCATTCCACGAGC | qPCR |
| Human HMGCS1-F | CTCTTGGGATGGACGGTATGC | qPCR |
| Human HMGCS1-R | GCTCCAACTCCACCTGTAGG | qPCR |
| Human SLC25A39 #1-F | TCGTGAAGATCGTGAGGCAC | qPCR |
| Human SLC25A39 #1-R | GGCTCGACCACACAGGAAG | qPCR |
| Human SLC25A39 #2-F | CCCTGGAGCTTATGCGGAC | qPCR |
| Human SLC25A39 #2-R | GCCTGAACCCATTGAGCCA | qPCR |
| Human beta-actin-F | TTTTGGCTATACCCTACTGGCA | qPCR |
| Human beta-actin-R | CTGCACAGTCGTCAGCATATC | qPCR |
| sgSQLE_F | caccGGAGAATTCCTGCAGCCGGG | CRISPR sgRNA |
| sgSQLE_R | aaacCCCGGCTGCAGGAATTCTCC-3’ | CRISPR sgRNA |
| sgSLC11A2_F | caccGTGCGACAGCCTGAACAGGA-3’ | CRISPR sgRNA |
| sgSLC11A2_R | aaacTCCTGTTCAGGCTGTCGCAC-3’ | CRISPR sgRNA |
| sgPDHA1_F | caccgTATGCTTCTCAAGGACAGGA-3’ | CRISPR sgRNA |
| sg PDHA1_R | aaacTCCTGTCCTTGAGAAGCATAC-3’ | CRISPR sgRNA |
| sgPDHB_F | caccgTCAGCTCCTACTCCAAACTG-3’ | CRISPR sgRNA |
| sgPDHB_R | aaacCAGTTTGGAGTAGGAGCTGAC-3’ | CRISPR sgRNA |
| sgSLC12A9_KO1_F | caccgTGGTTGGCCAACCGCAGCAG-3’ | CRISPR sgRNA |
| sgSLC12A9_KO1_R | aaacCTGCTGCGGTTGGCCAACCAc-3’ | CRISPR sgRNA |
| sgSLC12A9_KO1_F | caccGCTTCGGCTGGACGTCCGGA-3’ | CRISPR sgRNA |
| sgSLC12A9_KO1_R | aaacTCCGGACGTCCAGCCGAAGC-3’ | CRISPR sgRNA |
| sgSLC12A9_KO2_F | caccgTGGTTGGCCAACCGCAGCAG-3’ | CRISPR sgRNA |
| sgSLC12A9_KO2_R | aaacCTGCTGCGGTTGGCCAACCAc-3’ | CRISPR sgRNA |
| sgATP6V0A2_KO1_F | caccgAGAGGCTGGGAGCAAAACTG-3’ | CRISPR sgRNA |
| sgATP6V0A2_KO1_R | aaacCAGTTTTGCTCCCAGCCTCTC-3’ | CRISPR sgRNA |
| sgATP6V0A2_KO2_F | caccgCCAGGTACTGCACAAAACCG-3’ | CRISPR sgRNA |
| sgATP6V0A2_KO2_R | aaacCGGTTTTGTGCAGTACCTGGc-3’ | CRISPR sgRNA |
| sgATP6V0C_F | caccgCAAGAGCGGTACCGGCATTG-3’ | CRISPR sgRNA |
| sgATP6V0C_R | aaacCAATGCCGGTACCGCTCTTGC-3’ | CRISPR sgRNA |
| ATP2C1_KO1_F | caccgAAGCCTTGGAGTAGAACCAG | CRISPR sgRNA |
| ATP2C1_KO1_R | aaacCTGGTTCTACTCCAAGGCTTc | CRISPR sgRNA |
| ATP2C1_KO2_F | caccgCTAATGGGGAAGCCAACAGA | CRISPR sgRNA |
| ATP2C1_KO2_R | aaacTCTGTTGGCTTCCCCATTAGc | CRISPR sgRNA |

| | | |
|---|---|---|
| SLC25A39_KO1_F | caccgATAGGCAGTGAAGTAGATGG | CRISPR sgRNA |
| SLC25A39_KO1_R | aaacCCATCTACTTCACTGCCTATc | CRISPR sgRNA |

**Generation of knockout and overexpression constructs**
Forward and reverse oligos targeting *SQLE*, *SLC11A2, PDHB, SLC12A9, and ATPV0A2* were annealed and ligated into BSMBI-linearized plentiCRISPR v1 or v2 vector. Forward and reverse oligos targeting *SLC25A39* and *ATP2C1* were cloned into plentiCRISPRv1-GFP. Forward and reverse oligos targeting *ATP6V0C* were cloned into plentiCRISPRv2 shield vector. The sequences for the sgRNA oligos are listed in Primers Table. Gene fragments encoding SLC11A2.1, SLC11A2.2, and SLC25A39 were purchased from Twist Biosciences and cloned into pMXS-IRES-GFP by PCR and Gibson assembly. pMXS-IRES-RFP or IRES-GFP were used as empty vector controls. pLKO.1-dox-NFS1 sh#1 and pLKO.1-dox-NFS1 sh#2 were generously provided by Richard Possemato. pLJC5-Tmem192-2xFlag and pLJC5-Tmem192-3xHA constructs were generously provided by David Sabatini. pMXs-3XHA-EGFP-OMP25 and pMXs-3XMyC-EGFP-OMP25 were also generously provided by David Sabatini. The EGFP selection marker was removed and replaced with mCherry for use in all mitochondrial purification experiments.

**Cell Proliferation Assays**
2,000 Jurkat cells or 500 HeLa, 293T, or KPC cells were seeded in 0.2mL RPMI-1640 medium (Gibco) containing indicated treatments in triplicates in 96 well plates. On the day of seeding and after 5 days of growth, 50$\mu$L of Cell Titer Glo (Promega) reagent was added and luminescence was measured on a SpectraMax M3 plate reader (Molecular Devices). Data are presented as cell doublings or the $\log_2$ fold change in luminescence following 5 days of growth compared to initial reading on the day of seeding. Of note, ammonia experiments needed to be performed in 24 well plates to obtain consistent values.

**Generation of Knockout and overexpression cell lines**
For generation of knockdown or knockout cells, lentiviral packaging vectors VSV-G and Delta-VPR and plentiCRISPR expressing Cas9 and the appropriate sgRNA and pLKO.1-dox and the appropriate shRNA were simultaneously transfected into 293T cells using XtremeGene9 transfection reagent (Roche). For overexpression, pMXs-3XHA-mCherry-OMP25, pMXs-3XMyC-mCherry-OMP25, pMXS-IRES-GFP-SLC11A2 and pMXS-IRES-GFP-SLC25A39 backbone plasmids along retroviral packaging plasmids Gag-pol and VSV-G, were transfected into 293T cells. pMXS-IRES-RFP or GFP were used as empty vector controls. 60 hours post-transfection, the supernatant was collected and passed through a 0.45 syringe filter. For transduction, 0.1 x $10^6$ cells were plated in 6-well dishes containing 8mg/ml polybrene and virus, and spin infected by centrifugation at 2,200 rpm for 1.5 hours. Clonal knockouts were generated by FACS sorting single cells on a BD FACSAriaII, 72-96 hours post-infection into 96 well plates and grown for 2 weeks. To generate *SLC25A39* and *ATP2C1* knockout cells, cells were transfected with plentiCRISPR-GFP expressing Cas9 and the appropriate sgRNA and single $GFP^+$ clones were sorted and grown as above. Multiple clonal knockouts were validated via immunoblotting and cell proliferation assays. For overexpression cell lines, 72-96 hours post-infection, $RFP^+$ and $GFP^+$ cells were bulk-sorted on a BD FACSAriaII. For generation of conditional *ATP6V0C* knockout cells, cells were puromycin selected 48h post infection, pretreated with or without Shield-1 (0.5$\mu$M) for 3 days prior to a 5-day cell proliferation assay with or without Shield-1 (0.5$\mu$M) or FAC (0.1mg/ml). At the end point of the cell proliferation assay protein extracts were collected for immunoblotting. For generation of conditional *NFS1*

knockdown cells, cells were puromycin selected 72h post infection. Cells were then grown in the presence or absence of doxycycline (100 ng/ml) for 4d prior to mitochondrial harvest.

**Rapid lysosomal purification for LC-MS metabolite profiling**

Lysosomes were purified from 293T cell expressing pMXs-3XHA-EGFP-OMP25 and pMXs-3XMyC-EGFP-OMP2 according to the previously described protocol (Abu-Remaileh et al., 2017). Briefly, cells were grown for 24 hours under indicated treatments. ~30x $10^6$ cells were washed 2x in cold PBS, scraped into 1ml of cold KPBS, and pelleted via centrifugation at 1000x g for 1 minute, 30 seconds at 4ºC. Cells were resuspended in 1mL of KPBS, 10$\mu$l of cells were transferred into 50$\mu$l of 1% triton lysis buffer for a whole cell protein sample and 10$\mu$l of cells were transferred into 50$\mu$l of 80% methanol, containing heavy labeled amino acid standards, for direct extraction of whole cell metabolites. With one set of 20 strokes and another set of 10 strokes, the remaining sample was homogenized using a 2ml homogenizer. After centrifugation, the homogenate was incubated with 200$\mu$l of KPBS pre-washed anti-HA magnetic beads on a rotator shaker for 5 minutes at 4ºC. Beads were washed 3x in cold KPBS. 10% of bead volume was lysed with 1% triton buffer for protein extracts and remaining 90% was extracted in 80% methanol containing heavy labeled amino acid standards on a rotator shaker for 10 minutes at 4ºC. Samples were spun down at 20,000g to remove potential cellular debris or bead contamination prior to LC-MS polar metabolite profiling.

**Rapid mitochondrial purification for LC-MS metabolite profiling, proteomics, and immunoblotting**

Mitochondria were purified from 293T or HeLa cells expressing 3xHA-mCherry-OMP25 (mitochondria isolation) or 3xMyc-mCherry-OMP25 (background control) according to previously described protocol (Chen et al., 2016). Briefly, cells were grown for 24 hours under indicated treatments and processed accordingly to the lysosomal purification protocol. For metabolite profiling, 10% of bead volume was lysed with 1% triton buffer for protein extracts and the remaining 90% was extracted in 80% methanol containing heavy labeled amino acid standards on a rotator shaker for 10 minutes at 4ºC. For proteomics analyses and immunoblotting assays, 100% of the bead volume was lysed with 1% triton buffer.

**Mitochondrial Proteomics**

Following mitoIP purification, eluates, were dissolved in 8M urea, 50mM triethylammonium bicarbonate (TEAB), 10 mM dithiothreitol (DTT) and disulfides were reduced for 1 hour at room temperature. Alkylation was performed by adding iodoacetamide (IAA) and incubated for 1 hour at room temperature in the dark. Proteins were precipitated by Wessel/Flügge extraction (Wessel and Flugge, 1984) and pellets were dissolved in 100mM TEAB with endopeptidase LysC (2% w/w, enzyme/substrate) and incubated at 37°C for 2 hours. Sequencing grade modified trypsin (2 % w/w, enzyme/substrate) was added and digestion proceeded overnight at 30°C. Peptide solutions were labeled with 270 $\mu$g aliquots of TMTpro (16-plex) (Thermo). Protein pellets were dissolved in 8M urea, 50mM triethylammonium bicarbonate (TEAB), 10 mM dithiothreitol (DTT) and disulfides were reduced for 1 hour at room temperature. Alkylation was performed by adding iodoacetamide (IAA) and incubated for 1 hour at room temperature in the dark. Proteins were precipitated by Wessel/Flügge extraction[1] and pellets were dissolved in 100mM TEAB with endopeptidase LysC (2% w/w, enzyme/substrate) and incubated at 37°C for 2 hours. Sequencing grade modified trypsin (2 % w/w, enzyme/substrate) was added and digestion proceeded overnight at 30°C. Peptide solutions were labeled with 270 $\mu$g aliquots of TMTpro (Thermo Scientific) for 1 hour at room temperature and subsequently quenched with hydroxylamine for 15 minutes. An aliquot from each sample was combined for a ratio check,

according to which the samples were mixed. The pooled sample was purified using a high capacity reverse phase cartridge (Oasis HLB, Waters) and the eluate was fractionated using high pH reverse phase spin columns (Pierce) according to manufacturer specifications, yielding 8 fractions. Fractionated peptides were analyzed using an Easy-nLC 1200 HPLC equipped with a 250mm*75$\mu$m Easyspray column connected to a Fusion Lumos mass spectrometer (all Thermo Scientific) operating in synchronous precursor selection (SPS)-MS3 mode (McAlister et al., 2014) (10 SPS events). Solvent A was 0.1% formic acid in water and solvent B was 80% acetonitrile, 0.1% formic acid in water. Peptides were separated across a 90-minute linear gradient going from 7 to 33% B solvent at 300nL/minute. Precursors were fragmented by CID (35% CE) and MS2 ions were measured in the ion trap. MS2 ions were fragmented by HCD (65% CE) and MS3 reporter ions were measured in the orbitrap at 50K resolution. Raw files were searched through Proteome Discoverer v.2.3 (Thermo Scientific) and spectra were queried against the human proteome (database downloaded on 02/12/2019, containing 73662 sequences) using Sequest HT with a 1 % false discovery rate (FDR) applied. Oxidation of M was applied as a variable modification and carbamylation of C was applied as a static modification. A maximum isolation interference of 50% was allowed and 80% matching SPS ions were required. Protein abundance values were used for further statistical analysis. Subsequent statistical analysis was performed within the Perseus framework (Tyanova et al., 2016). All values were log2 transformed and normalized to the median intensity within each sample. An FDR-corrected t-test (q=0.05) was used to test for significance between sample groups.

**CRISPR/Cas9 Genetic Screens**

Metabolism-focused Cas9/sgRNA libraries were designed and genetic screens were performed and analyzed as previously described (Birsoy et al., 2015; Wang et al., 2014; Zhu et al., 2019b). Briefly, 40x $10^6$ Jurkat cells were infected with a lentiviral Cas9/sgRNA library at a 0.8 MOI. 48 hours following infection, cells were selected with puromycin for 72 hours and recovered for 24 hours. 40x $10^6$ cells, were pelleted and frozen as an initial sample and remaining cells were seeded into 500ml spinning flasks at a confluence of 80x $10^3$ cells/ml. Cells were split every 3 days and grown under indicated conditions for ~14 doublings. After 14 doublings, 40x $10^6$ cells were harvested for gDNA extraction using QIAamp Blood Midi Kit (Spin Protocol). sgRNAs were PCR amplified from 40$\mu$g of gDNA using Ex Taq DNA Polymerase, gel purified, and sequenced on NextSeq500 (Illumina) to quantify sgRNA abundance. After the sequencing reads were mapped, sgRNA counts were determined and guide scores, representing the log2 fold change of the normalized final read count of the guide from the initial read count of the guide, were calculated. Gene scores were defined as the median guide score.

**mTOR activation assay**

mTOR activation following amino acid starvation was assayed according to previously devised protocol (Zoncu et al., 2011). Briefly, 1x $10^6$ 293T cells were washed 2x in PBS and incubated in serum free, amino acid depleted RPMI media for 50 minutes under indicated treatments. Following amino acid starvation, a 10x amino stock containing amino acids at concentrations found in RPMI or PBS was added to wells for 10 minutes. Following amino acid re-feeding, cells were lysed according to immunoblot protocol and mTOR activation was assayed via immunoblotting of phosphorylated S6K.

**Real-time quantitative PCR**

RNAeasy Mini Kit (Qiagen) was used to isolate RNA from cells. 1$\mu$g of isolated RNA, quantified on a NanoDrop Microvolume Spectrophotometer (ThermoFisher) was used for cDNA synthesis

with Superscript II RT Kit (Invitrogen). qPCR was performed on a Thermo QuantStudio 6 Flex Real-Time PCR machine. The primer sequences are listed in Primers Table. Target genes SQLE, HMGCR, HMGCS1, and SLC25A39 were normalized to beta actin.

**Metabolite Profiling**

For bulk polar metabolite profiling and isotopic labeling, 1x $10^6$ Jurkat cells were seeded in triplicate in 6 well plates and grown for 24 hours under indicated treatments. For glucose and glutamine tracing experiments, cells were grown under indicated treatments for 12 hours in standard RPMI/10% FBS. After 12 hours, media was replaced with RPMI/10% dialyzed FBS (Gibco) lacking glutamine or glucose and containing [U-$^{13}$C]-glutamine (2mM) or [U-$^{13}$C]-glucose (10mM) l(Cambridge Isotopes), respectively, and grown for an additional 12 hours. Cells were washed 2x in cold 0.9% NaCl, extracted in 1ml 80% methanol containing $^{15}$N and $^{13}$C fully-labeled amino acid internal standards (MSK-A2-1.2, Cambridge Isotope Laboratories, Inc). Extracts were vortexed for 10 minutes, centrifuged at 20,000g to remove insoluble cell debris, nitrogen-dried, and stored at -80ºC until liquid chromatography-mass spectrometry (LC-MS). LC-MS was performed as previously described (Garcia-Bermudez et al., 2018) and relative quantification of metabolite abundances was performed using XCalibur QualBrowser 2.2 and Skyline Targeted Mass Spec Environment (MacCoss Lab) using a 5 ppm mass tolerance and a pooled-library of metabolite standards to confirm metabolite identity. Metabolite levels were normalized by cell counting and BCA protein quantification for each condition. For LysoIPs and MitoIPs, the LC-MS metabolite profiling protocol was the same as above except the metabolite extracts were not dried and 5$\mu$l of the 80% methanol extracts were directly injected for LC-MS.

For measurement of lanosterol and cholesterol, non-polar metabolites were extracted by phase separation through successive additions of 600$\mu$l of LC-MS grade 100% methanol, 300$\mu$l LC-MS grade water, and 400$\mu$l LC-MS grade chloroform. The lower, organic phase was carefully collected, nitrogen dried, and stored at -80ºC until LC-MS. LC-MS was run and analyzed, referencing cholesterol and lanosterol standards, as previously described (Garcia-Bermudez et al., 2019).

**Immunoblotting**

1x $10^6$ cells were washed in cold PBS and lysed in a buffer containing 10 mM Tris-Cl pH 7.5, 150 NaCl, 1 mM EDTA, 1% Triton X-100, 2% SDS, 0.1% CHAPS, and protease inhibitors (Roche). Lysates were sonicated, centrifuged at 20,000g, and total protein quantified using BCA Protein Assay Kit (Thermo Fisher). Supernatants were run on 8%, 10-20% or 12% SDS-PAGE and analyzed via immunoblotting. Blots were developed using the Licor Odyssey CLx infrared imaging system or Chemiluminescent detection and film exposure.

**Aconitase Activity Assay**

Aconitase activity assays were performed using the Aconitase Assay Kit (ab83459) purchased from Abcam. 293T cells were grown in the presence and absence of BafA1(10nM) and/or ferric ammonium citrate (0.1mg/ml) for 24 hours. 1x $10^6$ cells per well were processed according to manufacturer's protocol and aconitase activity was read out as the increase in absorbance at 240nm read in 45 second intervals over 30 minutes at room temperature on a SpectraMax M3 plate reader (Molecular Devices). Absorption at values 240nm were normalized to protein concentration as determined by BCA (Pierce) and converted to moles of cis-aconitate formed (extinction coefficient: 2.2 OD $mM^{-1}$/well).

**Transferrin Uptake Assay**
293T cells were grown in the presence or absence of BafA1 alone (10nM) or BafA1 (10nM) and ferric ammonium citrate (0.1mg/ml) for 24 hours. Cells were serum starved for 45 minutes and subsequently incubated with biotinylated-holo transferrin (20$\mu$g/ml) for 45 minutes. Cells were immediately washed in cold PBS, lysed, and resolved on 8% or 10-20% SDS-PAGE gels, and transferred to a PDVF membrane, according to immunoblotting protocols. Levels of holo versus apo transferrin was assessed via immunoblotting of transferrin or incubation of membrane in HRP-conjugated streptavidin (1:10,000).

**RNA Sequencing**
As above, 1x $10^6$ 293T cells were grown in 1$\mu$M ferristatin-1 with or without 0.1 mg/ml ferric ammonium citrate (FAC) for 24h. Following 24h growth, 10nM BafA1 was added to cells and cultured for an additional 24h. Cells were washed 2x with cold PBS and RNA was harvested using RNAeasy mini kit (Qiagen) according to manufacturer's protocol. 100 ng of total RNA was used to generate RNA-Seq libraries using Illumina TruSeq stranded mRNA LT kit (Cat# 20020594). Libraries prepared with unique barcodes were pooled at equal molar ratios. The pool was denatured and sequenced on Illumina NextSeq 500 sequencer using high output V2 reagents and NextSeq Control Software v1.4 to generate 75 bp single reads, following manufacturer's protocol (Cat# 15048776 Rev.E). Reads were aligned to GRCh38 using STAR RNA-seq aligner (Dobin et al., 2013). Aligned BAM files were sorted by coordinate and translated into transcript coordinates using quantMode SAM options. Transcript abundance was quantified using RSEM (Li and Dewey, 2011). Gene set enrichment analysis was performed on FPKM values from transcripts mapped to known coding genes from 3 biological replicates from each condition using 1000 permutations of the protein interaction data base (PID) gene set to generate pathway enrichment scores (Subramanian et al., 2005).

**Iron Staining**
$5x10^4$ 293T cells were seeded on MatTek No. 1.5, 35mM glass bottom culture dishes (MatTek P35G-1.5-14-C). As above, cells were pre-incubated for 24h in 1$\mu$M ferristatin-1 with or without 0.1 mg/ml ferric ammonium citrate. Cells were grown for an additional 24h in the presence or absence of DFO or BafA1. Plates were washed 3x in HBSS and stimulated at 37°C, 21% oxygen and 5% $CO_2$ for 20 minutes in HBSS. Next cells were stained in 1$\mu$M Ferro orange (dojingo) in HBSS for exactly 30 minutes at 37°C, 21% oxygen and 5% $CO_2$ and imaged immediately. Treatments were staggered to ensure precise staining duration. Focal images were acquired with a Zeiss inverted LSM 780 laser scanning confocal microscope (Zeiss) using a 63x/1.4 DIC Plan-Apochromat oil immersion objective. Five representative fields were captured for each condition under identical exposure times. Images were obtained with the Cy3 filter (ex 514nm, em 525-596). The images are 512 x 512 pixels with a pixel depth of 8-bit, with a pixel size of 0.264$\mu$m per pixel, a dwell time of 1.58$\mu$s, a pinhole size of 11.2 (1Airy unit), and a line averaging of 1.

**Oxygen Consumption Measurements**
Oxygen consumption rate of intact cells under the aforementioned treatments was performed using XF96e Extracellular Flux Analyzer (Seahorse Bioscience). 1x $10^4$ 293T cells were seeded on Seahorse cell culture plates. Cells were treated with Fer-1, FAC, BafA1 and DFO according to aforementioned protocol. Using XF MitoStress kit, oxygen consumption was measured as a proxy for basal respiration, ATP linked respiration, maximal respiration, and reserve capacity following respective injections with a blank, oligomycin (1.5$\mu$M), FCCP (1.0$\mu$M), and

Rotenone/Antimycin A (0.5$\mu$M). Oxygen consumption rate measurements were normalized to protein abundance via BCA (Pierce).

**Statistical Analyses**
Statistical analyses were performed on GraphPad Prism 8. Error bars are +/- sample standard deviation. Sample means, P-value, and sample size are indicated in text or figure legends.

**Data and Code Availability**
Raw data from RNA-sequencing experiments have been deposited in the Gene Expression Omnibus (GEO) and are available under accession code GSE141507.

## REFERENCES


Abu-Remaileh, M., Wyant, G.A., Kim, C., Laqtom, N.N., Abbasi, M., Chan, S.H., Freinkman, E., and Sabatini, D.M. (2017). Lysosomal metabolomics reveals V-ATPase- and mTOR-dependent regulation of amino acid efflux from lysosomes. Science *358*, 807-813.

Alvarez, S.W., Sviderskiy, V.O., Terzi, E.M., Papagiannakopoulos, T., Moreira, A.L., Adams, S., Sabatini, D.M., Birsoy, K., and Possemato, R. (2017). NFS1 undergoes positive selection in lung tumours and protects cells from ferroptosis. Nature *551*, 639-643.

Anderson, C.P., Shen, M., Eisenstein, R.S., and Leibold, E.A. (2012). Mammalian iron metabolism and its control by iron regulatory proteins. Biochim Biophys Acta *1823*, 1468-1483.

Andreini, C., Banci, L., Bertini, I., Elmi, S., and Rosato, A. (2007). Non-heme iron through the three domains of life. Proteins *67*, 317-324.

Andreini, C., Banci, L., Bertini, I., and Rosato, A. (2006). Zinc through the three domains of life. J Proteome Res *5*, 3173-3178.

Andreini, C., Bertini, I., and Rosato, A. (2009). Metalloproteomes: a bioinformatic approach. Acc Chem Res *42*, 1471-1479.

Andreini, C., Putignano, V., Rosato, A., and Banci, L. (2018). The human iron-proteome. Metallomics *10*, 1223-1231.

Appelmans, F., Wattiaux, R., and De Duve, C. (1955). Tissue fractionation studies. 5. The association of acid phosphatase with a special class of cytoplasmic granules in rat liver. Biochem J *59*, 438-445.

Ast, T., Meisel, J.D., Patra, S., Wang, H., Grange, R.M.H., Kim, S.H., Calvo, S.E., Orefice, L.L., Nagashima, F., Ichinose, F.*, et al.* (2019). Hypoxia Rescues Frataxin Loss by Restoring Iron Sulfur Cluster Biogenesis. Cell *177*, 1507-1521 e1516.

Bafaro, E., Liu, Y., Xu, Y., and Dempski, R.E. (2017). The emerging role of zinc transporters in cellular homeostasis and cancer. Signal Transduct Target Ther *2*.

Bainton, D.F. (1981). The discovery of lysosomes. J Cell Biol *91*, 66s-76s.

Bakkeren, D.L., de Jeu-Jaspars, C.M., van der Heul, C., and van Eijk, H.G. (1985). Analysis of iron-binding components in the low molecular weight fraction of rat reticulocyte cytosol. Int J Biochem *17*, 925-930.

Baly, D.L., Curry, D.L., Keen, C.L., and Hurley, L.S. (1984). Effect of manganese deficiency on insulin secretion and carbohydrate homeostasis in rats. J Nutr *114*, 1438-1446.

Bayeva, M., Khechaduri, A., Puig, S., Chang, H.C., Patial, S., Blackshear, P.J., and Ardehali, H. (2012). mTOR regulates cellular iron homeostasis through tristetraprolin. Cell Metab *16*, 645-657.

Beinert, H. (2000). Iron-sulfur proteins: ancient structures, still full of surprises. J Biol Inorg Chem *5*, 2-15.

Bergmann, M., Schutt, F., Holz, F.G., and Kopitz, J. (2004). Inhibition of the ATP-driven proton pump in RPE lysosomes by the major lipofuscin fluorophore A2-E may contribute to the pathogenesis of age-related macular degeneration. FASEB J *18*, 562-564.

Birsoy, K., Wang, T., Chen, W.W., Freinkman, E., Abu-Remaileh, M., and Sabatini, D.M. (2015). An Essential Role of the Mitochondrial Electron Transport Chain in Cell Proliferation Is to Enable Aspartate Synthesis. Cell *162*, 540-551.

Bjorklund, G., Dadar, M., Peana, M., Rahaman, M.S., and Aaseth, J. (2020). Interactions between iron and manganese in neurotoxicity. Arch Toxicol *94*, 725-734.

Blaby-Haas, C.E., and Merchant, S.S. (2014). Lysosome-related organelles as mediators of metal homeostasis. J Biol Chem *289*, 28129-28136.

Bode, H.P., Dumschat, M., Garotti, S., and Fuhrmann, G.F. (1995). Iron sequestration by the yeast vacuole. A study with vacuolar mutants of Saccharomyces cerevisiae. Eur J Biochem *228*, 337-342.

Bowman, E.J., Siebers, A., and Altendorf, K. (1988). Bafilomycins: a class of inhibitors of membrane ATPases from microorganisms, animal cells, and plant cells. Proc Natl Acad Sci U S A *85*, 7972-7976.

Boya, P., and Kroemer, G. (2008). Lysosomal membrane permeabilization in cell death. Oncogene *27*, 6434-6451.

Camaschella, C. (2015). Iron-deficiency anemia. N Engl J Med *372*, 1832-1843.

Cao, J.Y., Poddar, A., Magtanong, L., Lumb, J.H., Mileur, T.R., Reid, M.A., Dovey, C.M., Wang, J., Locasale, J.W., Stone, E.*, et al.* (2019). A Genome-wide Haploid Genetic Screen Identifies Regulators of Glutathione Abundance and Ferroptosis Sensitivity. Cell Rep *26*, 1544-1556 e1548.

Carmona, A., Deves, G., Roudeau, S., Cloetens, P., Bohic, S., and Ortega, R. (2010). Manganese accumulates within golgi apparatus in dopaminergic cells as revealed by synchrotron X-ray fluorescence nanoimaging. ACS Chem Neurosci *1*, 194-203.

Chapel, A., Kieffer-Jaquinod, S., Sagne, C., Verdon, Q., Ivaldi, C., Mellal, M., Thirion, J., Jadot, M., Bruley, C., Garin, J.*, et al.* (2013). An extended proteome map of the lysosomal membrane reveals novel potential transporters. Mol Cell Proteomics *12*, 1572-1588.

Chen, K.L., Ven, T.N., Crane, M.M., Brunner, M.L.C., Pun, A.K., Helget, K.L., Brower, K., Chen, D.E., Doan, H., Dillard-Telm, J.D.*, et al.* (2020). Loss of vacuolar acidity results in iron-sulfur cluster defects and divergent homeostatic responses during aging in Saccharomyces cerevisiae. Geroscience.

Chen, O.S., Hemenway, S., and Kaplan, J. (2002). Inhibition of Fe-S cluster biosynthesis decreases mitochondrial iron export: evidence that Yfh1p affects Fe-S cluster synthesis. Proc Natl Acad Sci U S A *99*, 12321-12326.

Chen, W., Dailey, H.A., and Paw, B.H. (2010). Ferrochelatase forms an oligomeric complex with mitoferrin-1 and Abcb10 for erythroid heme biosynthesis. Blood *116*, 628-630.

Chen, W.W., Freinkman, E., Wang, T., Birsoy, K., and Sabatini, D.M. (2016). Absolute Quantification of Matrix Metabolites Reveals the Dynamics of Mitochondrial Metabolism. Cell *166*, 1324-1337 e1311.

Chi, Y., Remsik, J., Kiseliovas, V., Derderian, C., Sener, U., Alghader, M., Saadeh, F., Nikishina, K., Bale, T., Iacobuzio-Donahue, C.*, et al.* (2020). Cancer cells deploy lipocalin-2 to collect limiting iron in leptomeningeal metastasis. Science *369*, 276-282.

Codazzi, F., Pelizzoni, I., Zacchetti, D., and Grohovaz, F. (2015). Iron entry in neurons and astrocytes: a link with synaptic activity. Front Mol Neurosci *8*, 18.

Correnti, C., Richardson, V., Sia, A.K., Bandaranayake, A.D., Ruiz, M., Suryo Rahmanto, Y., Kovacevic, Z., Clifton, M.C., Holmes, M.A., Kaiser, B.K.*, et al.* (2012). Siderocalin/Lcn2/NGAL/24p3 does not drive apoptosis through gentisic acid mediated iron withdrawal in hematopoietic cell lines. PLoS One *7*, e43696.

Corsetto, P.A., Ferrara, G., Buratta, S., Urbanelli, L., Montorfano, G., Gambelunghe, A., Chiaradia, E., Magini, A., Roderi, P., Colombo, I.*, et al.* (2016). Changes in Lipid Composition During Manganese-Induced Apoptosis in PC12 Cells. Neurochem Res *41*, 258-269.

Das, S., Carmona, A., Khatua, K., Porcaro, F., Somogyi, A., Ortega, R., and Datta, A. (2019). Manganese Mapping Using a Fluorescent Mn(2+) Sensor and Nanosynchrotron X-ray Fluorescence Reveals the Role of the Golgi Apparatus as a Manganese Storage Site. Inorg Chem *58*, 13724-13732.

Dautry-Varsat, A., Ciechanover, A., and Lodish, H.F. (1983). pH and the recycling of transferrin during receptor-mediated endocytosis. Proc Natl Acad Sci U S A *80*, 2258-2262.

Davis-Kaplan, S.R., Ward, D.M., Shiflett, S.L., and Kaplan, J. (2004). Genome-wide analysis of iron-dependent growth reveals a novel yeast gene required for vacuolar acidification. J Biol Chem *279*, 4322-4329.

De Duve, C., and Wattiaux, R. (1966). Functions of lysosomes. Annu Rev Physiol *28*, 435-492.

de Silva, D., Guo, J.H., and Aust, S.D. (1993). Relationship between iron and phosphate in mammalian ferritins. Arch Biochem Biophys *303*, 451-455.

Dempski, R.E. (2012). The cation selectivity of the ZIP transporters. Curr Top Membr *69*, 221-245.

Devireddy, L.R., Hart, D.O., Goetz, D.H., and Green, M.R. (2010). A mammalian siderophore synthesized by an enzyme with a bacterial homolog involved in enterobactin production. Cell *141*, 1006-1017.

Diab, H.I., and Kane, P.M. (2013). Loss of vacuolar H+-ATPase (V-ATPase) activity in yeast generates an iron deprivation signal that is moderated by induction of the peroxiredoxin TSA2. J Biol Chem *288*, 11366-11377.

Dixon, S.J., Lemberg, K.M., Lamprecht, M.R., Skouta, R., Zaitsev, E.M., Gleason, C.E., Patel, D.N., Bauer, A.J., Cantley, A.M., Yang, W.S.*, et al.* (2012). Ferroptosis: an iron-dependent form of nonapoptotic cell death. Cell *149*, 1060-1072.

Dobin, A., Davis, C.A., Schlesinger, F., Drenkow, J., Zaleski, C., Jha, S., Batut, P., Chaisson, M., and Gingeras, T.R. (2013). STAR: ultrafast universal RNA-seq aligner. Bioinformatics *29*, 15-21.

Dupont, C.L., Yang, S., Palenik, B., and Bourne, P.E. (2006). Modern proteomes contain putative imprints of ancient shifts in trace metal geochemistry. Proc Natl Acad Sci U S A *103*, 17822-17827.

Ferrer, M., Golyshina, O.V., Beloqui, A., Bottger, L.H., Andreu, J.M., Polaina, J., De Lacey, A.L., Trautwein, A.X., Timmis, K.N., and Golyshin, P.N. (2008). A purple acidophilic di-ferric DNA ligase from Ferroplasma. Proc Natl Acad Sci U S A *105*, 8878-8883.

Fleming, R.E., and Ponka, P. (2012). Iron overload in human disease. N Engl J Med *366*, 348-359.

Foury, F., and Roganti, T. (2002). Deletion of the mitochondrial carrier genes MRS3 and MRS4 suppresses mitochondrial iron accumulation in a yeast frataxin-deficient strain. J Biol Chem *277*, 24475-24483.

Furihata, T., Takada, S., Maekawa, S., Mizushima, W., Watanabe, M., Takahashi, H., Fukushima, A., Tsuda, M., Matsumoto, J., Kakutani, N.*, et al.* (2018). mitoNEET Regulates Mitochondrial Iron Homeostasis Interacting with Transferrin Receptor. bioRxiv, 330084.

Ganini, D., Santos, J.H., Bonini, M.G., and Mason, R.P. (2018). Switch of Mitochondrial Superoxide Dismutase into a Prooxidant Peroxidase in Manganese-Deficient Cells and Mice. Cell Chem Biol *25*, 413-425 e416.

Gao, G., and Chang, Y.Z. (2014). Mitochondrial ferritin in the regulation of brain iron homeostasis and neurodegenerative diseases. Front Pharmacol *5*, 19.

Garcia-Bermudez, J., Baudrier, L., Bayraktar, E.C., Shen, Y., La, K., Guarecuco, R., Yucel, B., Fiore, D., Tavora, B., Freinkman, E.*, et al.* (2019). Squalene accumulation in cholesterol auxotrophic lymphomas prevents oxidative cell death. Nature *567*, 118-122.

Garcia-Bermudez, J., Baudrier, L., La, K., Zhu, X.G., Fidelin, J., Sviderskiy, V.O., Papagiannakopoulos, T., Molina, H., Snuderl, M., Lewis, C.A.*, et al.* (2018). Aspartate is a limiting metabolite for cancer cell proliferation under hypoxia and in tumours. Nat Cell Biol *20*, 775-781.

Gauss, G.H., Kleven, M.D., Sendamarai, A.K., Fleming, M.D., and Lawrence, C.M. (2013). The crystal structure of six-transmembrane epithelial antigen of the prostate 4 (Steap4), a ferri/cuprireductase, suggests a novel interdomain flavin-binding site. J Biol Chem *288*, 20668-20682.

Goodwin, J.M., Dowdle, W.E., DeJesus, R., Wang, Z., Bergman, P., Kobylarz, M., Lindeman, A., Xavier, R.J., McAllister, G., Nyfeler, B.*, et al.* (2017). Autophagy-Independent Lysosomal Targeting Regulated by ULK1/2-FIP200 and ATG9. Cell Rep *20*, 2341-2356.

Graham, R.M., Thompson, J.W., and Webster, K.A. (2014). Inhibition of the vacuolar ATPase induces Bnip3-dependent death of cancer cells and a reduction in tumor burden and metastasis. Oncotarget *5*, 1162-1173.

Greene, B.T., Thorburn, J., Willingham, M.C., Thorburn, A., Planalp, R.P., Brechbiel, M.W., Jennings-Gee, J., Wilkinson, J.t., Torti, F.M., and Torti, S.V. (2002). Activation of caspase pathways during iron chelator-mediated apoptosis. J Biol Chem *277*, 25568-25575.

Gudekar, N., Shanbhag, V., Wang, Y., Ralle, M., Weisman, G.A., and Petris, M.J. (2020). Metallothioneins regulate ATP7A trafficking and control cell viability during copper deficiency and excess. Sci Rep *10*, 7856.

Harischandra, D.S., Ghaisas, S., Zenitsky, G., Jin, H., Kanthasamy, A., Anantharam, V., and Kanthasamy, A.G. (2019). Manganese-Induced Neurotoxicity: New Insights Into the Triad of Protein Misfolding, Mitochondrial Impairment, and Neuroinflammation. Front Neurosci *13*, 654.

Hider, R.C., and Kong, X.L. (2011). Glutathione: a key component of the cytoplasmic labile iron pool. Biometals *24*, 1179-1187.

Hubert, N., and Hentze, M.W. (2002). Previously uncharacterized isoforms of divalent metal transporter (DMT)-1: implications for regulation and cellular function. Proc Natl Acad Sci U S A *99*, 12345-12350.

Hughes, C.E., Coody, T.K., Jeong, M.Y., Berg, J.A., Winge, D.R., and Hughes, A.L. (2020). Cysteine Toxicity Drives Age-Related Mitochondrial Decline by Altering Iron Homeostasis. Cell *180*, 296-310 e218.

Hurlimann, J., and Zuber, C. (1968). In vitro protein synthesis by human slivary glands. II. Synthesis of proteins specific to saliva and other excretions. Immunology *14*, 819-824.

Inoue, H., Noumi, T., Nagata, M., Murakami, H., and Kanazawa, H. (1999). Targeted disruption of the gene encoding the proteolipid subunit of mouse vacuolar H(+)-ATPase leads to early embryonic lethality. Biochim Biophys Acta *1413*, 130-138.

Jensen, K.P., and Ryde, U. (2004). How O2 binds to heme: reasons for rapid binding and spin inversion. J Biol Chem *279*, 14561-14569.

Ji, C., and Kosman, D.J. (2015). Molecular mechanisms of non-transferrin-bound and transferring-bound iron uptake in primary hippocampal neurons. J Neurochem *133*, 668-683.

Johnson, Z.L., and Chen, J. (2017). Structural Basis of Substrate Recognition by the Multidrug Resistance Protein MRP1. Cell *168*, 1075-1085 e1079.

Jouihan, H.A., Cobine, P.A., Cooksey, R.C., Hoagland, E.A., Boudina, S., Abel, E.D., Winge, D.R., and McClain, D.A. (2008). Iron-mediated inhibition of mitochondrial manganese uptake mediates mitochondrial dysfunction in a mouse model of hemochromatosis. Mol Med *14*, 98-108.

Kao, Y.R., Chen, J., Narayanagari, S.R., Todorova, T.I., Aivalioti, M.M., Ferreira, M., Ramos, P.M., Pallaud, C., Mantzaris, I., Shastri, A.*, et al.* (2018). Thrombopoietin receptor-independent stimulation of hematopoietic stem cells by eltrombopag. Sci Transl Med *10*.

Karnkowska, A., Vacek, V., Zubacova, Z., Treitli, S.C., Petrzelkova, R., Eme, L., Novak, L., Zarsky, V., Barlow, L.D., Herman, E.K.*, et al.* (2016). A Eukaryote without a Mitochondrial Organelle. Curr Biol *26*, 1274-1284.

Kinoshita, K., Waritani, T., Noto, M., Takizawa, K., Minemoto, Y., Nishikawa, A., and Ohkuma, S. (1996). Bafilomycin A1 induces apoptosis in PC12 cells independently of intracellular pH. FEBS Lett *398*, 61-66.

Kispal, G., Csere, P., Prohl, C., and Lill, R. (1999). The mitochondrial proteins Atm1p and Nfs1p are essential for biogenesis of cytosolic Fe/S proteins. EMBO J *18*, 3981-3989.

Klempner, M.S., and Styrt, B. (1983). Alkalinizing the intralysosomal pH inhibits degranulation of human neutrophils. J Clin Invest *72*, 1793-1800.

Knutson, M.D. (2019). Non-transferrin-bound iron transporters. Free Radic Biol Med *133*, 101-111.

Koh, J.Y., Kim, H.N., Hwang, J.J., Kim, Y.H., and Park, S.E. (2019). Lysosomal dysfunction in proteinopathic neurodegenerative disorders: possible therapeutic roles of cAMP and zinc. Mol Brain *12*, 18.

Kramer, J., Ozkaya, O., and Kummerli, R. (2020). Bacterial siderophores in community and host interactions. Nat Rev Microbiol *18*, 152-163.

Kumar, C., Igbaria, A., D'Autreaux, B., Planson, A.G., Junot, C., Godat, E., Bachhawat, A.K., Delaunay-Moisan, A., and Toledano, M.B. (2011). Glutathione revisited: a vital function in iron metabolism and ancillary role in thiol-redox control. EMBO J *30*, 2044-2056.

Kusminski, C.M., Holland, W.L., Sun, K., Park, J., Spurgin, S.B., Lin, Y., Askew, G.R., Simcox, J.A., McClain, D.A., Li, C.*, et al.* (2012). MitoNEET-driven alterations in adipocyte mitochondrial activity reveal a crucial adaptive process that preserves insulin sensitivity in obesity. Nat Med *18*, 1539-1549.

Lawrence, R.E., and Zoncu, R. (2019). The lysosome as a cellular centre for signalling, metabolism and quality control. Nat Cell Biol *21*, 133-142.

Lee, D.A., and Goodfellow, J.M. (1998). The pH-induced release of iron from transferrin investigated with a continuum electrostatic model. Biophys J *74*, 2747-2759.

Lee, H., Lee, H.J., Seo, J., Kim, H.E., Shin, Y.K., Kim, J.H., and Lee, C. (2016). Activation of Oxygen and Hydrogen Peroxide by Copper(II) Coupled with Hydroxylamine for Oxidation of Organic Contaminants. Environ Sci Technol *50*, 8231-8238.

Li, B., and Dewey, C.N. (2011). RSEM: accurate transcript quantification from RNA-Seq data with or without a reference genome. BMC Bioinformatics *12*, 323.

Li, L., Chen, O.S., McVey Ward, D., and Kaplan, J. (2001). CCC1 is a transporter that mediates vacuolar iron storage in yeast. J Biol Chem *276*, 29515-29519.

Lill, R., and Freibert, S.A. (2020). Mechanisms of Mitochondrial Iron-Sulfur Protein Biogenesis. Annu Rev Biochem *89*, 471-499.

Loeffler, D., Wehling, A., Schneiter, F., Zhang, Y., Muller-Botticher, N., Hoppe, P.S., Hilsenbeck, O., Kokkaliaris, K.D., Endele, M., and Schroeder, T. (2019). Asymmetric lysosome inheritance predicts activation of haematopoietic stem cells. Nature *573*, 426-429.

MacVicar, T., Ohba, Y., Nolte, H., Mayer, F.C., Tatsuta, T., Sprenger, H.G., Lindner, B., Zhao, Y., Li, J., Bruns, C*., et al.* (2019). Lipid signalling drives proteolytic rewiring of mitochondria by YME1L. Nature *575*, 361-365.

Maio, N., and Rouault, T.A. (2016). Mammalian Fe-S proteins: definition of a consensus motif recognized by the co-chaperone HSC20. Metallomics *8*, 1032-1046.

Manabe, T., Yoshimori, T., Henomatsu, N., and Tashiro, Y. (1993). Inhibitors of vacuolar-type H(+)-ATPase suppresses proliferation of cultured cells. J Cell Physiol *157*, 445-452.

Mancias, J.D., Wang, X., Gygi, S.P., Harper, J.W., and Kimmelman, A.C. (2014). Quantitative proteomics identifies NCOA4 as the cargo receptor mediating ferritinophagy. Nature *509*, 105-109.

Martinez-Finley, E.J., Gavin, C.E., Aschner, M., and Gunter, T.E. (2013). Manganese neurotoxicity and the role of reactive oxygen species. Free Radic Biol Med *62*, 65-75.

Maxfield, F.R. (2014). Role of endosomes and lysosomes in human disease. Cold Spring Harb Perspect Biol *6*, a016931.

McAlister, G.C., Nusinow, D.P., Jedrychowski, M.P., Wuhr, M., Huttlin, E.L., Erickson, B.K., Rad, R., Haas, W., and Gygi, S.P. (2014). MultiNotch MS3 enables accurate, sensitive, and multiplexed detection of differential expression across cancer cell line proteomes. Anal Chem *86*, 7150-7158.

McDonough, W.F. (2001). Earthquake thermodynamics and phase transformations in the earth's interior. In International geophysics series, R. Teisseyre, and E. Majewski, eds. (San Diego, Calif.: Academic Press), pp. 3-23.

Meyer, J. (2008). Iron-sulfur protein folds, iron-sulfur chemistry, and evolution. J Biol Inorg Chem *13*, 157-170.

Miles, A.L., Burr, S.P., Grice, G.L., and Nathan, J.A. (2017). The vacuolar-ATPase complex and assembly factors, TMEM199 and CCDC115, control HIF1alpha prolyl hydroxylation by regulating cellular iron levels. Elife *6*.

Mindell, J.A. (2012). Lysosomal acidification mechanisms. Annu Rev Physiol *74*, 69-86.

Muckenthaler, M.U., Rivella, S., Hentze, M.W., and Galy, B. (2017). A Red Carpet for Iron Metabolism. Cell *168*, 344-361.

Mullen, P.J., Yu, R., Longo, J., Archer, M.C., and Penn, L.Z. (2016). The interplay between cell signalling and the mevalonate pathway in cancer. Nat Rev Cancer *16*, 718-731.

Nakashima, S., Hiraku, Y., Tada-Oikawa, S., Hishita, T., Gabazza, E.C., Tamaki, S., Imoto, I., Adachi, Y., and Kawanishi, S. (2003). Vacuolar H+-ATPase inhibitor induces apoptosis via lysosomal dysfunction in the human gastric cancer cell line MKN-1. J Biochem *134*, 359-364.

Nandal, A., Ruiz, J.C., Subramanian, P., Ghimire-Rijal, S., Sinnamon, R.A., Stemmler, T.L., Bruick, R.K., and Philpott, C.C. (2011). Activation of the HIF prolyl hydroxylase by the iron chaperones PCBP1 and PCBP2. Cell Metab *14*, 647-657.

Nemeth, E., Tuttle, M.S., Powelson, J., Vaughn, M.B., Donovan, A., Ward, D.M., Ganz, T., and Kaplan, J. (2004). Hepcidin regulates cellular iron efflux by binding to ferroportin and inducing its internalization. Science *306*, 2090-2093.

Nilsson, R., Schultz, I.J., Pierce, E.L., Soltis, K.A., Naranuntarat, A., Ward, D.M., Baughman, J.M., Paradkar, P.N., Kingsley, P.D., Culotta, V.C.*, et al.* (2009). Discovery of genes essential for heme biosynthesis through large-scale gene expression analysis. Cell Metab *10*, 119-130.

Nishihara, T., Akifusa, S., Koseki, T., Kato, S., Muro, M., and Hanada, N. (1995). Specific inhibitors of vacuolar type H(+)-ATPases induce apoptotic cell death. Biochem Biophys Res Commun *212*, 255-262.

Novikoff, A.B., Beaufay, H., and De Duve, C. (1956). Electron microscopy of lysosomerich fractions from rat liver. J Biophys Biochem Cytol *2*, 179-184.

Ohta, T., Arakawa, H., Futagami, F., Fushida, S., Kitagawa, H., Kayahara, M., Nagakawa, T., Miwa, K., Kurashima, K., Numata, M.*, et al.* (1998). Bafilomycin A1 induces apoptosis in the human pancreatic cancer cell line Capan-1. J Pathol *185*, 324-330.

Ouyang, Y., Peng, Y., Li, J., Holmgren, A., and Lu, J. (2018). Modulation of thiol-dependent redox system by metal ions via thioredoxin and glutaredoxin systems. Metallomics *10*, 218-228.

Pain, J., Balamurali, M.M., Dancis, A., and Pain, D. (2010). Mitochondrial NADH kinase, Pos5p, is required for efficient iron-sulfur cluster biogenesis in Saccharomyces cerevisiae. J Biol Chem *285*, 39409-39424.

Paradkar, P.N., Zumbrennen, K.B., Paw, B.H., Ward, D.M., and Kaplan, J. (2009). Regulation of mitochondrial iron import through differential turnover of mitoferrin 1 and mitoferrin 2. Mol Cell Biol *29*, 1007-1016.

Patel, M., and Ramavataram, D.V. (2012). Non transferrin bound iron: nature, manifestations and analytical approaches for estimation. Indian J Clin Biochem *27*, 322-332.

Patton, S.M., Pinero, D.J., Surguladze, N., Beard, J., and Connor, J.R. (2005). Subcellular localization of iron regulatory proteins to Golgi and ER membranes. J Cell Sci *118*, 4365-4373.

Petrezselyova, S., Kinclova-Zimmermannova, O., and Sychrova, H. (2013). Vhc1, a novel transporter belonging to the family of electroneutral cation-Cl(-) cotransporters, participates in the regulation of cation content and morphology of Saccharomyces cerevisiae vacuoles. Biochim Biophys Acta *1828*, 623-631.

Pietrocola, F., Galluzzi, L., Bravo-San Pedro, J.M., Madeo, F., and Kroemer, G. (2015). Acetyl coenzyme A: a central metabolite and second messenger. Cell Metab *21*, 805-821.

Platt, F.M., d'Azzo, A., Davidson, B.L., Neufeld, E.F., and Tifft, C.J. (2018). Lysosomal storage diseases. Nat Rev Dis Primers *4*, 27.

Ponka, P., Sheftel, A.D., English, A.M., Scott Bohle, D., and Garcia-Santos, D. (2017). Do Mammalian Cells Really Need to Export and Import Heme? Trends Biochem Sci *42*, 395-406.

Posey, J.E., and Gherardini, F.C. (2000). Lack of a role for iron in the Lyme disease pathogen. Science *288*, 1651-1653.

Price, D., and Joshi, J.G. (1982). Ferritin: a zinc detoxicant and a zinc ion donor. Proc Natl Acad Sci U S A *79*, 3116-3119.

Pyrih, J., Pyrihova, E., Kolisko, M., Stojanovova, D., Basu, S., Harant, K., Haindrich, A.C., Dolezal, P., Lukes, J., Roger, A.*, et al.* (2016). Minimal cytosolic iron-sulfur cluster assembly machinery of Giardia intestinalis is partially associated with mitosomes. Mol Microbiol *102*, 701-714.

Raguzzi, F., Lesuisse, E., and Crichton, R.R. (1988). Iron storage in Saccharomyces cerevisiae. FEBS Lett *231*, 253-258.

Rainey, N.E., Moustapha, A., Saric, A., Nicolas, G., Sureau, F., and Petit, P.X. (2019). Iron chelation by curcumin suppresses both curcumin-induced autophagy and cell death together with iron overload neoplastic transformation. Cell Death Discov *5*, 150.

Rajagopalan, K.N., Egnatchik, R.A., Calvaruso, M.A., Wasti, A.T., Padanad, M.S., Boroughs, L.K., Ko, B., Hensley, C.T., Acar, M., Hu, Z.*, et al.* (2015). Metabolic plasticity maintains proliferation in pyruvate dehydrogenase deficient cells. Cancer Metab *3*, 7.

Rouault, T.A. (2016). Mitochondrial iron overload: causes and consequences. Curr Opin Genet Dev *38*, 31-37.

Sallin, O., Reymond, L., Gondrand, C., Raith, F., Koch, B., and Johnsson, K. (2018). Semisynthetic biosensors for mapping cellular concentrations of nicotinamide adenine dinucleotides. Elife *7*.

Scheiber-Mojdehkar, B., Lutzky, B., Schaufler, R., Sturm, B., and Goldenberg, H. (2004). Non-transferrin-bound iron in the serum of hemodialysis patients who receive ferric saccharate: no correlation to peroxide generation. J Am Soc Nephrol *15*, 1648-1655.

Senturk, S., Shirole, N.H., Nowak, D.G., Corbo, V., Pal, D., Vaughan, A., Tuveson, D.A., Trotman, L.C., Kinney, J.B., and Sordella, R. (2017). Rapid and tunable method to temporally control gene editing based on conditional Cas9 stabilization. Nat Commun *8*, 14370.

Settembre, C., Di Malta, C., Polito, V.A., Garcia Arencibia, M., Vetrini, F., Erdin, S., Erdin, S.U., Huynh, T., Medina, D., Colella, P.*, et al.* (2011). TFEB links autophagy to lysosomal biogenesis. Science *332*, 1429-1433.

Shah, N.R. (2017). Advances in iron chelation therapy: transitioning to a new oral formulation. Drugs Context *6*, 212502.

Sharma, S., Sivalingam, K., Neese, F., and Chan, G.K. (2014). Low-energy spectrum of iron-sulfur clusters directly from many-particle quantum mechanics. Nat Chem *6*, 927-933.

Shaw, G.C., Cope, J.J., Li, L., Corson, K., Hersey, C., Ackermann, G.E., Gwynn, B., Lambert, A.J., Wingert, R.A., Traver, D.*, et al.* (2006). Mitoferrin is essential for erythroid iron assimilation. Nature *440*, 96-100.

Sheftel, A.D., Mason, A.B., and Ponka, P. (2012). The long history of iron in the Universe and in health and disease. Biochim Biophys Acta *1820*, 161-187.

Sheftel, A.D., Zhang, A.S., Brown, C., Shirihai, O.S., and Ponka, P. (2007). Direct interorganellar transfer of iron from endosome to mitochondrion. Blood *110*, 125-132.

Shi, H., Bencze, K.Z., Stemmler, T.L., and Philpott, C.C. (2008). A cytosolic iron chaperone that delivers iron to ferritin. Science *320*, 1207-1210.

Shokolenko, I., Venediktova, N., Bochkareva, A., Wilson, G.L., and Alexeyev, M.F. (2009). Oxidative stress induces degradation of mitochondrial DNA. Nucleic Acids Res *37*, 2539-2548.

Si, M., and Lang, J. (2018). The roles of metallothioneins in carcinogenesis. J Hematol Oncol *11*, 107.

Siegert, I., Schodel, J., Nairz, M., Schatz, V., Dettmer, K., Dick, C., Kalucka, J., Franke, K., Ehrenschwender, M., Schley, G.*, et al.* (2015). Ferritin-Mediated Iron Sequestration Stabilizes Hypoxia-Inducible Factor-1alpha upon LPS Activation in the Presence of Ample Oxygen. Cell Rep *13*, 2048-2055.

Slabbaert, J.R., Kuenen, S., Swerts, J., Maes, I., Uytterhoeven, V., Kasprowicz, J., Fernandes, A.C., Blust, R., and Verstreken, P. (2016). Shawn, the Drosophila Homolog of SLC25A39/40, Is a Mitochondrial Carrier That Promotes Neuronal Survival. J Neurosci *36*, 1914-1929.

Spinelli, J.B., Yoon, H., Ringel, A.E., Jeanfavre, S., Clish, C.B., and Haigis, M.C. (2017). Metabolic recycling of ammonia via glutamate dehydrogenase supports breast cancer biomass. Science *358*, 941-946.

Subramanian, A., Tamayo, P., Mootha, V.K., Mukherjee, S., Ebert, B.L., Gillette, M.A., Paulovich, A., Pomeroy, S.L., Golub, T.R., Lander, E.S.*, et al.* (2005). Gene set enrichment analysis: a knowledge-based approach for interpreting genome-wide expression profiles. Proc Natl Acad Sci U S A *102*, 15545-15550.

Sun-Wada, G., Murata, Y., Yamamoto, A., Kanazawa, H., Wada, Y., and Futai, M. (2000). Acidic endomembrane organelles are required for mouse postimplantation development. Dev Biol *228*, 315-325.

Telfer, T.J., Richardson-Sanchez, T., Gotsbacher, M.P., Nolan, K.P., Tieu, W., and Codd, R. (2019). Analogues of desferrioxamine B (DFOB) with new properties and new functions generated using precursor-directed biosynthesis. Biometals *32*, 395-408.

Toth, I., and Bridges, K.R. (1995). Ascorbic acid enhances ferritin mRNA translation by an IRP/aconitase switch. J Biol Chem *270*, 19540-19544.

Tsherniak, A., Vazquez, F., Montgomery, P.G., Weir, B.A., Kryukov, G., Cowley, G.S., Gill, S., Harrington, W.F., Pantel, S., Krill-Burger, J.M.*, et al.* (2017). Defining a Cancer Dependency Map. Cell *170*, 564-576 e516.

Tsukamoto, S., Hara, T., Yamamoto, A., Ohta, Y., Wada, A., Ishida, Y., Kito, S., Nishikawa, T., Minami, N., Sato, K.*, et al.* (2013). Functional analysis of lysosomes during mouse preimplantation embryo development. J Reprod Dev *59*, 33-39.

Tyanova, S., Temu, T., Sinitcyn, P., Carlson, A., Hein, M.Y., Geiger, T., Mann, M., and Cox, J. (2016). The Perseus computational platform for comprehensive analysis of (prote)omics data. Nat Methods *13*, 731-740.

Vashisht, A.A., Zumbrennen, K.B., Huang, X., Powers, D.N., Durazo, A., Sun, D., Bhaskaran, N., Persson, A., Uhlen, M., Sangfelt, O.*, et al.* (2009). Control of iron homeostasis by an iron-regulated ubiquitin ligase. Science *326*, 718-721.

Veatch, J.R., McMurray, M.A., Nelson, Z.W., and Gottschling, D.E. (2009). Mitochondrial dysfunction leads to nuclear genome instability via an iron-sulfur cluster defect. Cell *137*, 1247-1258.

Venkataramani, V., Doeppner, T.R., Willkommen, D., Cahill, C.M., Xin, Y., Ye, G., Liu, Y., Southon, A., Aron, A., Au-Yeung, H.Y.*, et al.* (2018). Manganese causes neurotoxic iron accumulation via translational repression of amyloid precursor protein and H-Ferritin. J Neurochem *147*, 831-848.

Wachtershauser, G. (1990). Evolution of the first metabolic cycles. Proc Natl Acad Sci U S A *87*, 200-204.

Wang, H., Shi, H., Rajan, M., Canarie, E.R., Hong, S., Simoneschi, D., Pagano, M., Bush, M.F., Stoll, S., Leibold, E.A.*, et al.* (2020). FBXL5 Regulates IRP2 Stability in Iron Homeostasis via an Oxygen-Responsive [2Fe2S] Cluster. Mol Cell *78*, 31-41 e35.

Wang, T., Wei, J.J., Sabatini, D.M., and Lander, E.S. (2014). Genetic screens in human cells using the CRISPR-Cas9 system. Science *343*, 80-84.

Wessel, D., and Flugge, U.I. (1984). A method for the quantitative recovery of protein in dilute solution in the presence of detergents and lipids. Anal Biochem *138*, 141-143.

Wiley, S.E., Paddock, M.L., Abresch, E.C., Gross, L., van der Geer, P., Nechushtai, R., Murphy, A.N., Jennings, P.A., and Dixon, J.E. (2007). The outer mitochondrial membrane protein mitoNEET contains a novel redox-active 2Fe-2S cluster. J Biol Chem *282*, 23745-23749.

Wilson, R.B., and Roof, D.M. (1997). Respiratory deficiency due to loss of mitochondrial DNA in yeast lacking the frataxin homologue. Nat Genet *16*, 352-357.

Wyant, G.A., Abu-Remaileh, M., Wolfson, R.L., Chen, W.W., Freinkman, E., Danai, L.V., Vander Heiden, M.G., and Sabatini, D.M. (2017). mTORC1 Activator SLC38A9 Is Required to Efflux Essential Amino Acids from Lysosomes and Use Protein as a Nutrient. Cell *171*, 642-654 e612.

Xia, Z., Wei, J., Li, Y., Wang, J., Li, W., Wang, K., Hong, X., Zhao, L., Chen, C., Min, J.*, et al.* (2017). Zebrafish slc30a10 deficiency revealed a novel compensatory mechanism of Atp2c1 in maintaining manganese homeostasis. PLoS Genet *13*, e1006892.

Xiao, G., Wan, Z., Fan, Q., Tang, X., and Zhou, B. (2014). The metal transporter ZIP13 supplies iron into the secretory pathway in Drosophila melanogaster. Elife *3*, e03191.

Xiao, Y., Chen, X., Huang, S., Li, G., Mo, M., Zhang, L., Chen, C., Guo, W., Zhou, M., Wu, Z.*, et al.* (2018). Iron promotes alpha-synuclein aggregation and transmission by inhibiting TFEB-mediated autophagosome-lysosome fusion. J Neurochem *145*, 34-50.

Xu, J., Wan, Z., and Zhou, B. (2019). Drosophila ZIP13 is posttranslationally regulated by iron-mediated stabilization. Biochim Biophys Acta Mol Cell Res *1866*, 1487-1497.

Yambire, K.F., Rostosky, C., Watanabe, T., Pacheu-Grau, D., Torres-Odio, S., Sanchez-Guerrero, A., Senderovich, O., Meyron-Holtz, E.G., Milosevic, I., Frahm, J.*, et al.* (2019). Impaired lysosomal acidification triggers iron deficiency and inflammation in vivo. Elife *8*.

Yan, Y., Jiang, K., Liu, P., Zhang, X., Dong, X., Gao, J., Liu, Q., Barr, M.P., Zhang, Q., Hou, X.*, et al.* (2016). Bafilomycin A1 induces caspase-independent cell death in hepatocellular carcinoma cells via targeting of autophagy and MAPK pathways. Sci Rep *6*, 37052.

Yang, B., Keshelava, N., Anderson, C.P., and Reynolds, C.P. (2003). Antagonism of buthionine sulfoximine cytotoxicity for human neuroblastoma cell lines by hypoxia is reversed by the bioreductive agent tirapazamine. Cancer Res *63*, 1520-1526.

Yang, S., Wang, X., Contino, G., Liesa, M., Sahin, E., Ying, H., Bause, A., Li, Y., Stommel, J.M., Dell'antonio, G.*, et al.* (2011). Pancreatic cancers require autophagy for tumor growth. Genes Dev *25*, 717-729.

Yang, W.S., and Stockwell, B.R. (2016). Ferroptosis: Death by Lipid Peroxidation. Trends Cell Biol *26*, 165-176.

Yu, X.X., Lewin, D.A., Zhong, A., Brush, J., Schow, P.W., Sherwood, S.W., Pan, G., and Adams, S.H. (2001). Overexpression of the human 2-oxoglutarate carrier lowers mitochondrial membrane potential in HEK-293 cells: contrast with the unique cold-induced mitochondrial carrier CGI-69. Biochem J *353*, 369-375.

Yu, Y., and Richardson, D.R. (2011). Cellular iron depletion stimulates the JNK and p38 MAPK signaling transduction pathways, dissociation of ASK1-thioredoxin, and activation of ASK1. J Biol Chem *286*, 15413-15427.

Yuan, N., Song, L., Zhang, S., Lin, W., Cao, Y., Xu, F., Fang, Y., Wang, Z., Zhang, H., Li, X.*, et al.* (2015). Bafilomycin A1 targets both autophagy and apoptosis pathways in pediatric B-cell acute lymphoblastic leukemia. Haematologica *100*, 345-356.

Zhang, S., Macias-Garcia, A., Ulirsch, J.C., Velazquez, J., Butty, V.L., Levine, S.S., Sankaran, V.G., and Chen, J.J. (2019a). HRI coordinates translation necessary for protein homeostasis and mitochondrial function in erythropoiesis. Elife *8*.

Zhang, Z., Yan, J., Bowman, A.B., Bryan, M.R., Singh, R., and Aschner, M. (2019b). Dysregulation of TFEB contributes to manganese-induced autophagic failure and mitochondrial dysfunction in astrocytes. Autophagy, 1-18.

Zhu, G., Liu, Y., Zhi, Y., Jin, Y., Li, J., Shi, W., Liu, Y., Han, Y., Yu, S., Jiang, J.*, et al.* (2019a). PKA- and Ca(2+)-dependent p38 MAPK/CREB activation protects against manganese-mediated neuronal apoptosis. Toxicol Lett *309*, 10-19.

Zhu, W., Winter, M.G., Spiga, L., Hughes, E.R., Chanin, R., Mulgaonkar, A., Pennington, J., Maas, M., Behrendt, C.L., Kim, J.*, et al.* (2020). Xenosiderophore Utilization Promotes Bacteroides thetaiotaomicron Resilience during Colitis. Cell Host Microbe *27*, 376-388 e378.

Zhu, X.G., Nicholson Puthenveedu, S., Shen, Y., La, K., Ozlu, C., Wang, T., Klompstra, D., Gultekin, Y., Chi, J., Fidelin, J.*, et al.* (2019b). CHP1 Regulates Compartmentalized Glycerolipid Synthesis by Activating GPAT4. Mol Cell *74*, 45-58 e47.

Ziller, A., and Fraissinet-Tachet, L. (2018). Metallothionein diversity and distribution in the tree of life: a multifunctional protein. Metallomics *10*, 1549-1559.

Zoncu, R., Bar-Peled, L., Efeyan, A., Wang, S., Sancak, Y., and Sabatini, D.M. (2011). mTORC1 senses lysosomal amino acids through an inside-out mechanism that requires the vacuolar H(+)-ATPase. Science *334*, 678-683.

Zoroddu, M.A., Aaseth, J., Crisponi, G., Medici, S., Peana, M., and Nurchi, V.M. (2019). The essential metals for humans: a brief overview. J Inorg Biochem *195*, 120-129.